Noble metal nanoparticles for assay development

A thesis submitted to Dublin City University
for the degree of Doctor of Philosophy

by

Yi Zhang M.Sc.

Research supervisors
Prof. Colette McDonagh
Dr. Margaret Brennan-Fournet

School of Physical Sciences
Dublin City University

September 2013

Declaration

I hereby certify that this material, which I now submit for assessment on the programme of study leading to the award of Doctor of Philosophy is entirely my own work, and that I have exercised reasonable care to ensure that the work is original, and does not to the best of my knowledge breach any law of copyright, and has not been taken from the work of others save and to the extent that such work has been cited and acknowledged within the text of my work.

Signed: _____ (Candidate) ID No.: _____

Date: _____

Acknowledgments

I would like to express my gratitude to Prof. Colette McDonagh and Dr. Margaret Brennan-Fournet for their guidance and support throughout the course of this project. Thank you for giving me the opportunity to carry out my Ph.D. study in your groups.

Sincere thanks to Dr. Muriel Voisin, Dr. Deirdre Ledwith and Dr. Patrick Fournet for their support and advice throughout the first year of the project in NUIG.

I am very grateful to Dr. Gemma Keegan for her help with the work that I carried out in DCU. Thank you for giving me advice on all things chemistry and proofreading the drafts of my thesis.

Finally, I would like to thank my parents and friends for their love and encouragement throughout my stay in Ireland.

Table of Contents

Abstract

Noble metal nanoparticles exhibit a unique optical property known as localized surface plasmon resonance (LSPR), which occurs when interacting light couples to the collective oscillations of the surface electrons. This work investigates the use of various nanoparticles for biosensing based on LSPR.

Triangular silver nanoplates (TSNPs), synthesized using two different methods, and their derivatives, gold-coated TSNPs (AuTSNPs), were investigated for use in refractive index sensitivity-based solution assays. Refractive index sensitivities of these nanoplates were determined and benchmarked against the theoretical calculation predicted by Miller *et al.*. The first generation TSNPs and AuTSNPs were used for the detection of human C-reactive protein (CRP) and cardiac troponin I (cTnI) and the second generation AuTSNPs were used for the detection of human CRP. In order to address the complex assay design, a simpler aggregation-based assay for the detection of human IgG was implemented using spherical gold nanoparticles. Furthermore, a preliminary study on incorporating the AuTSNPs into a surface plasmon resonance (SPR) sensor was carried out to explore the enhancement effect of the nanoplates on SPR detection.

Nobel metal nanoparticles are found to enhance fluorescence-based biosensing due to a phenomenon known as metal-enhanced fluorescence (MEF) when the nanoparticles are in the vicinity of fluorophores. In this work, the enhancement effects of the AuTSNPs and spherical silver nanoparticles (AgNPs) on the fluorescence were evaluated. A significant enhancement was observed for AgNPs whereas no enhancement was observed for AuTSNPs. Further MEF studies were conducted using various dyes and gold-coated AgNPs. AgNPs were used for enhancing the fluorescence-based assays for human IgG and CRP detection. The limits of detection (LODs) of the IgG and CRP assays were improved by ~ 9-fold and ~ 19-fold, respectively.

This work establishes the potential of plasmonic nanoparticles for highly sensitive biosensing and holds much promise for the improvement of biomedical diagnostics.

Abbreviations

A	Absorbance
AA	Ascorbic acid
aCRP	Anti-human CRP
ADDLs	Amyloid-β derived diffusible ligands
AFM	Atomic force microscopy
AgNPs	Spherical silver nanoparticles
aIgG	Anti-human IgG
AMI	Acute myocardial infarction
aTnI	Anti-Troponin I
AU	Arbitary units
AuNPs	Spherical gold nanoparticles
AuTSNPs	Gold-coated triangular silver nanoplates
BB	Borate buffer
BDI	Biomedical Diagnostics Institute
BNP	B-type natriuretic peptide
BSA	Bovine serum albumin
C	Constant
C2	Anti-human CRP monoclonal antibody C2
C6	Anti-human CRP monoclonal antibody C6
CCD	Charge coupled device
CK	Creatinine kinase
CKMB	Creatinine kinase myocardial isoenzyme
CRP	C-reactive protein
cTnI	Cardiac troponin I
CV	Coefficient of variation
DCU	Dublin City University

DDA	Discrete dipole approximation
dH_2O	Distilled water
DLS	Dynamic Light Scattering
DNA	Deoxyribonucleic acid
EBL	Electron beam lithography
ELISA	Enzyme-linked immunosorbent assay
Fab	Fragment antigen-binding
Fc	Fragment crystallizable
FDTD	Finite difference time domain method
FIB	Focused ion beam
H	Heavy chain
h	hour
hCG	human chorionic gonadotrophin
hs-CRP	high-sensitivity CRP
IC	Internal Conversion
IgG	Immunoglobulin G
IL	Immunoluminometric
IP	Intellectual Property
IT	Immunoturbidimetric
L	Light chain
LbL	Layer-by-layer
LOD	Limit of detection
LSPR	Localized surface plasmon resonance
mAb	Monoclonal antibody
MEF	Metal-enhanced fluorescence
MES	2-(N-Morpholino)ethanesulfonic acid
MI	Myocardial infarction
min	Minute
MLWA	Modified long wavelength approximation

MMP	Multiple multipole method
M_W	Molecular weight
MWCO	Molecular weight cut off
NSL	Nanosphere lithography
NUIG	National university of Ireland, Galway
PAH	Poly(allylamine) hydrochloride
PB	Phosphate buffer
PBS	Phosphate buffered saline
PBST	Phosphate buffered saline with Tween 20
PC	Cytidine 5'-diphosphocholine
PCS	Photon Correlation Spectroscopy
PEI	Poly(ethyleneimine)
PEL	Polyelectrolyte
PMT	Photomultplier tube
PSA	Prostate specific antigen
PSS	Poly(sodium 4-styrenesulfonate)
RIU	Refractive index unit
RU	Response unit
SAMs	Self assembled monolayers
s	Second
SD	Standard deviation
SDS	Sodium dodecyl sulfate
SERS	Surface enhanced Raman scattering
SIF	Silver Island Film
SPR	Surface plasmon resonance
SPs	Surface Plasmons
TCD	Trinity College Dublin
TEM	Transmission Electron Microscopy
TSC	Trisodium citrate

TSNPs	Triangular silver nanoplates
UCD	University College Dublin
UV–vis	Ultraviolet–visible
V	Variable
v/v	Volume per unit volume
w/v	Weight per unit volume
ε	Molar extinction coefficient
λ_{max}	Maximum wavelength

Chapter 1

Introduction

1.1 Background

In recent years there has been an increasing demand for highly sensitive detection of biomolecules such as proteins and nucleic acids in the biomedical area. Along with the rapid development of nanotechnology, optical sensing based on noble metal nanoparticles has paved a way for detecting biomolecules at low concentrations for biomedical applications. The work presented in this thesis explores the application of noble metal nanoparticles in the detection of proteins by taking advantage of their unique optical property known as localized surface plasmon resonance (LSPR). In this work, LSPR has been integrated in a range of assay designs including refractive index sensitivity-based, aggregation-based, surface plasmon resonance (SPR)-based and fluorescence-based assays. This opening chapter provides a brief overview of noble metal nanoparticles and their applications in the biomedical area. This is followed by an outline of the thesis structure and a statement of the main objectives of the work.

1.2 Noble metal nanoparticles

1.2.1 Historical development

Noble metal nanoparticles are referred to as the particles produced from noble metals which have at least one dimension of the order of 100 nm or less. Noble metal nanoparticles, especially gold and silver nanoparticles, exhibit intense scattering and absorption of light in the visible spectrum which is the source of the beautiful colors in stained glass. Gold nanoparticles are probably the first nanomaterial used for therapeutic and decorative purposes, which can date back to 5^{th} or 4^{th} century B.C. in Egypt and China.[1] A well-known example is the Lycurgus Cup that was fabricated in 4^{th} century A.D. It displays red in transmitted light and green in reflected light, due to the presence of colloidal gold and silver in the glass (Figure 1.1).

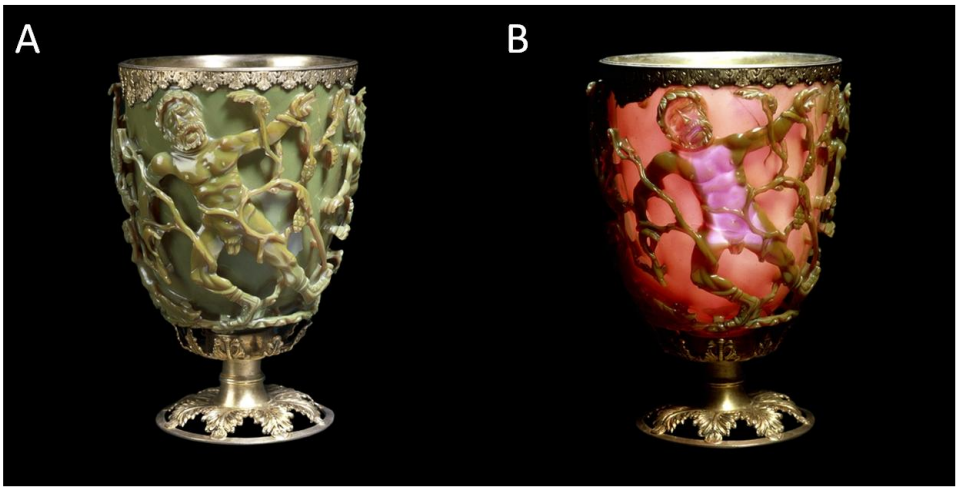

Figure 1.1 The Lycurgus Cup, appearing green in reflected light (A) and red in transmitted light (B). Courtesy of the British Museum.

In 1857, Faraday reported the first scientific article on the synthesis of gold nanoparticles and he was the first to attribute the red color to finely divided gold particles.[2] In 1908, Mie developed a solution to Maxwell's equations that describes the scattering and absorption spectra of spherical particles of arbitrary size.[3] At present, the most common approach to the synthesis of noble metal nanoparticles involves chemical reduction of a metal salt in a solution containing a stabilizer, which limits the growth of the nanoparticles, controls their shape and improves their stability.[4, 5] While most of the one-step synthesis tends to yield approximately spherical nanoparticles,[6, 7] seed-mediated growth is used to fabricate non-spherical nanoparticles of controllable shape and size such as nanorods,[8-11] nanocubes,[12] nanodiscs[13] and nanoprisms.[14, 15] In seed-mediated syntheses, seed particles are first formed by the reduction of a metal salt in a solution. Next, the nanoparticles are grown by adding the seeds to a growth solution where the metal salt is reduced directly on the surface of the seed particles. Detailed information on morphology control by colloidal methods can be found in reviews.[16, 17] Additionally, metal nanostructures on substrates can be fabricated using scanning beam lithographies such as electron beam lithography (EBL)[18-20] and focused ion beam (FIB).[21, 22] These techniques allow the preparation of patterned nanostructures with accurate control of size, shape and spatial distribution. However, the cost of such techniques is usually high and the patterned areas are small. Nanosphere lithography (NSL)[23, 24] is an inexpensive and large scale method that involves evaporation of a metal on a close-packed monolayer of polystyrene nanospheres which serves as a material

deposition mask. Following the removal of the nanospheres, a periodic array of triangle-shaped nanoparticles remains on the substrate.

1.2.2 Current applications in biomedicine

As numerous research efforts have been made to fabricate various noble metal nanoparticles and to investigate their optical properties, more and more studies have been carried out on the applications of these particles. Biomedicine is one of the most attractive fields where the use of gold and silver nanoparticles has been explored broadly. The potential biomedical applications of these particles primarily include biosensing/diagnosis,[25-27] imaging[28-30], targeted drug delivery[31-33] and therapy.[34-37]

The unique optical properties of noble metal nanoparticles (i.e. LSPR) provide a platform for biosensing by means of transducing a molecular recognition-induced change into a quantifiable signal. This type of application is typically developed on the basis of the following mechanisms: (i) local refractive index changes,[26, 38-40] (ii) nanoparticle aggregation,[41-46] (iii) surface enhanced Raman scattering (SERS)[47-51] and (iv) metal-enhanced fluorescence (MEF).[52-57] The signal measurement techniques mainly involve ultraviolet–visible (UV–vis) spectroscopy, dark-field microscopy, Raman spectroscopy and fluorescence spectroscopy. In addition, LSPR has been incorporated into the SPR biosensing to further amplify the signal.[58-62] While the utilization of nanoparticles for biosensing is mostly active in the research laboratory, a few technologies have been commercialized. A good example is Nanosphere's Verigene System which involves gold nanoparticle-based diagnostic applications including clinical microbiology tests, cardiac tests, human genetic tests and pharmacogenetic tests.[63] During the course of my PhD program, a company called Plasmonix now sells the silver nanoparticle-coated 96-well microplates that are used for fluorescence-based assays to improve the assay sensitivities.[64]

The scattering from a single gold or silver nanoparticle has been found to be many orders of magnitude greater than the signal from single fluorophores or quantum dots.[65, 66] Additionally, unlike fluorophores, nanoparticles neither photobleach or blink. These effects enable them to enhance the contrast of imaging systems based on microscopy such as dark-field microscopy for imaging cells and a microarray-based DNA assay.[29, 30, 67] Gold and silver nanoparticles have also been used as imaging labels for cell and

tissue imaging with surface enhanced Raman spectroscopy.[68-70] In a fluorescence imaging study, silver nanoparticle-fluorophore coupled molecular probes have been developed for single cell imaging using scanning confocal microscopy.[71] This approach provides a promising imaging agent with increased brightness, decreased lifetime and improved photostability.

Recently, gold nanoparticles have been used as drug delivery systems due to their biocompatibility, optical properties and outstanding abilities to conjugate with small molecules like ligands, DNA and drugs.[72] The absorption of light by noble metal nanoparticles yields a nanoscopic heat source, thus enabling thermal ablation treatment to tumors by locally and specifically applying heat to the diseased tissue.[34, 73] A detailed review on the therapeutic applications of noble metal nanoparticles can be found in this article.[74]

1.2.3 Roles of noble metal nanoparticles in this thesis

This thesis focuses on the development of biosensing applications based on noble metal nanoparticles for potential diagnostic tests. Specifically, two main nanoparticle applications have been explored in this work. Firstly, nanoparticles, conjugated with specific probes, are used as biosensors to detect target analyte molecules including human C-reactive protein (CRP), human cardiac troponin I (cTnI) and human IgG. Secondly, nanoparticles are used as enhancers to amplify the signals from SPR and fluorescence-based assays. Both of these roles are based on their unique optical properties, i.e. LSPR.

1.3 Thesis structure

This thesis consists of seven chapters.

Chapter 1 briefly introduces the development of noble metal nanoparticles and their applications in the field of biomedical sciences. A description of the roles that the nanoparticles play in this thesis is given. An outline of the thesis and the research objectives are presented.

Chapter 2 describes the relevant background of immunoassays, the fundamental theories of fluorescence and the distinct optical properties of noble metal nanoparticles. The

principles of MEF are discussed. A review of biosensing based on LSPR in relation to this work is given.

Chapter 3 describes the main characterization techniques used in this work.

Chapter 4 reports the early work carried out at the National University of Ireland, Galway (NUIG) during the first year of my PhD program, where I worked on unique triangular nanoplates which had been developed by Prof. John Kelly in Trinity College, Dublin (TCD) and referred to the Kelly particles in this thesis. Prof. Kelly and one of my supervisors, Dr. Brennan-Fournet, optimized the refractive index sensitivities of these particles and my initial task was to investigate their use for highly sensitive homogeneous assays in solution. Dr. Brennan-Fournet moved to DCU after the first year and, due to intellectual property (IP) restrictions, my work on the Kelly particles had to be discontinued. The work presented here is preliminary work towards the use of the particles in real assays.

Chapter 5 reports the development of homogenous assays using alternative triangular nanoplates and spherical gold nanoparticles (AuNPs). Firstly, a refractive index sensitivity-based assay using the alternative triangular nanoplates is described. Next, an aggregation-based assay using AuNPs is presented. In the last section of Chapter 5, preliminary work on a nanoparticle-enhanced SPR assay using triangular nanoplates is described.

Chapter 6 reports the development of a fluorescence-based, solid-phase assay enhanced by noble metal nanoparticles. Firstly, the comparison of the enhancement effect of triangular nanoplates and spherical silver nanoparticles (AgNPs) on the fluorescence is presented. Secondly, the enhancement effect for two different dyes is outlined. This is followed by an investigation of the enhancement effect on the gold-coated AgNPs. Next, MEF assays using AgNPs are described.

Chapter 7 summarizes the results obtained during the work and evaluates the results in the context of the state-of-the art for assays for the various analytes. Finally, the future work is also described.

1.4 Research objectives

The central objective of this work was to develop LSPR assays with improved sensitivity for application in point-of-care diagnostics. Both solution-based and solid platform-based approaches were used and transduction methods ranged from refractive index-based, to aggregation, SPR and finally MEF.

The specific objectives are:

1. To experimentally investigate refractive index sensitivity-based assays using solution-phase triangular nanoplates
2. To experimentally investigate aggregation-based assays using solution-phase spherical AuNPs and to explore the potential of enhanced SPR detection using AuTSNPs.
3. To experimentally investigate MEF-based assays using silver and gold nanostructures on solid substrates.

References

1. M.-C. Daniel and D. Astruc, Chemical Reviews **104** (1), 293-346 (2004).
2. M. Faraday, Philosophical Transactions of the Royal Society of London **147**, 145-181 (1857).
3. G. Mie, Annalen der Physik **330** (3), 377-445 (1908).
4. A. Roucoux, J. Schulz and H. Patin, Chemical Reviews **102** (10), 3757-3778 (2002).
5. G. B. Khomutov and Y. A. Koksharov, Advances in Colloid and Interface Science **122** (1–3), 119-147 (2006).
6. G. Frens, Nature-Physical Science **241** (105), 20-22 (1973).
7. Z. S. Pillai and P. V. Kamat, The Journal of Physical Chemistry B **108** (3), 945-951 (2003).
8. C. J. Murphy, T. K. Sau, A. Gole and C. J. Orendorff, MRS Bulletin **30** (05), 349-355 (2005).
9. N. R. Jana, L. Gearheart and C. J. Murphy, Advanced Materials **13** (18), 1389-1393 (2001).
10. N. R. Jana, L. Gearheart and C. J. Murphy, Chemical Communications (7), 617-618 (2001).
11. M. Iqbal, Y.-I. Chung and G. Tae, Journal of Materials Chemistry **17** (4), 335-342 (2007).
12. Q. Zhang, W. Li, C. Moran, J. Zeng, J. Chen, L.-P. Wen and Y. Xia, Journal of the American Chemical Society **132** (32), 11372-11378 (2010).
13. S. Chen, Z. Fan and D. L. Carroll, The Journal of Physical Chemistry B **106** (42), 10777-10781 (2002).
14. D. Aherne, D. M. Ledwith, M. Gara and J. M. Kelly, Advanced Functional Materials **18** (14), 2005-2016 (2008).
15. S. Chen and D. L. Carroll, Nano Letters **2** (9), 1003-1007 (2002).
16. M. Grzelczak, J. Perez-Juste, P. Mulvaney and L. M. Liz-Marzan, Chemical Society Reviews **37** (9), 1783-1791 (2008).
17. A. R. Tao, S. Habas and P. Yang, Small **4** (3), 310-325 (2008).
18. W. Rechberger, A. Hohenau, A. Leitner, J. R. Krenn, B. Lamprecht and F. R. Aussenegg, Optics Communications **220** (1–3), 137-141 (2003).

19. J. Grand, P.-M. Adam, A.-S. Grimault, A. Vial, M. Lamy de la Chapelle, J.-L. Bijeon, S. Kostcheev and P. Royer, Plasmonics **1** (2-4), 135-140 (2006).
20. L. Gunnarsson, T. Rindzevicius, J. Prikulis, B. Kasemo, M. Käll, S. Zou and G. C. Schatz, The Journal of Physical Chemistry B **109** (3), 1079-1087 (2004).
21. A. G. Brolo, R. Gordon, B. Leathem and K. L. Kavanagh, Langmuir **20** (12), 4813-4815 (2004).
22. T. Ohno, J. A. Bain and T. E. Schlesinger, Journal of Applied Physics **101** (8), 083107-083104 (2007).
23. T. R. Jensen, M. L. Duval, K. L. Kelly, A. A. Lazarides, G. C. Schatz and R. P. Van Duyne, The Journal of Physical Chemistry B **103** (45), 9846-9853 (1999).
24. C. L. Haynes and R. P. Van Duyne, The Journal of Physical Chemistry B **105** (24), 5599-5611 (2001).
25. J. J. Storhoff, A. A. Lazarides, R. C. Mucic, C. A. Mirkin, R. L. Letsinger and G. C. Schatz, Journal of the American Chemical Society **122** (19), 4640-4650 (2000).
26. A. J. Haes, W. P. Hall, L. Chang, W. L. Klein and R. P. Van Duyne, Nano Letters **4** (6), 1029-1034 (2004).
27. S.-H. Yeom, M.-E. Han, B.-H. Kang, K.-J. Kim, H. Yuan, N.-S. Eum and S.-W. Kang, Sensors and Actuators B: Chemical **177** (0), 376-383 (2013).
28. T. Huang, P. D. Nallathamby and X.-H. N. Xu, Journal of the American Chemical Society **130** (50), 17095-17105 (2008).
29. S. J. Oldenburg, C. C. Genick, K. A. Clark and D. A. Schultz, Analytical Biochemistry **309** (1), 109-116 (2002).
30. X.-H. N. Xu, W. J. Brownlow, S. V. Kyriacou, Q. Wan and J. J. Viola, Biochemistry **43** (32), 10400-10413 (2004).
31. A. G. Tkachenko, H. Xie, D. Coleman, W. Glomm, J. Ryan, M. F. Anderson, S. Franzen and D. L. Feldheim, Journal of the American Chemical Society **125** (16), 4700-4701 (2003).
32. S. Gurunathan, K.-J. Lee, K. Kalishwaralal, S. Sheikpranbabu, R. Vaidyanathan and S. H. Eom, Biomaterials **30** (31), 6341-6350 (2009).
33. P. Mukherjee, R. Bhattacharya, P. Wang, L. Wang, S. Basu, J. A. Nagy, A. Atala, D. Mukhopadhyay and S. Soker, Clinical Cancer Research **11** (9), 3530-3534 (2005).

34. L. R. Hirsch, R. J. Stafford, J. A. Bankson, S. R. Sershen, B. Rivera, R. E. Price, J. D. Hazle, N. J. Halas and J. L. West, Proceedings of the National Academy of Sciences of the United States of America **100** (23), 13549-13554 (2003).
35. C. Loo, A. Lowery, N. Halas, J. West and R. Drezek, Nano Letters **5** (4), 709-711 (2005).
36. I. H. El-Sayed, X. Huang and M. A. El-Sayed, Cancer Letters **239** (1), 129-135 (2006).
37. X. Huang, I. H. El-Sayed, W. Qian and M. A. El-Sayed, Journal of the American Chemical Society **128** (6), 2115-2120 (2006).
38. A. J. Haes and R. P. Van Duyne, Journal of the American Chemical Society **124** (35), 10596-10604 (2002).
39. P. L. Truong, B. W. Kim and S. J. Sim, Lab on a Chip **12** (6), 1102-1109 (2012).
40. M. Kreuzer, R. Quidant, J. P. Salvador, M. P. Marco and G. Badenes, Anal Bioanal Chem **391** (5), 1813-1820 (2008).
41. R. Elghanian, J. J. Storhoff, R. C. Mucic, R. L. Letsinger and C. A. Mirkin, Science **277** (5329), 1078-1081 (1997).
42. J. J. Storhoff, R. Elghanian, R. C. Mucic, C. A. Mirkin and R. L. Letsinger, Journal of the American Chemical Society **120** (9), 1959-1964 (1998).
43. J. J. Storhoff, A. D. Lucas, V. Garimella, Y. P. Bao and U. R. Muller, Nat Biotech **22** (7), 883-887 (2004).
44. N. T. K. Thanh and Z. Rosenzweig, Analytical Chemistry **74** (7), 1624-1628 (2002).
45. Q. Cao, H. Yuan and R. Cai, J. Wuhan Univ. Technol.-Mat. Sci. Edit. **24** (5), 772-775 (2008).
46. L. R. Hirsch, J. B. Jackson, A. Lee, N. J. Halas and J. L. West, Analytical Chemistry **75** (10), 2377-2381 (2003).
47. Y. C. Cao, R. Jin and C. A. Mirkin, Science **297** (5586), 1536-1540 (2002).
48. S. P. Mulvaney, M. D. Musick, C. D. Keating and M. J. Natan, Langmuir **19** (11), 4784-4790 (2003).
49. L. Seballos, J. Zhang and R. Sutphen, Anal Bioanal Chem **383** (5), 763-767 (2005).
50. L. Sun, C. Yu and J. Irudayaraj, Analytical Chemistry **79** (11), 3981-3988 (2007).

51. S. Abalde-Cela, P. Aldeanueva-Potel, C. Mateo-Mateo, L. Rodríguez-Lorenzo, R. A. Alvarez-Puebla and L. M. Liz-Marzán, Journal of The Royal Society Interface (2010).
52. C. Lobmaier, G. Hawa, M. Götzinger, M. Wirth, F. Pittner and F. Gabor, Journal of Molecular Recognition **14** (4), 215-222 (2001).
53. N. Lochner, C. Lobmaier, M. Wirth, A. Leitner, F. Pittner and F. Gabor, European Journal of Pharmaceutics and Biopharmaceutics **56** (3), 469-477 (2003).
54. E. Matveeva, Z. Gryczynski, J. Malicka, I. Gryczynski and J. R. Lakowicz, Analytical Biochemistry **334** (2), 303-311 (2004).
55. E. G. Matveeva, Z. Gryczynski and J. R. Lakowicz, Journal of Immunological Methods **302** (1–2), 26-35 (2005).
56. R. Nooney, A. Clifford, X. LeGuevel, O. Stranik, C. McDonagh and B. MacCraith, Anal Bioanal Chem **396** (3), 1127-1134 (2010).
57. Y.-F. Chang, J.-S. Yu, Y.-T. Chang, L.-C. Su, C.-C. Wu, Y.-S. Chang, C.-S. Lai and C. Chou, Biosensors and Bioelectronics **41** (0), 232-237 (2013).
58. L. A. Lyon, M. D. Musick and M. J. Natan, Analytical Chemistry **70** (24), 5177-5183 (1998).
59. B. H. Schneider, E. L. Dickinson, M. D. Vach, J. V. Hoijer and L. V. Howard, Biosensors and Bioelectronics **15** (1–2), 13-22 (2000).
60. U. Pieper-Fürst, U. Kleuser, W. F. M. Stöcklein, A. Warsinke and F. W. Scheller, Analytical Biochemistry **332** (1), 160-167 (2004).
61. H. R. Sim, A. W. Wark and H. J. Lee, Analyst **135** (10), 2528-2532 (2010).
62. M. J. Kwon, J. Lee, A. W. Wark and H. J. Lee, Analytical Chemistry **84** (3), 1702-1707 (2012).
63. http://www.nanosphere.us/.
64. http://plasmonixinc.com/.
65. J. Yguerabide and E. E. Yguerabide, Analytical Biochemistry **262** (2), 157-176 (1998).
66. S. Schultz, D. R. Smith, J. J. Mock and D. A. Schultz, Proceedings of the National Academy of Sciences of the United States of America **97** (3), 996-1001 (2000).

67. T. Huang, P. D. Nallathamby, D. Gillet and X.-H. N. Xu, Analytical Chemistry **79** (20), 7708-7718 (2007).
68. J.-H. Kim, J.-S. Kim, H. Choi, S.-M. Lee, B.-H. Jun, K.-N. Yu, E. Kuk, Y.-K. Kim, D. H. Jeong, M.-H. Cho and Y.-S. Lee, Analytical Chemistry **78** (19), 6967-6973 (2006).
69. Q. Hu, L.-L. Tay, M. Noestheden and J. P. Pezacki, Journal of the American Chemical Society **129** (1), 14-15 (2007).
70. C. L. Zavaleta, B. R. Smith, I. Walton, W. Doering, G. Davis, B. Shojaei, M. J. Natan and S. S. Gambhir, Proceedings of the National Academy of Sciences **106** (32), 13511-13516 (2009).
71. J. Zhang, Y. Fu, D. Liang, K. Nowaczyk, R. Y. Zhao and J. R. Lakowicz, Nano Letters **8** (4), 1179-1186 (2008).
72. G. Han, P. Ghosh and V. M. Rotello, Nanomedicine **2** (1), 113-123 (2007).
73. X. Huang, P. K. Jain, I. H. El-Sayed and M. A. El-Sayed, Photochemistry and Photobiology **82** (2), 412-417 (2006).
74. R. R. Arvizo, S. Bhattacharyya, R. A. Kudgus, K. Giri, R. Bhattacharya and P. Mukherjee, Chemical Society Reviews **41** (7), 2943-2970 (2012).

Chapter 2

Theory and background

2.1 Introduction

This chapter introduces the main elements of the work carried out, including the relevant background to immunoassays, the fundamentals of fluorescence theory, the concepts behind nanoparticle local surface plasmon resonance and the principles of plasmonic enhancement of fluorescence, herein referred to as metal-enhanced fluorescence (MEF). Also included is a comprehensive state-of-the-art review of LSPR biosensing based on cutting edge technologies and mechanisms.

2.2 Assays and Immunoassays

An assay is an analytical method that identifies and quantifies a substance. It is primarily used in pharmaceutical, food testing, biological, chemical and medical areas. An immunoassay is a ligand-binding assay that measures an analyte in a biological mixture through a specific antibody-antigen reaction.[1] Immunoassays are being extensively employed in research laboratories and clinical diagnostics.

An antibody, also known as immunoglobulin, is a protein produced by B cells in response to a foreign molecule (i.e. antigen). Its functionality enables it to specifically recognize and binds to a defined structure (i.e. epitope) on an antigen. Monoclonal antibodies produced by a single B cell clone recognize only one epitope, whereas polyclonal antibodies produced by multiple B cell clones recognize different epitopes on one antigen.[2] Figure 2.1 illustrates a simplified structure of an antibody molecule. Typically, the antibody is depicted as a Y-shaped molecule comprising of two identical heavy chains and two identical light chains. Each chain contains both a variable (V) and a constant (C) region. Functionally, the antibody consists of two important parts including the Fab (fragment, antigen binding) region and Fc (Fragment, crystallizable) region. The Fab region is composed of one constant and one variable domain from each heavy and light chain, which contains the antigen binding site of the antibody. The

interaction between the antibody and antigen, similar to a lock and key, involves non-covalent bonds including hydrogen bonds, ionic bonds, hydrophobic interactions and Van der Waals forces.[3] There are many factors affecting the antibody-antigen reaction such as temperature, pH, ionic strength and duration of incubation time.[3] The antibody-antigen reaction can be optimized by adjusting these factors. The Fc region is the base of the antibody that plays a role in modulating immune cell activity.

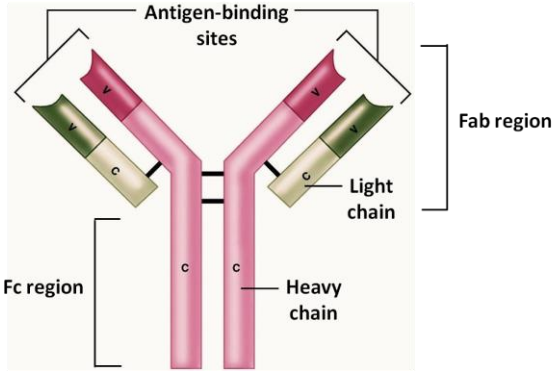

Figure 2.1 Simplified structure of an antibody molecule. Adapted from reference.[4]

2.2.1 Immunoassay classifications

Immunoassays can be classified in different ways and a thorough description of the immunoassay designs and formats can be found in reference.[5] In this chapter, the immunoassay formats used in this work are described below.

2.2.1.1 Homogeneous and heterogeneous immunoassays

Based on the requirement of separation steps in an assay, immunoassays are classified as homogeneous or heterogeneous. Homogeneous immunoassays only involve the combination of an analyte and the reagents followed by detection.[5] They do not require the physical separation of antibody-bound components from the free ones, which generally shortens the assay time and reduces the requirements for automation.[5] On the other hand, heterogeneous immunoassays require separation steps, such as washing, in order to physically remove the interfering components from the antibody-analyte complexes.[6] Due to the separation steps, heterogeneous immunoassays can be time-consuming and labor-intensive.

2.2.1.2 Label-free and labeled immunoassays

Depending on whether a label is introduced to the assay system, immunoassays are classified as labeled or label-free. Most conventional immunoassays use a label (e.g. radioisotope, enzyme or fluorophore) conjugated with one or more components in the assay system to generate detectable signals.[7] These assays can be easily quantified because the number of antibody-antigen bindings is usually proportional to the level of the signal produced by the labels. Recently, label-free immunoassays have been widely developed, which are independent of labels for detection. A well known example of such an assay is based on SPR which detects the changes of reflective index in the vicinity of a thin metal film due to the occurrence of antibody-antigen bindings on the film.[8] Noble metal nanoparticles have recently shown promise when employed in immunoassays. The performance of these assays is based on LSPR and both label-free and labeled formats have used.[9-11] In these assays, the shifts in the LSPR wavelength are measured, depending on the refractive index changes of the local medium that are induced by the antibody-antigen bindings on the nanoparticle surface.

2.2.1.3 Direct and sandwich immunoassays

The direct immunoassay is usually considered to be the simplest form of immunoassay since it requires only one antibody for the specific detection of a target antigen. Figure 2.2 A illustrates an example of a direct immunoassay using a solid phase, where the antibody is immobilized on a substrate. The concentration of the antigen is determined by measuring the signal of the labeled antigen which is captured by the antibody. This type of assay is relatively fast due to the simple procedure. The sandwich immunoassay involves the measurement of antigen between a layer of capture antibody and a layer of detection antibody. The antigen must contain at least two epitopes since at least two antibodies react with it. Figure 2.2 B illustrates a solid-phase sandwich immunoassay where the capture antibody is immobilized on a substrate and the detection antibody is conjugated to a label, e.g. a fluorophore. The immobilized antibody captures the antigen from a sample, followed by the introduction of labeled antibody that will bind to the free epitopes of the antigen. The level of signal generated by the labeled antibody is directly proportional to the antigen concentration.

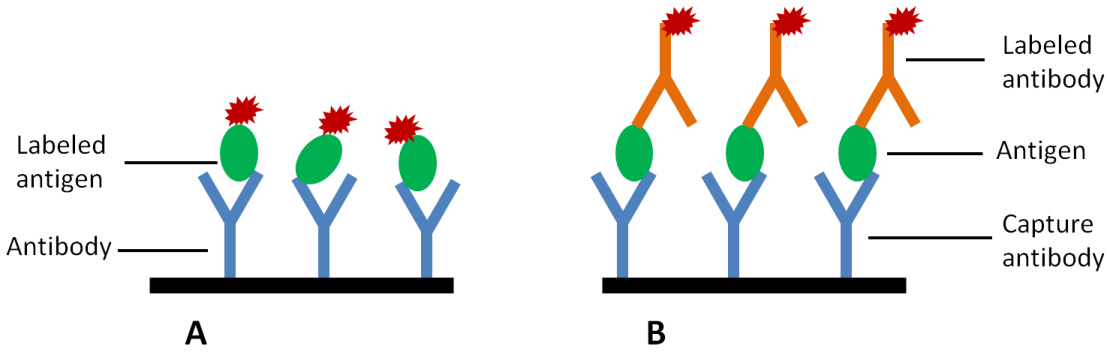

Figure 2.2 Schematic illustrating (A) a direct immunoassay and (B) a sandwich immunoassay.

2.3 Absorption and Fluorescence

Fluorescence is the spontaneous emission of photons from a substance when it relaxes to its ground state after the absorption of photons. The processes of absorption and emission in a substance are demonstrated in the Jablonski diagram shown in Figure 2.3.[12] The singlet ground, first and second electronic states are depicted by S_0, S_1 and S_2, respectively. A fluorescent substance known as a fluorophore is usually excited to a higher vibrational energy level (S_1 or S_2) when absorbing a photon, which occurs in about 10^{-15} s. Immediately following the absorption, the fluorophore may relax to the lowest vibrational level of S_1 by non-radiative decay. This process known as internal conversion generally occurs within 10^{-12} s and completes before emission. The fluorophore then relaxes to its ground state (S_0) by emitting a photon of energy.

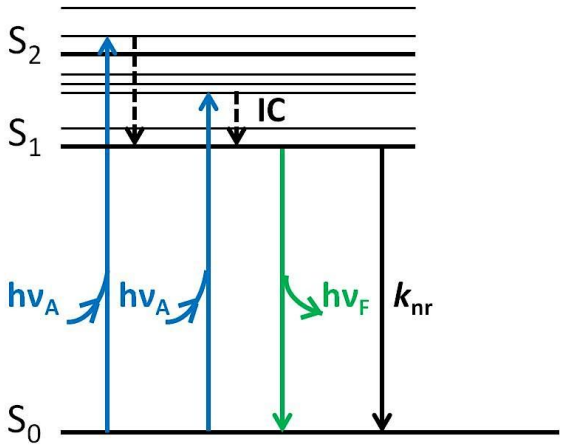

Figure 2.3 Jablonski diagram demonstrating the fluorescence process. IC denotes internal conversion.

The fluorescence quantum yield (ϕ) and lifetime (τ) are critical properties of a fluorophore. The fluorescence quantum yield refers to the ratio of the number of emitted photons to the number of absorbed photons, and is given by

$$\phi = \frac{\Gamma}{\Gamma + k_{nr}} \tag{2.1}$$

where Γ and k_{nr} are the radiative and non-radiative decay rates, respectively. The quantum yield is always less than unity due to energy dissipation.

The lifetime is defined as the average time the fluorophore spends in the excited state prior to emitting a photon of energy, and is expressed as:

$$\tau = \frac{1}{\Gamma + k_{nr}} \tag{2.2}$$

The radiative decay rate is determined by the extinction coefficient of the fluorophore according to the *Strickler–Berg* relationship[13].

$$\Gamma = 2.88 \times 10^9 \, \upsilon_0^{-2} n^2 \frac{g_g}{g_e} \int \varepsilon d\upsilon \tag{2.3}$$

where υ_0 is the wavenumber of the absorption maximum, n is the refractive index of the medium, g_g and g_e are the degeneracies of the ground and the first excited states, ε is the molar extinction coefficient of the fluorophore. Since the extinction coefficient remains nearly constant in various environments, the radiative decay rate does not change substantially under most conditions. Therefore, the changes in quantum yield ϕ and lifetime τ result from changes in the non-radiative decay rate k_{nr}. The values of ϕ and τ either both increase or decrease.

2.4 Surface plasmon resonance

When light interacts with a metal, such as a thin gold or silver film, its surface free electrons oscillate collectively while absorbing, scattering or reradiating the incident photons. The resulting surface electromagnetic waves propagate along the metal surface for distances on the order of tens to hundreds of microns, and decay exponentially in the z-direction with lengths on the order of 200 nm (Figure 2.4).[14-16] As a result of the coherent oscillation of the surface electrons, the intensity of the electromagnetic field in

the z-direction is enhanced by a factor of 10 to 100 compared to the incident intensity.[15] These propagating electromagnetic modes are termed surface plasmon polaritons, but are usually referred to as surface plasmons (SPs). The enhancement of the electromagnetic field at the metal surface results in an extraordinary sensitivity of SPs to surface conditions.

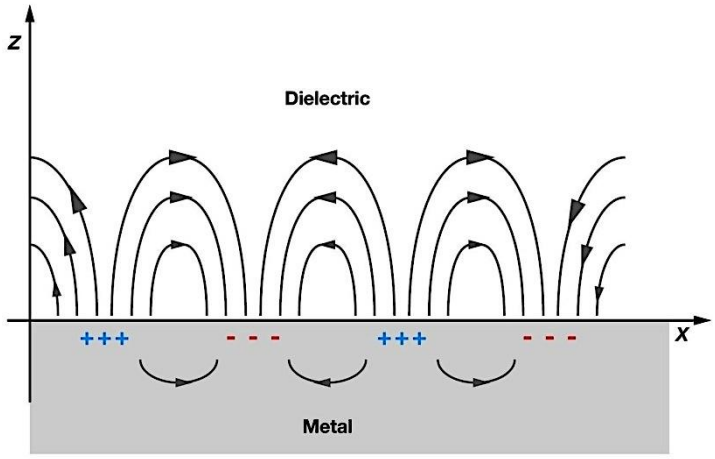

Figure 2.4 Schematic diagram of SPR. Adapted from reference.[16]

2.5 Localized surface plasmon resonance and Mie theory

Nanostructured noble metals such as gold and silver nanoparticles exhibit distinct optical properties from the bulk metals, typically exhibiting strong absorption bands in the visible region. This absorption band originates from the interaction between an electromagnetic field and the free electrons confined on the nanometer scale in the metal. When light interacts with nanoparticles that are much smaller than the incident wavelength the free electrons in the metal move to the surface and oscillate in resonance with the photon's frequency (Figure 2.5).[17] This collective oscillation of conduction electrons is confined to the surface of the nanostructure and is known as localized surface plasmon resonance (LSPR). Consequently, the induced electromagnetic field associated with the LSPR is considerably enhanced in the vicinity of the nanoparticle.

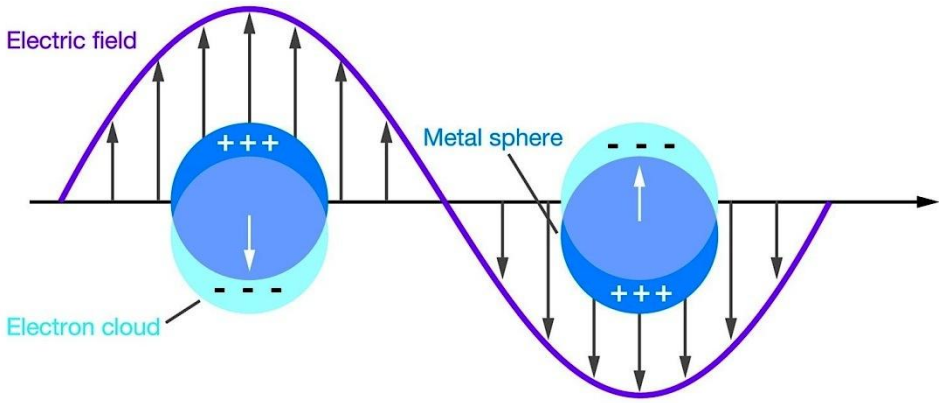

Figure 2.5 LSPR illustrating the oscillation of the electron cloud upon interaction with an electromagnetic field. Adapted from reference.[16]

In 1908 Mie published a paper on a theoretical solution to Maxwell's equations,[18] elucidating the scattering and absorption of electromagnetic radiation incident on a spherical particle of arbitrary material. Mie solution provides the simplest theoretical approach for demonstrating the optical properties of nanoparticles. It is given by,[19]

$$E(\lambda) = \frac{24\pi N_A a^3 \varepsilon_m^{3/2}}{\lambda \cdot \ln(10)} \left[\frac{\varepsilon_i}{(\varepsilon_r + \chi\varepsilon_m)^2 + \varepsilon_i^2} \right] \tag{2.4}$$

where $E(\lambda)$ is the extinction (extinction = scattering + absorption), N_A is the number of nanoparticles, a is the radius of the nanosphere, ε_m is the dielectric constant of the medium surrounding the nanosphere, λ is the wavelength of the absorbing radiation, ε_i and ε_r correspond to the imaginary and real portions of the spherical metal's dielectric function and χ is a shape factor dependent upon the aspect ratio of the nanoparticle (equal to 2 for a sphere). It is evident that the LSPR spectrum of a single metallic nanosphere suspended in a dielectric medium relies on the nanoparticle size (a), material (ε_i and ε_r) and the dielectric constant of the surrounding environment (ε_m). Moreover, the extinction spectrum also depends upon the shape (χ) which becomes an important parameter in the case of non-spherical nanoparticles.

2.5.1 Influence of material: dielectric function

The dielectric properties of a material describe the interaction of electromagnetic radiation with the material. As discussed above, the dielectric properties of noble metal nanoparticles differ from those of the bulk metal such as, unlike bulk metals,

nanoparticles can exhibit strong absorption within the visible spectrum. The two most relevant metals in this work are gold and silver which have similar dielectric properties resulting from the cooperative behavior of the d-band electrons and conduction electrons on the nanoparticle surface.[20] The difference in interband contributions to the plasmon resonance results in gold and silver spherical nanoparticles having plasmon resonance absorption bands at 520 nm and 400 nm respectively for a diameter of ~ 60 nm. The dielectric constant has both real and imaginary contributions with the imaginary contribution contributing to the extinction properties of the nanoparticles. Importantly, silver has an imaginary dielectric constant lower value resulting in its higher extinction. As a result, silver nanoparticles have a factor of ten greater scattering strength than similar gold nanoparticles.[21]

2.5.2 Influence of nanoparticle size

When a particle is illuminated by an electromagnetic field, its electrons can be accelerated and they radiate electromagnetic energy in all directions via scattering processes. Additionally, the excited electrons can also transform the incident electromagnetic energy into other forms such as thermal energy via absorption processes. The sum of both processes is known as extinction.[22] The relative contributions of absorption and scattering to extinction depend on the size and shape of the nanoparticles. In order to examine the size effect on the optical properties of a nanoparticle, a sphere is chosen for simplicity.

For a spherical nanoparticle much smaller than the wavelength of the incident light ($a \leq$ 10 nm), the electric field can be considered spatially constant, with a time dependent phase, which is known as the quasi-static approximation.[23] Within this model, the conduction electrons experience homogenous polarization leading to a dipole mode resonance as depicted in Figure 2.6 A. This resonance is exclusively dependent on the shape of the nanoparticle and the electron density. The LSPR extinction results from the dipole absorption while the scattering process is negligible.[24] The peak position and the width of the LSPR are influenced by the frequency dependent dielectric functions of the noble metals.[23].

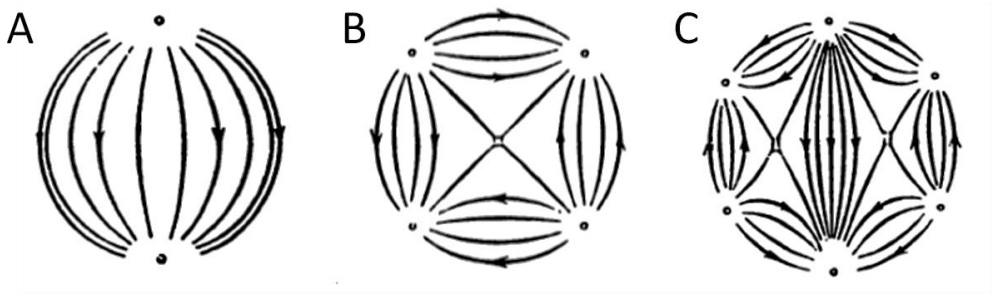

Figure 2.6 Electric field distributions of the (A) dipole, (B) quadrupole and (C) octupole resonances. Adapted from reference.[23]

As the size of nanoparticle increases, the electron density is no longer polarized homogeneously by the incident light, resulting in higher multipole mode resonances such as quadrupole and octupole (Figure 2.6 B and C).[23] Higher order resonances corresponding to individual polarizations of the electron density are observed at shorter wavelengths with respect to the dipole peak.[25-27] In addition, the accelerated electrons in the larger nanoparticle can radiate energy in all directions, which is the scattering process. Due to this secondary radiation, the electrons experience energy loss (radiation damping), shifting the dipole resonance to longer wavelengths and broadening the spectrum.[28] The scattering becomes dominant in the extinction spectra as the size of the nanoparticle increases. Figure 2.7 shows the contributions of absorption and scattering to the extinction for small and large silver nanospheres.[29] For a small nanosphere (a = 22 nm), both absorption and scattering are observed while the former plays a dominant role in the extinction. However, for a large nanosphere (a = 100 nm), the scattering process contributes almost the entire extinction.

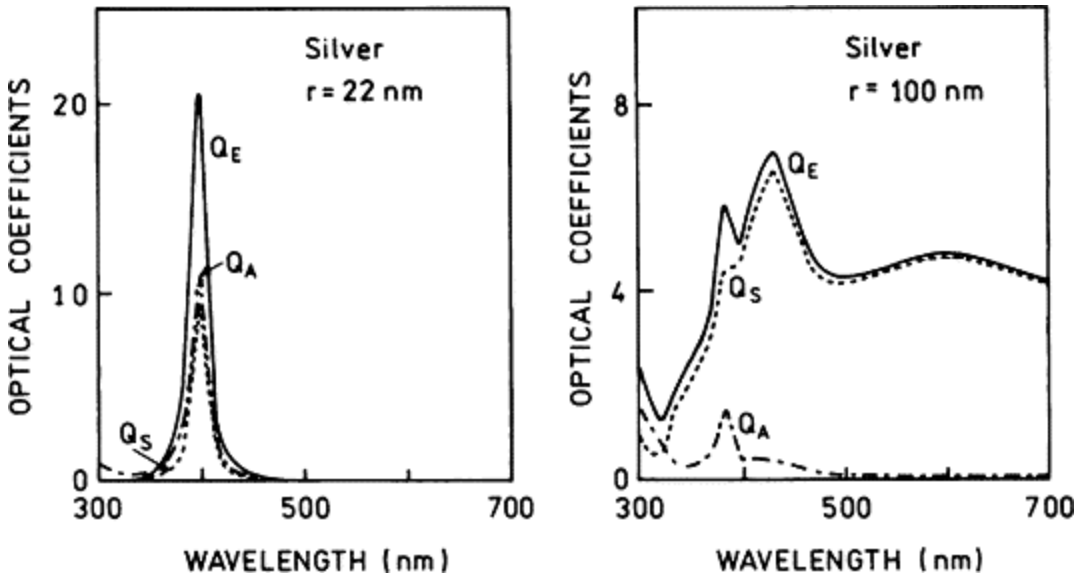

Figure 2.7 Extinction (Q_E), absorption (Q_A) and scattering (Q_S) efficiencies for small and large silver spheres. Adapted from reference.[29]

2.5.3 Influence of nanoparticle shape

Mie theory only provides the exact solution for the spherical case. Although Gans extended this theory to ellipsoids,[30] further theory is required to elucidate the optical response of nanoparticles with arbitrary shapes. Over the past two decades, new numerical methods have been introduced to model complex nanoparticles, including the discrete dipole approximation (DDA),[31, 32] the T-matrix method,[33] the multiple multipole method (MMP),[34] the finite difference time domain method (FDTD)[35] and the modified long wavelength approximation (MLWA).[36]

In essence, the surface plasmon oscillation involves a displacement of the negative charges from the positive nuclei under the action of an incident electromagnetic field. This displacement of the negative charges gives rise to polarization charges at the particle surface and hence the restoring force of the system.[23] The frequency and intensity of plasmon resonances are primarily determined by the surface polarization. Any change in the shape or geometry of the nanoparticle will change the surface polarization and therefore the resonance spectrum. For instance, within the quasistatic regime, an ellipsoid with three different axes presents three distinct dipole modes, differing from a sphere with only one dipole mode.[23] Moreover, as the shape of the nanoparticle becomes less symmetric not only dipole modes with distinct frequencies but also higher multipole modes are induced. Wiley *et al.* demonstrated the optical

properties of different silver nanoparticles in electromagnetic fields using DDA calculations.[37] The low-symmetry nanoparticles display redshifted resonance peaks compared to nanospheres, which is attributed to the corners of the structures where surface charges accumulate.[38, 39] The charge distribution near the corners increases the surface polarization and therefore reduces the restoring force for electron oscillation, which is characterized by a redshift of the resonance peak and the appearance of high multipole modes (Figure 2.8).[37, 40]

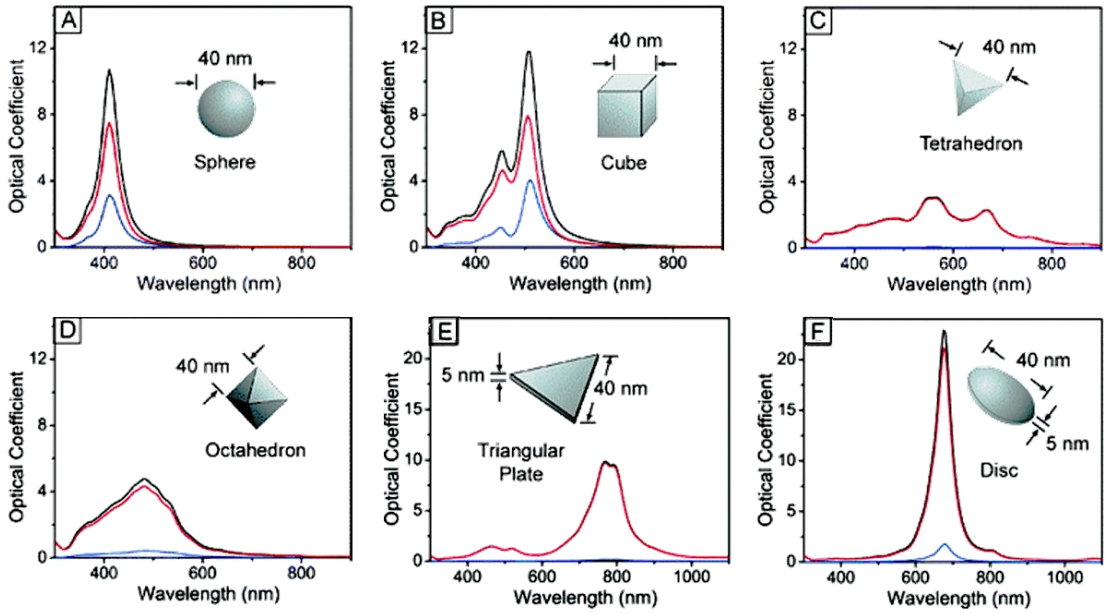

Figure 2.8 The DDA calculated UV-vis extinction (black), absorption (red) and scattering (blue) spectra of silver nanostructures. Adapted from reference.[37]

Haes and coworkers demonstrated electric field enhancement contours around three differently shaped silver nanoparticles with the same volume.[41] The electric field contours near the surfaces, especially at the corners of cubic and pyramidal nanostructures, are observed to be much more intense than those near spherical contours. The highly enhanced electric field is also observed near the sharply curved surface of a silver nanoellipsoid.[36] In the case of triangular nanoplates, the maximum enhancement for the dipole resonances is observed to occur at the tips.[36, 42, 43] Figure 2.9 A shows a spectrum of a silver triangular nanoplate with 100 nm edge length and 16 nm thickness.[44] The 770 nm peak is assigned to the in-plane dipole resonance, the 470 nm peak to the in-plane quadrupole resonance and the 340 nm peak to the out-of-plane

quadrupole resonance. A weak shoulder at 410 nm is assigned to the out-of-plane dipole resonance though it is only weakly visible. Figure 2.9 B shows the electric field enhancement contours near the surface of a silver triangular nanoplate as depicted in Figure 2.9 A.[36] The maximum field for the dipole mode occurs at the nanoplate tips and is approximately 500 times the applied field, leading to enhanced sensitivity to local changes near the tips. This effect renders triangular nanoplates a more attractive candidate than spherical nanoparticles for optical sensing.

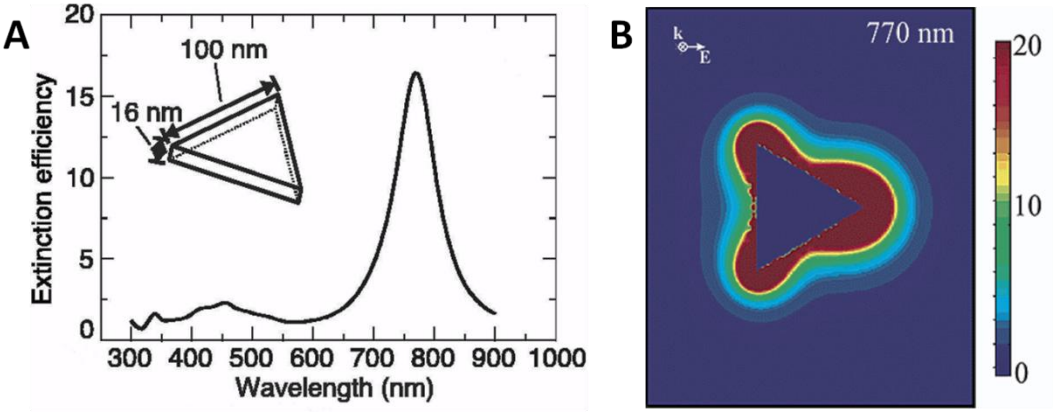

Figure 2.9 (A) DDA simulation of the orientation averaged extinction efficiency spectrum of a silver triangular nanoplate in water (edge length = 100 nm, thickness = 16 nm). (B) Electric field enhancement contours external to the silver triangular nanoplate for an in-plane dipole resonance at 770 nm. Adapted from references.[36, 44]

2.5.4 Influence of dielectric environment: refractive index sensitivity

The electron oscillations confined at the surface of nanoparticles are very sensitive to any change in the metal-dielectric interface. According to equation 2.4, it is apparent that the dielectric constant of the surrounding medium ε_m determines the surface plasmon resonance of the nanoparticle. An increase in the dielectric constant, particularly the refractive index n ($n = {\varepsilon_m}^{1/2}$), of the surrounding medium results in a decrease in the restoring force for the electron oscillation, thus decreasing the plasmon oscillation frequency.[45] In general, the plasmon resonances have been found to shift to longer wavelengths as the refractive index of the local medium is increased. More specifically, the LSPR peak wavelength (λ_{max}) of the nanoparticles has been found to increase linearly with the local refractive index.[46-48] The refractive index sensitivity of

the nanoparticle is defined as a ratio of the change in the LSPR λ_{max} to the change in the local refractive index n, which is $\Delta\lambda_{max}/\Delta n$ (nm/RIU).[49, 50] Refractive index sensitivities ranging from tens to hundreds of nanometers per refractive index unit have been observed within the visible spectral region which in cases rise to values greater than 1000 nm/RIU in the near infra-red spectral region for various nanoparticles such as nanospheres,[51, 52] nanocubes,[51] triangular nanoplates,[53, 54] nanorods[51, 55] and nanoshells.[45, 56]

Miller and Lazarides postulated that the refractive index sensitivities of the nanoparticles are exclusively determined by the LSPR peak wavelengths and the dielectric properties of the material.[50] They showed that the refractive index sensitivity linearly increases with the peak wavelength, regardless of the nanoparticle shape for wavelengths up to 800 nm. Lee and El-Sayed observed that the refractive index sensitivity of the nanorods is independent of the metal composition but primarily dependent on the aspect ratio (i.e. the ratio of the long axis to the short axis) of the structure.[55] In addition, the sensitivity is found to linearly increase with the aspect ratio of the nanorods. Recently, Charles *et al.* have carried out a comprehensive refractive index sensitivity study for solution phase triangular silver nanoplates (TSNPs).[54] It is observed that the refractive index sensitivities of TSNP sols increase linearly with LSPR peak wavelengths up to 800 nm and nonlinearly with the wavelengths in the near infrared region (Figure 2.10 A and B). A maximum refractive index sensitivity of 1096 nm/RIU was obtained at an LSPR peak wavelength of 1093 nm. The refractive index sensitivity is experimentally and theoretically found to linearly increase with the aspect ratio (i.e. the ratio of the edge length to the thickness) of the structures (Figure 2.10 C). The aspect ratio of TSNPs is a key parameter in determining their refractive index sensitivities.[54]

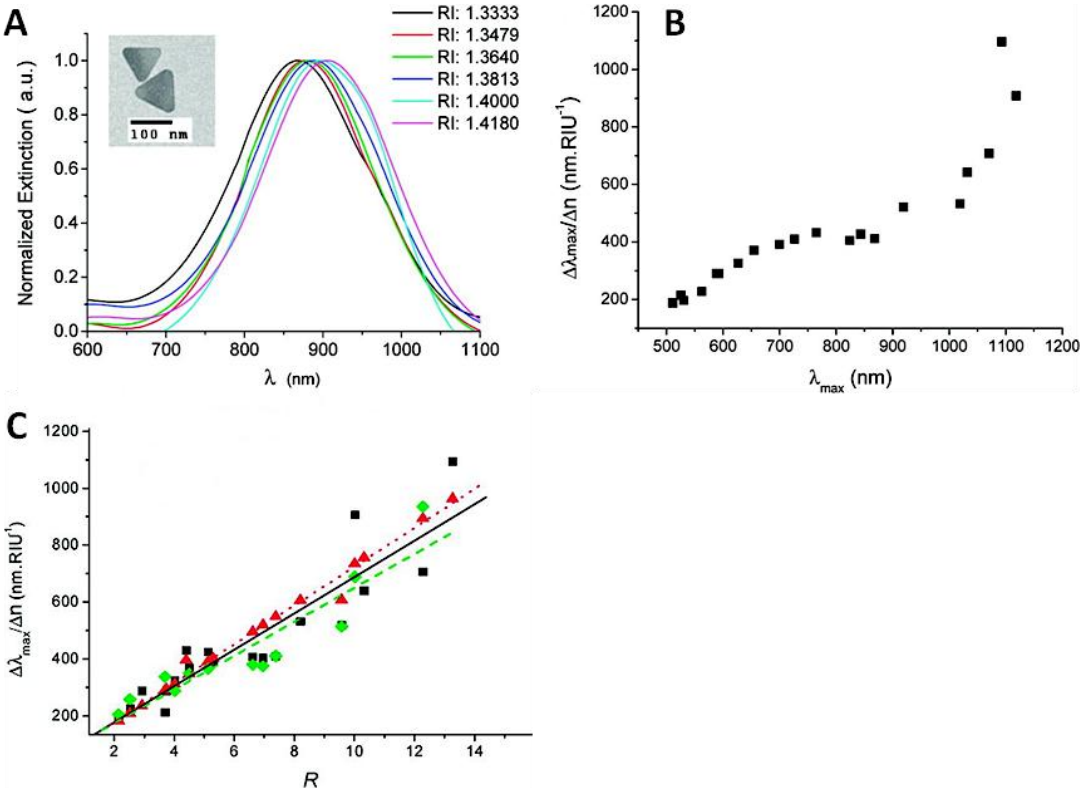

Figure 2.10 (A) An example of the spectral shift observed for a TSNP ensemble exposed to various refractive indices. (B) Plotting of the LSPR λ_{max} of the TSNP sols against the corresponding refractive index sensitivity. (C) The dependence of the refractive index sensitivity on aspect ratio of TSNP (experimental data = black, aspect ratio dependent approximation = red, DDA = green). Adapted from reference.[54]

2.6 Metal-enhanced fluorescence

When a fluorophore is placed in the vicinity of a metal nanoparticle, the optical properties of the fluorophore can be modified and both excitation and emission processes can be enhanced. Figure 2.11 shows the classical Jablonski diagram for the fluorescence process (left) and the modified form illustrating the metal-fluorophore interactions (right). As discussed above in section 2.5, locally enhanced electric fields are observed in the metal nanoparticles due to the collective oscillation of electrons on the metal surface. When a fluorophore is placed near to a metal nanoparticle, its absorption process is enhanced by the increased electric fields, resulting in a subsequent increase in the excitation rate and subsequently the emission intensity.[57] Additionally, the excited-state fluorophore can couple to the surface plasmons of the nearby nanoparticle, generating far-field radiation at the emission wavelength. Through this

mechanism an increase in the emission is observed, accompanied by a decrease in the lifetime.[57]

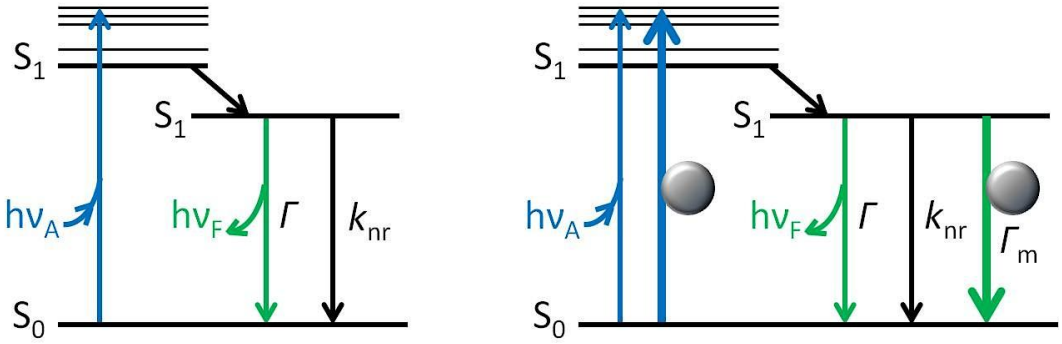

Figure 2.11 Jablonski diagram without (left) and with (right) metal-fluorophore interactions. The thicker arrows represent enhanced excitation and emission rates. Reproduced from reference.[58]

In the case of a fluorophore in the vicinity of a metal nanoparticle, the radiative decay rate is increased and the quantum yield (ϕ_m) and lifetime (τ_m) are given by[12]

$$\phi_m = \frac{\Gamma + \Gamma_{\mathrm{m}}}{\Gamma + \Gamma_{\mathrm{m}} + k'_{nr}} \tag{2.5}$$

$$\tau_m = \frac{1}{\Gamma + \Gamma_{\mathrm{m}} + k'_{nr}} \tag{2.6}$$

where Γ_{m} and k'_{nr} are radiative and non-radiative decay rates induced by the metal nanoparticle, respectively. It is apparent that an increase in the metal-induced radiative decay rate Γ_{m} results in an increased quantum yield and decreased lifetime, an effect which is not observed in classical fluorescence in the absence of metal nanoparticles (equations 2.5 and 2.6). The decreased lifetime is expected to improve the photostability of the fluorophore as less time will be spent in the excited state per excitation/emission cycle. Therefore, fluorophores in the vicinity of metal nanoparticles, with increased quantum yield and decreased lifetime, can emit considerably more photons per second than those in the absence of metal nanoparticles.[59]

2.6.1 Key parameters for MEF

Numerous theoretical and experimental studies have shown that MEF is highly sensitive to the optical properties of metal nanoparticles, the orientation of the fluorophores and the distance between the fluorophore and the nanoparticles.[60-62] Calculations have shown that the maximum enhancement can be achieved when the dipole of the fluorophore is oriented perpendicular to the nearby nanoparticle surface and parallel to the dipole plasmon mode on the nanoparticle.[61, 62] However, the optimization of the fluorophore-nanoparticle configuration can be quite complicated in practice. More practical approaches to achieving effective MEF involve choosing appropriate nanoparticles and varying the fluorophore-nanoparticle distance.

As discussed in section 2.5.2, both absorption and scattering contribute to the extinction of a metal nanoparticle. The scattering component generating far-field radiation is believed to be the primary mechanism for enhanced fluorescence.[12] In theory, the fluorescence will be enhanced when the scattering of the nanoparticle dominates the plasmon resonance. It is known that the relative contributions of absorption and scattering are determined by the material and the size of the nanoparticles.[29] Among the numerous MEF studies, silver is preferred in the applications of MEF due to its greater scattering compared with gold. Yguerabide and Yguerabide observed that the scattering cross section of a 30 nm silver nanoparticle is 10 times larger than that of a gold nanoparticle of the same size.[21] The size dependent scattering has been demonstrated in Figure 2.7 where the scattering cross section increases and dominates the extinction as the size of the silver nanoparticle increases from 22 nm to 100 nm. To obtain the enhanced fluorescence, the predicted diameters for silver and gold nanospheres are over 40 and 80 nm, respectively.[29] Moreover, non-spherical or aggregated particles have been observed to enhance fluorescence which is primarily associated with large scattering components dominating over absorption.[63, 64]

In addition to the substantial scattering from the nanoparticle, the fluorescence of a nearby fluorophore is very sensitive to the spectral overlap between the scattering spectrum and the excitation and/or emission spectra of the fluorophore.[65, 66] Both theory and experiment have shown that the fluorescence enhancement can be optimized by appropriately matching the spectra of the nanoparticle and the fluorophore.[65-69]

Furthermore, the distance between the fluorophores and the metal nanoparticles plays a key role in the fluorescence enhancement.[70-73] Varying from system to system, MEF occurs when a fluorophore is placed within a distance of 3-50 nm from the surface of a metal nanoparticle,[74] and the maximum enhancement is typically achieved at a distance between 3-10 nm.[70, 72] When a fluorophore is directly coupled with a metal nanoparticle, its excited state can experience non-radiative decay through energy transfer from the fluorophore to the nanoparticle, leading to quenching.[60] When the fluorophore is separated from the nanoparticle by an appropriate distance between 3-10 nm, the non-radiative decay diminishes and the enhancement effect begins to dominate due to the increased excitation and emission rates. When the fluorophore-nanoparticle distance is larger than 10 nm, the enhancement effect reduces and eventually reaches unity.[75]

2.7 LSPR biosensing – current state-of-the-art

Nobel metal nanoparticles, especially gold and silver nanoparticles, have been extensively developed for biosensing such as the detection of molecular binding events on the basis of LSPR. In this section LSPR biosensing mainly for immunoassays in the biomedical area is discussed, based on different mechanisms including (i) refractive index sensitivity, (ii) colloidal aggregation, (iii) nanoparticle-enhanced SPR and (iv) MEF.

2.7.1 LSPR biosensing based on refractive index sensitivity

As discussed previously, the LSPR spectrum of noble metal nanoparticles is highly sensitive to changes in the dielectric environment. One approach to LSPR biosensing is the measurement of the LSPR spectral shift in response to the adsorption of analyte that results from a change in the local refractive index of the dielectric environment. The overall LSPR spectral shift is correlated with the analyte concentration, allowing for quantitative determination. To date, various LSPR biosensing systems have been designed using nanoparticles on solid phase surfaces and in liquid phase. Early work involved the use of gold and silver nanospheres immobilized on substrates. A biotin-streptavidin assay was used to investigate the refractive index sensitivities of immobilized gold nanospheres with a range of diameters.[76] The nanoparticles with optimal size exhibited a limit of detection (LOD) of 0.83 nM streptavidin. In assays

evaluating the antibody-antigen binding events with bovine or human serum albumin, an LOD of 10 nM was obtained using gold nanospheres.[77] Along with the development of synthetic methods for diverse nanoparticles, non-spherical nanoparticles have attracted substantial attention due to their highly enhanced local electronic fields near the sharp curvatures of the surfaces. Haes and Van Duyne first reported a highly sensitive LSPR biosensor using surface-confined triangular Ag nanoparticles supported on a glass substrate.[9] By functionalizing the triangular Ag nanoparticles with a specific antibody, they used this LSPR biosensing system to detect amyloid-β derived diffusible ligands (ADDLs), a biomarker for Alzheimer's disease, with an LOD of 100 fM.[9] The LSPR response of an individual gold nanorod sensor to exposure to prostate specific antigen (PSA) was measured by Truong *et al*. using a dark field microscope and a spectrograph.[78] The LOD of such individual sensors was estimated to be as low as ~ 1 aM, corresponding to an LSPR peak shift of ~ 4.2 nm.[78] Yu and Irudayaraj demonstrated a solution-phase multiplex assay based on gold nanorods for the detection of three analytes including goat anti-human IgG1 Fab, rabbit anti-mouse IgG1 Fab and rabbit anti-sheep IgG (H+L).[79] By combining three types of nanorods with distinct aspect ratios, different longitudinal LSPR peaks allowed for the simultaneous monitoring of three different analytes.[79] The group further extended this sensing system to the simultaneous detection of bacterial pathogens, *Escherichia coli* and *Salmonella typhimurium*, using a dispersion of gold nanorods with two distinct aspect ratios.[80]

2.7.2 LSPR biosensing based on colloidal aggregation

The LSPR phenomenon results in enhanced electronic fields being confined within a region of only a few nanometers near the surface of the nanoparticles and which decay exponentially away from the surface.[81] When multiple nanoparticles are placed in close vicinity of each other, the electronic fields of individual particles interact (i.e. near-field coupling) resulting in a redshift and a broadening of the LSPR wavelength.[82, 83] In 1980, Leuvering *et al.* first reported a new immunoassay approach based on the aggregation of antibody-conjugated gold nanoparticles in the presence of analyte, which was associated with a color change of the solution.[84] They further optimized the assay system for the detection of human chorionic gonadotrophin (hCG), a hormone produced during pregnancy.[85] A rapid homogeneous immunoassay for human ferritin was demonstrated by Englebienne *et al*. using gold colloids and the LOD was determined to be 4.5 μg/L.[86]

Thanh and Rosenzweig developed an aggregation-based immunoassay for anti-protein A using gold nanoparticles coated with protein A.[87] By adjusting the concentration of gold nanoparticles, pH and temperature, the aggregation immunoassay was optimized with an LOD of 1 µg/mL.[87] Currently, most of the aggregation-based immunoassays are developed using spherical gold nanoparticles, non-spherical nanoparticles however can also be employed in this approach.[88, 89] Hirsch *et al*. reported a rapid immunoassay based on the aggregation of antibody-conjugated gold nanoshells.[88] Successful detection of rabbit IgG was achieved in saline, serum and diluted whole blood with LODs on the order of 100 pg/mL within 10-30 min.[88] In contrast to the traditional spectroscopy measurement, dynamic light scattering (DLS) was used to analyze the aggregates of two types of gold nanoparticles for the detection of PSA.[89] In this approach, gold nanospheres and nanorods were conjugated with two different antibodies capable of binding to PSA. Following the addition of analyte, the relative ratio of aggregates to individual particles was quantified by DLS measurement, which was correlated with the concentration of the analyte.[89]

2.7.3 LSPR biosensing based on nanoparticle-enhanced SPR

Since the mid-1980s, the SPR sensing technique has been developed and well-established for detection and measurement of molecular interactions in real time. However, the conventional SPR sensing system has limited sensitivity to small molecules with low molecular weight such as hormones. To amplify the SPR signal and improve the sensitivity, noble metal nanoparticles have been incorporated with success in SPR sensors.[90-94] The utilization of nanoparticles leads to enhanced SPR sensitivity through three main mechanisms: (i) an increase of the mass in every binding event, (ii) an increase in the refractive index of the analyte and (iii) coupling between the LSPR of nanoparticles and the SPR of the metal surface.[95] Several groups have reported enhanced SPR signals due to gold nanospheres used in a sandwich assay format where the secondary antibody was conjugated with the nanoparticles.[90, 93, 94] By using antibody-nanoparticle conjugates in a sandwich assay for detection of human matrix metalloproteinase (MMP)-2, an enhancement factor of 114 and an LOD of 0.5 pM was observed.[93] In another sandwich assay for progesterone detection the antibody-conjugated gold nanospheres resulted in an enhancement factor of 13 and an LOD of 8.6 pg/mL.[94] In addition to the spherical nanoparticles, various shapes of nanoparticles

have been studied for the enhancement of SPR.[95-97] Law *et al.* reported a 23-fold enhancement in the sensitivity of SPR detection for rabbit IgG using antibody-conjugated gold nanorods, with an LOD of ~ 40 pg/mL.[95] In a recent study, three different shapes of gold nanoparticles including cubic cages, rods and quasi-spheres have been compared in terms of sensitivity enhancement of SPR detection for thrombin.[97] The greatest enhancement was observed for quasi-spherical nanoparticles which resulted in the detection of thrombin concentrations as low as ~ 1 aM.

2.7.4 LSPR biosensing based on MEF

Fluorescence spectroscopy is one of the predominant tools used for biomedical research. Significant advances are being made in fluorescence techniques, which improve the sensitivity and LOD of biosensing systems. Over the last decade, noble metal nanoparticles have been incorporated into fluorescence-based assays, resulting in immunoassays with amplified fluorescence signals and increased sensitivities.[98-101] The increased fluorescence intensity and improved performance of these assays is attributed to the phenomenon of MEF. MEF can arise from both enhanced excitation and emission processes. Nanoscale metals can interact with fluorophores through the presence of their local electromagnetic fields and through coupling of their plasmonic scattering modes to increase their fluorescence intensity.[29, 102, 103] Herein, Table 2.1 summarizes the findings of selected reports from the recent literature in relation to the fluorescence-based assays enhanced by metal nanoparticles.

Table 2.1 Characteristics of MEF assays in the literature.

Nanostructure	Fluorophore & analyte	Enhancement factor	LOD	Reference
Silver nanosphere film (35 nm)	6-(N-(7-nitrobenz-2-oxa-1,3-diazol-4yl) amino) hexanoate (NBD), goat IgG	20	N/A	Sokolov *et al.* (1998)[104]
Silver nanosphere film	Fluorescein, rabbit IgG	N/A	500 pM	Lobmaier *et al.* (2001) [105]
Silver nanosphere film	Fluorescein, insulin	4	250 nM	Lochner *et al.* (2003)[106]
Silver nanospheres in solution	Cy3, streptavidin	3-5	N/A	Aslan *et al.* (2004)[107]
Silver island films (SIF)	Rhodamine Red-X and Alexa Fluor-647, myoglobin	10-15 for 100 ng/mL myoglobin	50 ng/mL	Matveeva *et al.* (2005)[98]
Gold nanosphere film (5 nm)	Cy5, human B-type natriuretic peptide (BNP) and cardiac troponin I (cTnI)	2.5 for BNP and 4 for cTnI	N/A	Hong and Kang (2006)[108]
SIF on gold/silver film	Rhodamine-RedX, myoglobin	50 for 1000 ng/mL myoglobin	N/A	Barnett *et al.* (2007)[100]
Gold nanospheres (20 nm)	Cy 5, mouse IgG	N/A	1 pg/mL	Hsieh *et al.* (2007)[109]
SIF on gold film	AlexaFluor 647, myoglobin	50 for 100 ng/mL myoglobin	N/A	Matveeva *et al.* (2007)[110]
Cap-shaped silver nanoparticles	R-phycoerythrin, IL-6	50	N/A	Yamaguchi *et al.* (2007)[111]
Silver nanosphere film	Cy 5, human IgG	11 - 37	0.086 ng/mL	Nooney *et al.* (2010)[99]
SIF	DY 488, human TNF-α	10.4	50 pg/mL	Szmacinski *et al.* (2010)[101]
Silver-coated silica beads on substrate	AlexaFluor 430, rabbit IgG	8.5	N/A	Deng *et al.* (2010)[112]
SIF	FITC, anthrax protective antigen	20 – 30	0.1 pg/mL	Dragan *et al.* (2010)[113]
Silver nanospheres	Cy 5, human IgG	N/A	1 ng/mL	Wei *et al.* (2012)[114]
Silver bilayer nanosphere film	FITC, human IgG	3.3	1 ng/mL	Zhang *et al.* (2012)[115]
Gold nanospheres	Atto 633, UL-16 binding protein 2	N/A	16-18 pg/mL	Chang *et al.* (2013)[116]

2.8 Conclusions

In conclusion, this chapter has attempted to describe the principal elements of the work described in this thesis. A description of immunoassays has been given, distinguishing between homogeneous and heterogeneous assays, label-free and labeled assays, and direct and sandwich assays. The interaction of electromagnetic radiation with noble metal nanoparticles and the role of the surface plasmon has been described and the theory and has been outlined. As background to the work carried out in this thesis, four different approaches to LSPR biosensing have been described and key recent publications in these areas have been highlighted. Of the four approaches discussed, the first two, namely refractive index sensitivity-based and aggregation-based assays, were primarily carried out in solution-phase as reported in Chapters 4 and 5. Chapter 5 also includes a section on solid-phase SPR biosensing while Chapter 6 describes MEF-based immunoassays carried out on a solid-phase platform.

References

1. A. D. MacNaught and A. R. Wilkinson, *IUPAC Compendium of Chemical Terminology Gold Book*. (Blackwell Science, 1997).
2. N. S. Lipman, L. R. Jackson, L. J. Trudel and F. Weis-Garcia, ILAR journal **46** (3), 258-267 (2005).
3. R. Reverberi and L. Reverberi, Blood Transfusion **5** (4), 227-240 (2007).
4. http://www.austincc.edu/apreview/EmphasisItems/Inflammatoryresponse.html.
5. D. Wild, *The immunoassay handbook*. 15-50 (Elsevier Science & Technology Books, 2005).
6. G. Wu, *Assay Development: Fundamentals and Practices*. (Wiley, 2010).
7. N. Bojorge Ramírez, A. M. Salgado and B. Valdman, Brazilian Journal of Chemical Engineering **26**, 227-249 (2009).
8. W. M. Mullett, E. P. C. Lai and J. M. Yeung, Methods **22** (1), 77-91 (2000).
9. A. J. Haes, L. Chang, W. L. Klein and R. P. Van Duyne, Journal of the American Chemical Society **127** (7), 2264-2271 (2005).
10. K. M. Mayer, S. Lee, H. Liao, B. C. Rostro, A. Fuentes, P. T. Scully, C. L. Nehl and J. H. Hafner, ACS Nano **2** (4), 687-692 (2008).
11. J. Cao, E. K. Galbraith, T. Sun and K. T. V. Grattan, Sensors and Actuators B: Chemical **169** (0), 360-367 (2012).
12. J. R. Lakowicz, *Principles of fluorescence spectroscopy*. (Springer, 2006).
13. S. J. Strickler and R. A. Berg, The Journal of Chemical Physics **37** (4), 814-822 (1962).
14. J. M. Brockman, B. P. Nelson and R. M. Corn, Annual Review of Physical Chemistry **51** (1), 41-63 (2000).
15. R. P. Van Duyne, Science **306** (5698), 985-986 (2004).
16. K. A. Willets and R. P. Van Duyne, Annual Review of Physical Chemistry **58** (1), 267-297 (2007).
17. S. Eustis and M. A. El-Sayed, ChemInform **37** (25) (2006).
18. G. Mie, Annalen der Physik **330** (3), 377-445 (1908).
19. Uwe Kreibig and M. Vollmer, *Optical properties of metal clusters* (Springer, Berlin, 1995).
20. S. Link, Z. L. Wang and M. A. El-Sayed, The Journal of Physical Chemistry B **103** (18), 3529-3533 (1999).

21. J. Yguerabide and E. E. Yguerabide, Analytical Biochemistry **262** (2), 137-156 (1998).
22. C. F. Bohren and D. R. Huffman, *Absorption and scattering of light by small particles*. (Wiley, 1983).
23. U. Kreibig and M. Vollmer, *Optical Properties of Metal Clusters*. (Springer, 1995).
24. C. Noguez, The Journal of Physical Chemistry C **111** (10), 3806-3819 (2007).
25. A. S. Kumbhar, M. K. Kinnan and G. Chumanov, Journal of the American Chemical Society **127** (36), 12444-12445 (2005).
26. K. L. Shuford, M. A. Ratner and G. C. Schatz, The Journal of Chemical Physics **123** (11), 114713 (2005).
27. N. Felidj, J. Grand, G. Laurent, J. Aubard, G. Levi, A. Hohenau, N. Galler, F. R. Aussenegg and J. R. Krenn, The Journal of Chemical Physics **128** (9), 094702-094705 (2008).
28. M. Meier and A. Wokaun, Opt. Lett. **8** (11), 581-583 (1983).
29. J. R. Lakowicz, Analytical Biochemistry **337** (2), 171-194 (2005).
30. R. Gans, Annalen der Physik **342** (5), 881-900 (1912).
31. W.-H. Yang, G. C. Schatz and R. P. Van Duyne, Journal of Chemical Physics **103** (3), 869 (1995).
32. K. L. Kelly, A. A. Lazarides and G. C. Schatz, Computing in Science & Engineering **3** (4), 67-73 (2001).
33. N. Riefler and T. Wriedt, Progress In Electromagnetics Research Symposium **2** (5), 450-454 (2006).
34. E. Moreno, D. Erni, C. Hafner and R. Vahldieck, J. Opt. Soc. Am. A **19** (1), 101-111 (2002).
35. R. X. Bian, R. C. Dunn, X. S. Xie and P. T. Leung, Physical Review Letters **75** (26), 4772 (1995).
36. K. L. Kelly, E. Coronado, L. L. Zhao and G. C. Schatz, The Journal of Physical Chemistry B **107** (3), 668-677 (2003).
37. B. J. Wiley, S. H. Im, Z.-Y. Li, J. McLellan, A. Siekkinen and Y. Xia, The Journal of Physical Chemistry B **110** (32), 15666-15675 (2006).
38. J. Kottmann, ouml, P. rg, O. J. F. Martin, D. R. Smith and S. Schultz, Physical Review B **64** (23), 235402 (2001).

39. J. P. Kottmann, O. J. F. Martin, D. R. Smith and S. Schultz, Physical Review B **64** (23), 235402 (2001).
40. J. Aizpurua, G. W. Bryant, L. J. Richter, F. J. García de Abajo, B. K. Kelley and T. Mallouk, Physical Review B **71** (23), 235420 (2005).
41. A. J. Haes, C. L. Haynes, A. D. McFarland, G. C. Schatz, R. P. Van Duyne and S. Zou, MRS Bulletin **30** (05), 368-375 (2005).
42. E. Hao and G. C. Schatz, *Electromagnetic fields around silver nanoparticles and dimers*. (AIP, 2004).
43. F. Guedje, K. , M. Giloan, M. Potara, M. N. Hounkonnou and S. Astilean, Physica Scripta **86** (5), 055702 (2012).
44. R. Jin, Y. Cao, C. A. Mirkin, K. L. Kelly, G. C. Schatz and J. G. Zheng, Science **294** (5548), 1901-1903 (2001).
45. F. Tam, C. Moran and N. Halas, The Journal of Physical Chemistry B **108** (45), 17290-17294 (2004).
46. T. R. Jensen, M. L. Duval, K. L. Kelly, A. A. Lazarides, G. C. Schatz and R. P. Van Duyne, The Journal of Physical Chemistry B **103** (45), 9846-9853 (1999).
47. A. D. McFarland and R. P. Van Duyne, Nano Letters **3** (8), 1057-1062 (2003).
48. A. J. Haes, S. Zou, G. C. Schatz and R. P. Van Duyne, The Journal of Physical Chemistry B **108** (22), 6961-6968 (2004).
49. M. D. Malinsky, K. L. Kelly, G. C. Schatz and R. P. Van Duyne, Journal of the American Chemical Society **123** (7), 1471-1482 (2001).
50. M. M. Miller and A. A. Lazarides, The Journal of Physical Chemistry B **109** (46), 21556-21565 (2005).
51. H. Chen, X. Kou, Z. Yang, W. Ni and J. Wang, Langmuir **24** (10), 5233-5237 (2008).
52. P. Kvasnicka and J. Homola, *Optical sensors based on spectroscopy of localized surface plasmons on metallic nanoparticles: Sensitivity considerations*. (AVS, 2008).
53. C. Xue, Z. Li and Chad A. Mirkin, Small **1** (5), 513-516 (2005).
54. D. E. Charles, D. Aherne, M. Gara, D. M. Ledwith, Y. K. Gun'ko, J. M. Kelly, W. J. Blau and M. E. Brennan-Fournet, ACS Nano **4** (1), 55-64 (2009).
55. K.-S. Lee and M. A. El-Sayed, The Journal of Physical Chemistry B **110** (39), 19220-19225 (2006).

56. P. K. Jain and M. A. El-Sayed, The Journal of Physical Chemistry C **111** (47), 17451-17454 (2007).
57. Y. Zhang, A. Dragan and C. D. Geddes, The Journal of Physical Chemistry C **113** (28), 12095-12100 (2009).
58. K. Ray, M. H. Chowdhury, J. Zhang, Y. Fu, H. Szmacinski, K. Nowaczyk and J. R. Lakowicz, in *Optical Sensor Systems in Biotechnology*, edited by G. Rao (Springer Berlin Heidelberg, 2010), Vol. 116, pp. 1-28.
59. J. R. Lakowicz, K. Ray, M. Chowdhury, H. Szmacinski, Y. Fu, J. Zhang and K. Nowaczyk, Analyst **133** (10), 1308-1346 (2008).
60. T. Ming, H. Chen, R. Jiang, Q. Li and J. Wang, The Journal of Physical Chemistry Letters **3** (2), 191-202 (2011).
61. M. H. Chowdhury, S. K. Gray, J. Pond, C. D. Geddes, K. Aslan and J. R. Lakowicz, J. Opt. Soc. Am. B **24** (9), 2259-2267 (2007).
62. T. Härtling, P. Reichenbach and L. M. Eng, Opt. Express **15** (20), 12806-12817 (2007).
63. K. Aslan, J. R. Lakowicz and C. D. Geddes, The Journal of Physical Chemistry B **109** (13), 6247-6251 (2005).
64. H. Su, Y. Zhong, T. Ming, J. Wang and K. S. Wong, The Journal of Physical Chemistry C **116** (16), 9259-9264 (2012).
65. Y. Chen, K. Munechika and D. S. Ginger, Nano Letters **7** (3), 690-696 (2007).
66. S. Vukovic, S. Corni and B. Mennucci, The Journal of Physical Chemistry C **113** (1), 121-133 (2009).
67. M. Thomas, J. J. Greffet, R. Carminati and J. R. Arias-Gonzalez, Applied Physics Letters **85** (17), 3863-3865 (2004).
68. P. Bharadwaj and L. Novotny, Opt. Express **15** (21), 14266-14274 (2007).
69. F. Tam, G. P. Goodrich, B. R. Johnson and N. J. Halas, Nano Letters **7** (2), 496-501 (2007).
70. J. Malicka, I. Gryczynski, Z. Gryczynski and J. R. Lakowicz, Analytical Biochemistry **315** (1), 57-66 (2003).
71. K. Ray, R. Badugu and J. R. Lakowicz, Chemistry of Materials **19** (24), 5902-5909 (2007).
72. R. I. Nooney, O. Stranik, C. McDonagh and B. D. MacCraith, Langmuir **24** (19), 11261-11267 (2008).

73. K. Kang, J. Wang, J. Jasinski and S. Achilefu, Journal of Nanobiotechnology **9** (1), 16 (2011).
74. H. Szmacinski, D. S. Smith, M. A. Hanson, Y. Kostov, J. R. Lakowicz and G. Rao, Biotechnology and Bioengineering **100** (3), 448-457 (2008).
75. W. Deng and E. M. Goldys, Langmuir **28** (27), 10152-10163 (2012).
76. N. Nath and A. Chilkoti, Analytical Chemistry **76** (18), 5370-5378 (2004).
77. K. Fujiwara, H. Watarai, H. Itoh, E. Nakahama and N. Ogawa, Anal Bioanal Chem **386** (3), 639-644 (2006).
78. P. L. Truong, B. W. Kim and S. J. Sim, Lab on a Chip **12** (6), 1102-1109 (2012).
79. C. Yu and J. Irudayaraj, Analytical Chemistry **79** (2), 572-579 (2007).
80. C. Wang and J. Irudayaraj, Small **4** (12), 2204-2208 (2008).
81. T. Jensen, L. Kelly, A. Lazarides and G. C. Schatz, Journal of Cluster Science **10** (2), 295-317 (1999).
82. K. H. Su, Q. H. Wei, X. Zhang, J. J. Mock, D. R. Smith and S. Schultz, Nano Letters **3** (8), 1087-1090 (2003).
83. L. Gunnarsson, T. Rindzevicius, J. Prikulis, B. Kasemo, M. Käll, S. Zou and G. C. Schatz, The Journal of Physical Chemistry B **109** (3), 1079-1087 (2005).
84. J. H. W. Leuvering, P. J. H. M. Thal, M. van der Waart and A. H. W. M. Schuurs, Journal of Immunoassay **1** (1), 77 - 91 (1980).
85. J. H. W. Leuvering, P. J. H. M. Thal and A. H. W. M. Schuurs, Journal of Immunological Methods **62** (2), 175-184 (1983).
86. P. Englebienne, A. Van Hoonacker and J. Valsamis, Clinical Chemistry **46** (12), 2000-2003 (2000).
87. N. T. K. Thanh and Z. Rosenzweig, Analytical Chemistry **74** (7), 1624-1628 (2002).
88. L. R. Hirsch, J. B. Jackson, A. Lee, N. J. Halas and J. L. West, Analytical Chemistry **75** (10), 2377-2381 (2003).
89. X. Liu, Q. Dai, L. Austin, J. Coutts, G. Knowles, J. Zou, H. Chen and Q. Huo, Journal of the American Chemical Society **130** (9), 2780-2782 (2008).
90. L. A. Lyon, M. D. Musick and M. J. Natan, Analytical Chemistry **70** (24), 5177-5183 (1998).
91. B. H. Schneider, E. L. Dickinson, M. D. Vach, J. V. Hoijer and L. V. Howard, Biosensors and Bioelectronics **15** (1–2), 13-22 (2000).

92. B. H. Schneider, E. L. Dickinson, M. D. Vach, J. V. Hoijer and L. V. Howard, Biosensors and Bioelectronics **15** (11–12), 597-604 (2000).
93. U. Pieper-Fürst, U. Kleuser, W. F. M. Stöcklein, A. Warsinke and F. W. Scheller, Analytical Biochemistry **332** (1), 160-167 (2004).
94. J. S. Mitchell, Y. Wu, C. J. Cook and L. Main, Analytical Biochemistry **343** (1), 125-135 (2005).
95. W.-C. Law, K.-T. Yong, A. Baev, R. Hu and P. N. Prasad, Opt. Express **17** (21), 19041-19046 (2009).
96. H. R. Sim, A. W. Wark and H. J. Lee, Analyst **135** (10), 2528-2532 (2010).
97. M. J. Kwon, J. Lee, A. W. Wark and H. J. Lee, Analytical Chemistry **84** (3), 1702-1707 (2012).
98. E. G. Matveeva, Z. Gryczynski and J. R. Lakowicz, Journal of Immunological Methods **302** (1–2), 26-35 (2005).
99. R. Nooney, A. Clifford, X. LeGuevel, O. Stranik, C. McDonagh and B. MacCraith, Anal Bioanal Chem **396** (3), 1127-1134 (2010).
100. A. Barnett, E. G. Matveeva, I. Gryczynski, Z. Gryczynski and E. M. Goldys, Physica B: Condensed Matter **394** (2), 297-300 (2007).
101. H. Szmacinski, Z. Murtaza and J. R. Lakowicz, The Journal of Physical Chemistry C **114** (16), 7236-7241 (2010).
102. J. R. Lakowicz, Analytical Biochemistry **298** (1), 1-24 (2001).
103. Y. Zhang, K. Aslan, M. J. R. Previte and C. D. Geddes, Applied Physics Letters **90** (5), 053107/053101-053107/053103 (2007).
104. K. Sokolov, G. Chumanov and T. M. Cotton, Analytical Chemistry **70** (18), 3898-3905 (1998).
105. C. Lobmaier, G. Hawa, M. Götzinger, M. Wirth, F. Pittner and F. Gabor, Journal of Molecular Recognition **14** (4), 215-222 (2001).
106. N. Lochner, C. Lobmaier, M. Wirth, A. Leitner, F. Pittner and F. Gabor, European Journal of Pharmaceutics and Biopharmaceutics **56** (3), 469-477 (2003).
107. K. Aslan, J. Lakowicz, H. Szmacinski and C. Geddes, J Fluoresc **14** (6), 677-679 (2004).
108. B. Hong and K. A. Kang, Biosensors and Bioelectronics **21** (7), 1333-1338 (2006).

109. B.-Y. Hsieh, Y.-F. Chang, M.-Y. Ng, W.-C. Liu, C.-H. Lin, H.-T. Wu and C. Chou, Analytical Chemistry **79** (9), 3487-3493 (2007).

110. E. G. Matveeva, I. Gryczynski, A. Barnett, Z. Leonenko, J. R. Lakowicz and Z. Gryczynski, Analytical Biochemistry **363** (2), 239-245 (2007).

111. T. Yamaguchi, T. Kaya and H. Takei, Analytical Biochemistry **364** (2), 171-179 (2007).

112. W. Deng, K. Drozdowicz-Tomsia, D. Jin and E. M. Goldys, presented at the Nanoscience and Nanotechnology (ICONN), 2010 International Conference on, 2010 (unpublished).

113. A. I. Dragan, M. T. Albrecht, R. Pavlovic, A. M. Keane-Myers and C. D. Geddes, Analytical Biochemistry **425** (1), 54-61 (2012).

114. X. Wei, H. Li, Z. Li, M. Vuki, Y. Fan, W. Zhong and D. Xu, Anal Bioanal Chem **402** (3), 1057-1063 (2012).

115. R. Zhang, Z. Wang, C. Song, J. Yang, A. Sadaf and Y. Cui, J Fluoresc **23** (1), 71-77 (2012).

116. Y.-F. Chang, J.-S. Yu, Y.-T. Chang, L.-C. Su, C.-C. Wu, Y.-S. Chang, C.-S. Lai and C. Chou, Biosensors and Bioelectronics **41** (0), 232-237 (2013).

Chapter 3

Instrumentation

3.1 Introduction

This chapter presents the theory behind the instrumentation and characterization techniques used for data collection within this thesis. The characterization techniques include ultraviolet-visible (UV-vis) spectroscopy, transmission electron microscopy (TEM), dynamic light scattering (DLS), surface plasmon resonance (SPR) spectroscopy, atomic force microscopy (AFM) and fluorescence spectroscopy. The background of each technique is given in the following sections.

3.2 Ultraviolet-visible spectroscopy

UV-vis spectroscopy is a broadly used tool for the characterization of noble metal nanoparticles as the optical properties of nanoparticles are sensitive to the size, shape and the concentration of the nanoparticles as well as the dielectric environment surrounding them. Noble metal nanoparticles will not only absorb light but also scatter it therefore meaning that the detected signal from the sample is representative of their extinction spectra, i.e. the sum of their absorption and scattering.

UV-vis spectroscopy is based on absorbance. In spectroscopy, the absorbance A is defined as,[1]

$$A = \log_{10} \frac{I_0}{I} \tag{3.1}$$

where I_0 is the intensity of the incident light at a given wavelength, I is the intensity of the light after it passes through a sample (transmitted light intensity). To quantitatively determine the concentration of a sample, Beer-Lambert law is commonly used,[1]

$$\log_{10} \frac{I_0}{I} = \epsilon c l \tag{3.2}$$

where ϵ is the molar extinction coefficient, c is the concentration of the absorbing sample and l is the path length through the sample. The schematic illustration of Beer-Lambert law is given in Figure 3.1. According to equations 3.1 and 3.2, the Beer-Lambert law implies a linear relationship between the absorbance and the concentration of an absorbing sample under constant conditions of the path length and the incident wavelength of the light. In this thesis the spectrophotometers used for characterization of UV-vis spectra include Ocean Optics USB4000, Varian Cary 50 and Tecan Infinite 200.

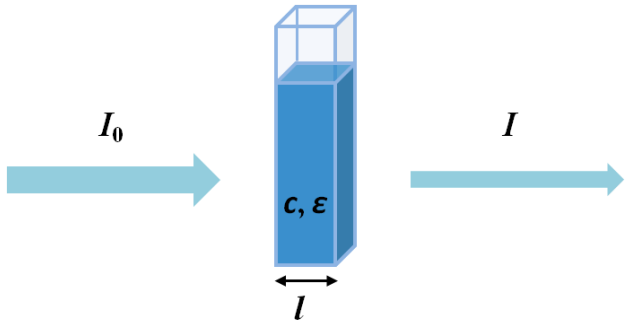

Figure 3.1 Schematic diagram illustrating Beer-Lambert law.

3.3 Transmission electron microscopy

TEM is a microscopy technique that images thin samples at a high resolution using a beam of electrons. It provides an approach to characterizing the morphology, dimensions and distribution of the nanoparticles. A simplified TEM setup is shown in Figure 3.2, depicting the major constituents in the vacuum system.[2] The emission source which is otherwise known as the electron gun emits the electrons that travel down a column and are focused by the condenser lens into a very thin beam. The beam of electrons illuminates the specimen on the specimen holder. Depending on the density of the material present, some of the electrons are scattered and disappear from the beam. The transmitted electrons are focused into an image by the objective lens, followed by traveling through the projective lens to magnify the image. The image is detected by a phosphor screen or a charge coupled device (CCD).[2] Contrast observed in the image is mostly attributed to differences in density. In this thesis the TEM used for characterizing the nanoparticles is an FEI Tecnai G^2 20. All TEM experiments were carried out in University College Dublin (UCD).

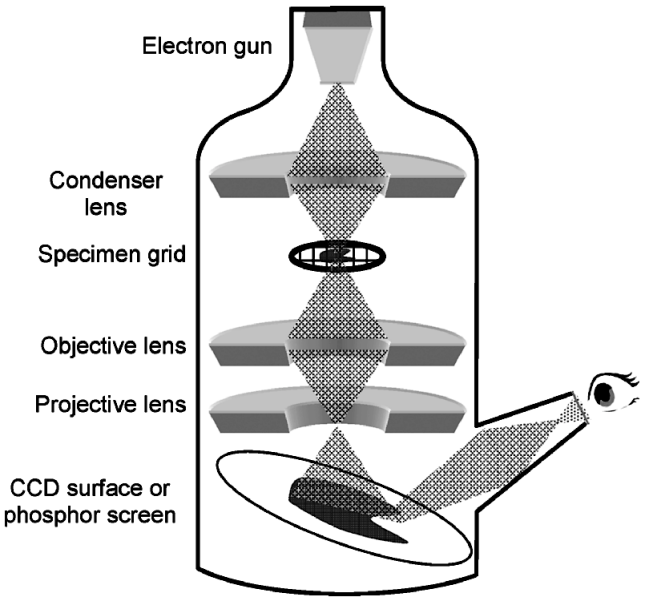

Figure. 3.2 Schematic diagram of a simplified TEM system. Adapted from reference.[2]

3.4 Dynamic light scattering

DLS, also referred to as Photon Correlation Spectroscopy (PCS), is a technique that measures the size of particles suspended in liquids. Particles in suspensions undergo Brownian motion due to random collisions with the solvent molecules surrounding them. As a result of Brownian motion, particles diffuse through the solvent. The DLS system measures Brownian motion and relates it to the size of the particles by illuminating the particles with a laser beam and analyzing the time-dependent fluctuations in the intensity of scattered light from particles. The translational diffusion coefficient is determined by the analysis of intensity fluctuation using the autocorrelation function. The size of a particle is then calculated from the translational diffusion coefficient according to the Stokes-Einstein equation,[3]

$$d_H = \frac{kT}{3\pi\eta D} \tag{3.3}$$

where d_H is the hydrodynamic diameter of the particle, k is the Boltzmann's constant, T is the absolute temperature, η is the viscosity of the solvent and D is the translational diffusion coefficient. The hydrodynamic diameter is the diameter of a sphere with the same diffusion coefficient as that of the measured particle in the suspension. It is apparent that small particles move quickly while larger particles move more slowly. In this thesis all DLS measurements were carried out with a Delsa Nano C.

3.5 Surface plasmon resonance spectroscopy

SPR spectroscopy is widely used for detection of molecular interactions in real time by measuring a change in the SPR of a planar metal (typically gold and silver) surface as a result of a change in the refractive index near the surface. Figure 3.3 illustrates a typical SPR-based detection of molecular binding events. Under specific conditions (i.e. angle of incidence and wavelength), the incident p-polarized light excites plasmons in the gold film. As a result, a characteristic absorption of energy occurs and SPR is detected as a reduction in the intensity of the reflected light. The angle of incidence for SPR is highly sensitive to changes in the refractive index at the metal-dielectric interface.[4] Therefore, binding of an antigen (yellow circles) to the immobilized antibody (red 'Y' shapes) is detected as a shift in the angle of incidence required for SPR. Additionally, a plot of angle of incidence against time directly corresponds to magnitude and kinetics of antigen-antibody binding in real time. In this thesis, the SPR experiments were performed with a Biacore 3000.

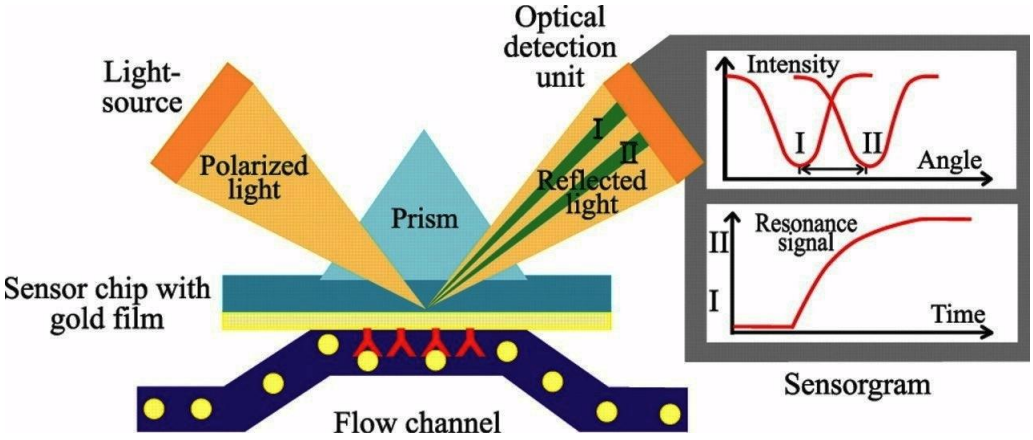

Figure 3.3 Schematic diagram illustrating SPR detection for antigen-antibody binding. Reproduced from Biacore.[5]

The Biacore 3000 system is composed of three main components, including the SPR detection system, the sensor surface and the microfluidic system. The SPR detection system is described above. The sensor chip provides the physical conditions to generate the SPR signal. Gold surfaces with or without modification are used for the sensor chips. The biomolecular interactions being studied occur on the surface of the sensor chip. The microfluidic system is responsible for the precise delivery of sample and

buffer in a controlled fashion. The sensor surface forms one wall of a flow cell which is an integral part of the microfluidic system. A continuous flow of liquid is maintained over the sensor surface throughout the analysis, switching between buffer and sample.

3.6 Atomic force microscopy

AFM is a type of scanning probe microscopy that resolves features at the nanometer scale for either conductive or non-conductive samples. As shown in Figure 3.4, a typical AFM system consists of a cantilever with a sharp tip at its free end and a laser beam deflection system. By bringing the tip into the vicinity of a sample surface, forces acting between the tip and the sample surface cause the cantilever to bend. A laser spot is reflected from the back of the cantilever onto a position-sensitive photodetector. When the tip scans across the surface, the cantilever bends to accommodate changes in topography, resulting in changes in the position of the laser spot. The forces generally measured include Van der Waals, electrostatic, magnetic, capillary, Casimir and solvation forces. They are not measured directly but calculated by measuring the deflection of the cantilever.

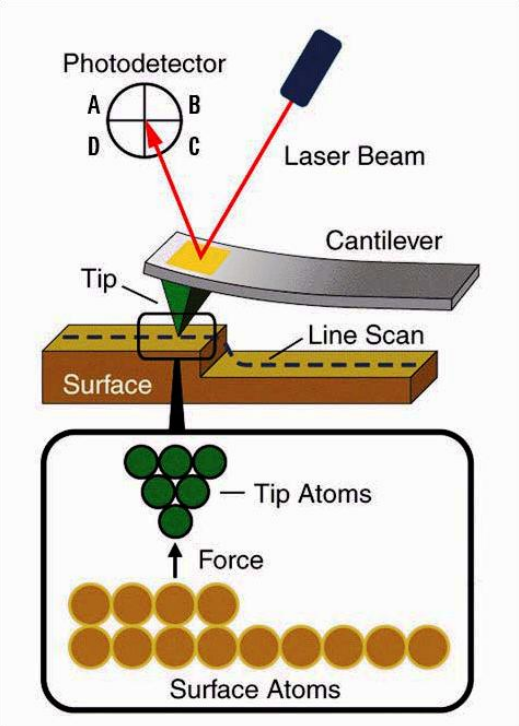

Figure 3.4 Schematic diagram illustrating a typical AFM set-up. Reproduced from Agilent.[6]

The primary modes of AFM operation include contact mode, non-contact mode and tapping mode. Contact mode is performed with the tip in gentle contact with the surface of a sample. In this mode, the tip either scans at a constant height above the surface or scans with a constant force by keeping a constant deflection. In contrast to contact mode, non-contact mode is performed with the tip oscillated near the surface of a sample. The distance between the tip and the surface is on the order of tens to hundreds of Angstroms. In this mode, the cantilever is oscillated near its resonance frequency with an amplitude less than 10 nm. The detection scheme is based on analyzing changes in the resonance frequency or oscillation amplitude of the cantilever. Tapping mode is an approach that maps topography by intermittently contacting the surface with an oscillating tip. In this mode, the cantilever is driven to oscillate up and down at or near its resonance frequency with an amplitude greater than 10 nm. When the tip comes close to the surface, the oscillation amplitude reduces due to the forces acting between the tip and the sample. A feedback system monitors the changes in the amplitude and ensures that the amplitude is maintained constant during a scan. A topography image is obtained by monitoring the force required to keep the oscillation amplitude constant. The choice of operation modes depends on the sample and its environment. Tapping mode is usually used for imaging nanoparticles that are loosely bound to the substrate as it eliminates the lateral force applied by the tip that may damage the sample, which is common in contact mode.[7] Compared with non-contact mode, tapping mode provides higher resolution. In this thesis, the AFM experiments were carried out in tapping mode using a Veeco BioScope II.

3.7 Fluorescence spectroscopy

Fluorescence spectroscopy is a tool that analyzes fluorescence from a sample. The detailed description of the absorption and fluorescence process of a fluorophore has been given in section 2.3. The instrument for measuring fluorescence is known as a spectrofluorometer or fluorescence spectrometer. A schematic representation of a typical spectrofluorometer is illustrated in Figure 3.5. The light source such as xenon lamp emits light over a broad spectrum typically ranging from 200 to 900 nm. The light passes through a monochromator that selects the desired narrow band of wavelengths. The transmitted light strikes the sample, causing fluorescence emission by fluorophores within the sample. The fluorescence is dispersed by a second monochromator and

collected by a detector which is usually a photomultiplier tube (PMT). The signal is amplified and finally presented in graphical form and stored digitally. In this thesis, all fluorescence measurements were performed with a Tecan Infinite 200 plate reader.

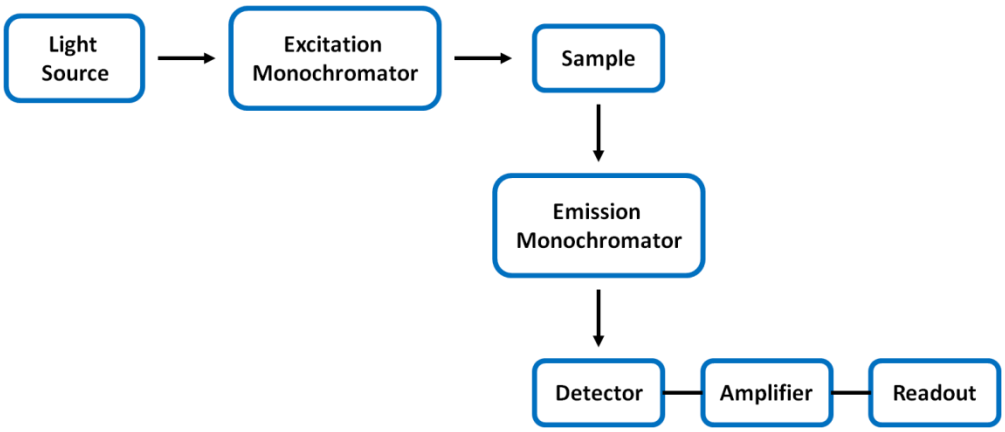

Figure 3.5 Block diagram of a typical spectrofluorometer.

References

1. A. L. Lehninger, D. D. L. Nelson and M. M. Cox, *Lehninger Principles of Biochemistry*. (W.H. Freeman, 2005).
2. K. Kalantar-Zadeh and B. N. Fry, *Nanotechnology-Enabled Sensors*. (Springer London, Limited, 2008).
3. A. Einstein, Annalen der Physik **322** (8), 549-560 (1905).
4. Z. Salamon, M. F. Brown and G. Tollin, Trends in Biochemical Sciences **24** (6), 213-219 (1999).
5. www.Biacore.com.
6. www.home.agilent.com.
7. T. Junno, S. Anand, K. Deppert, L. Montelius and L. Samuelson, Applied Physics Letters **66** (24), 3295-3297 (1995).

Chapter 4

Triangular nanoplates for direct assays in solution

4.1 Introduction

As outlined in Chapter 1, this thesis work is in two sections, the earlier part, which was carried out in NUI Galway and which uses the Kelly particles for solution-based assays, and work carried out in BDI on both solution and solid-phase assays using various types of metal nanoparticles. This chapter focuses on the Galway work on solution-phase assays using the Kelly particles. The work here involves the utilization of solution-phase triangular silver nanoplates (TSNPs) and their derivatives, gold-coated TSNPs (AuTSNPs), as LSPR refractive index sensors for biomedical assays. The size of the TSNPs can be readily controlled resulting in plasmon bands throughout the visible spectrum and the near infrared by using a seed-mediated synthetic procedure in aqueous solution (Figure 4.1).[1] A comprehensive study has been carried out by Charles *et al.*, demonstrating that these TSNP sols exhibit high ensemble refractive index sensitivities and can potentially act as efficient optical sensors for biomedical assays.[2] The AuTSNP sols are synthesized in a straightforward fashion through epitaxial deposition of a gold layer at the edges of TSNPs. This effectively protects the TSNPs against etching by chloride and other anions.[3] These AuTSNP sols are also found to exhibit high refractive index sensitivities and thus are promising candidates for biomedical sensing.

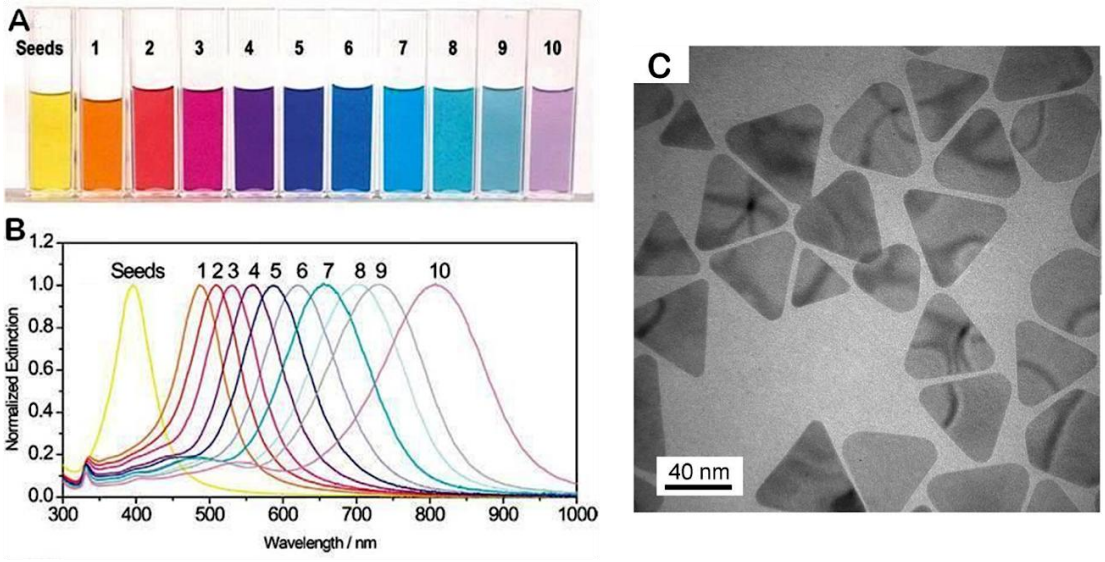

Figure 4.1 (A) Photograph of TSNP sols with a range of colors indicating various sizes; (B) The corresponding extinction spectra of the TSNP sols in image (A); and (C) TEM image of flat-lying TSNP from a representative sample. Adapted from reference.[1]

4.2 Overview of the assays

The LSPR-based biomedical assays in this work include two preliminary models, the first for the detection of human C-reactive protein (CRP) and the second for human cardiac troponin I (cTnI). Both assays are designed as one-step, solution-phase platforms for simple, highly sensitive and high-throughput biomedical sensing.

As stated previously, the LSPR of the nanoplates are sensitive to the changes of local refractive index. The LSPR peak shifts as the local refractive index is changed. The utilization of the solution-phase triangular nanoplates in this study is directly based on this concept. In general, the triangular nanoplates are functionalized with a suitable biological receptor and then used to detect the target analyte which specifically binds to that receptor on the surface of the nanoplate. Consequently, the receptor-nanoplate conjugates experience a redshift in the LSPR peak when the analyte-receptor binding occurs inducing an increase in the refractive index of the nanoplates' surrounding medium (Figure 4.2). This redshift can be detected by standard UV-vis spectroscopy using a conventional spectrophotometer and be used to quantify the concentration of the analyte.

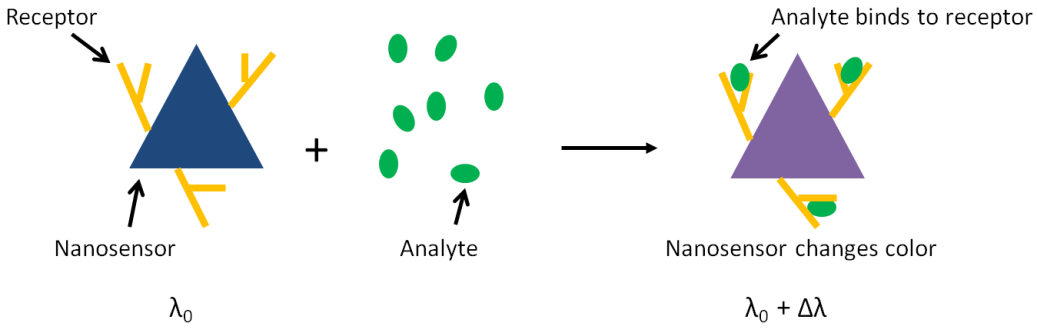

Figure 4.2 Schematic illustrating a receptor functionalized triangular nanoplate sensing the analyte binding to its surface which is characterized by the absorption color changing from blue to purple.

In this study, two preliminary model assays have been developed based on the aforementioned theory using solution-phase triangular nanoplates with high refractive index sensitivities. In one assay model, phosphocholine-functionalized triangular nanoplates are used to detect human CRP. In the other assay model, monoclonal anti-troponin I antibody-functionalized triangular nanoplates are used to detect human cTnI.

4.2.1 CRP

Over eight decades ago, CRP was initially discovered by Tillett and Francis in the serum of patients with acute pneumococcal pneumonia.[4] It was originally found to possess reactivity with pneumococcal C polysaccharide and was consequently named C-reactive protein.[4, 5] CRP belongs to a protein family known as pentraxins which have been stably conserved during evolution.[6] Each CRP molecule consists of five identical subunits that are attached non-covalently forming a cyclic pentamer with a total molecular weight ranging from 110 to 144 kDa.[7, 8] One important characteristic of CRP is its high affinity for the ligands containing phosphocholine in the presence of calcium. A single molecule of phosphocholine is bound to each subunit of CRP via the choline group, cooperating with the two CRP-bound calcium ions via the phosphate group.[9]

CRP is synthesized and secreted by hepatocytes in the liver as an acute-phase reactant in response to inflammation, infection or tissue injury.[10, 11] The circulating concentration of CRP may elevate rapidly and significantly by 1,000 fold or more within 24 – 48 hours in the presence of various acute phase stimuli.[12-15] The half-life of CRP in plasma is between 18 and 20 hours.[16] It is able to remarkably reduce to the

normal level with the subsidence of symptoms. Therefore, CRP tests have been employed in clinical laboratories to evaluate inflammatory diseases and the response to therapies.[17]

As a marker of inflammation, increased values of CRP have been found in the patients with atherosclerosis[18] and cardiovascular disease including myocardial infarction,[19] myocardial ischemia and unstable angina.[20, 21] Further studies have elucidated a strong correlation between the raised levels of CRP and the potential development, the severity and the prognosis of coronary heart disease.[22-26] Currently, high-sensitivity CRP (hs-CRP) assays, which refer to as the test of CRP using high sensitive method, are being utilized as a predictor to evaluate cardiovascular and stroke risk. According to the American Heart Association, an hs-CRP level of < 1 mg/L, 1 mg/L to 3 mg/L or > 3 mg/L corresponds to a low, average or high risk of developing cardiovascular disease, respectively.[27] Information of some manufactured hs-CRP methods is listed in Table 4.1.

Table 4.1 Characteristics of some commercial hs-CRP assays

Reagent manufacturer	**Reagent description**	**Methodology**	**Assay range (mg/L)**	**LOD (mg/L)**
Denka Seiken	CRP-Latex (II) × 2 High Sensitive Application	IT[a]	0.05–160	0.02
Diagnostic Products Corporation	hsCRP	IL[b]	0.2–100	0.1
Mitsubishi Kagaku Iatron	PATHFAST hsCRP	IL[b]	0.05–30	0.002
Kamiya	K-Assay CRP (I)	IT[a]	0.1–20	0.03
Olympus	CRP (Latex) Sensitive Application	IT[a]	0.5–20	0.08
Roche	Tina-quant CRP (Latex) HS	IT[a]	0.1−20	0.03
Sekisui	Nanopia CRP	IT[a]	0.1–420	0.1
Siemens	Cardiophase hsCRP	IT[a]	0.16−10	0.02
Wako	CRP-HS II LT	IT[a]	1–350	0.1

[a] IT, immunoturbidimetric; [b] IL, immunoluminometric

4.2.2 cTnI

cTnI is a protein subunit of the cardiac troponin complex, which regulates the contraction of cardiac muscle by inhibiting the ATPase activity of actomyosin.[28] Human cTnI, with a molecular weight of around 24 kDa, consists of 210 amino acid residues.[29, 30] Cardiac TnI is reported to express exclusively in heart muscle, and therefore it is considered as a highly cardiac-specific protein.[31]

During the myocardial injury process, the troponin complex is degraded and cTnI is then released into the bloodstream both in free form and complexed with the other subunits (troponin C and cardiac troponin T).[32, 33] In the case of patients with acute myocardial infarction (AMI), cTnI elevates within 6 hours, peaks within 8 to16 hours and remains detectable up to 9 days after the onset of chest pain.[34] The release kinetics makes cTnI an excellent biomarker for detection of AMI. Furthermore, the measurement of serum cTnI is reported to be superior to the conventional measurement of creatinine kinase (CK) and its myocardial isoenzyme (CKMB) in terms of specificity and selectivity for the identification of cardiac injury.[35, 36] Recently, many studies demonstrate that the measurement of cTnI can be used as not only a diagnostic but also a prognostic tool for acute coronary syndromes.[34, 35, 37-39] Moreover, cTnI has been accepted as the gold standard in the diagnosis of myocardial infarction (MI).[40] The 2007 joint European Society of Cardiology, American College of Cardiology Foundation, American Heart Association, and World Heart Federation expert consensus document recommends that the cutoff values for cTnI should be determined for each assay at the 99th percentile of a normal reference population with ≤10% coefficient of variation (CV) in each labarotory.[41] Table 4.2 shows information of some commercial cTnI assays.

Table 4.2 Characteristics of some commercial cTnI assays

Reagent manufacturer	Reagent description	Methodology	Assay range (µg/L)	LOD (µg/L)	99th % (µg/L)
Abbott	ARCHITECT STAT Troponin-I	IL[a]	0.02 – 50	≤ 0.01	0.04
bioMérieux	VIDAS Troponin I Ultra	IL[a]	0.01 − 30	0.01	0.01
Mitsubishi	PATHFAST cTnI	IL[a]	0.02 – 50	0.02	0.02
Ortho	VITROS Troponin I ES	IL[a]	0.012 – 80	0.012	0.034
Roche	Troponin I STAT	IL[a]	0.16−2.5×10^4	0.16	0.16
Siemens	ADVIA Centaur TnI-Ultra	IL[a]	0.008 − 50	0.008	0.04
Tosoh	AIA-PACK cTnI 2nd-Gen	IL[a]	0.02 – 120	0.02	0.02

[a] IL, immunoluminometric

4.3 Experimental methods

4.3.1 Materials

Silver nitrate ($AgNO_3$, ≥ 99.9%), trisodium citrate (TSC), poly(sodium 4-styrenesulfonate) (PSS), sodium borohydride ($NaBH_4$), L-ascorbic acid (AA), tetrachloroauric (III) acid ($HAuCl_4$, ≥ 99.9%), cytidine 5'-diphosphocholine (PC), sodium phosphate dibasic (Na_2HPO_4), sodium phosphate monobasic (NaH_2PO_4), sucrose and CRP were purchased from Sigma-Aldrich and were used as received. Human cTnI and monoclonal anti-TnI antibody were purchased from Fitzgerald Industries International (USA). All glassware used in the synthesis of nanoparticles was first rinsed with concentrated nitric acid (65%) and then rinsed thoroughly with Millipore water and finally water from Sigma-Aldrich before use. All the consumables were obtained from Fisher Scientific. Water purchased from Sigma-Aldrich was used throughout.

4.3.2 Synthesis of TSNPs

The TSNP sols were synthesized according to the method of Aherne *et al.* using a seed-mediated reduction of Ag^+ in aqueous solution as previously described.[1] Typically, the silver seeds were prepared by combining water (4.5 mL), aqueous TSC (0.5 mL, 25 mM), aqueous PSS (0.25 mL, 500 mg/L; 1,000 kDa) and aqueous $NaBH_4$ (0.3 mL, 10 mM), followed by addition of aqueous $AgNO_3$ (5 mL, 0.5 mL) at a rate of 2 mL/min while stirring continuously. The nanoplates were grown from the synthesized seeds by adding aqueous $AgNO_3$ (3 mL, 0.5 mM) at a rate of 1 mL/min to the combination of water (5 mL), aqueous AA (75 μL, 10 mM) and various quantities of seed solution while stirring vigorously. After synthesis, aqueous TSC (0.5 mL, 25 mM) was added to stabilize the nanoparticles.

4.3.3 Synthesis of AuTSNPs

Silver seeds and TSNP sols were prepared via the method stated in section 4.3.2. AuTSNP sols were then synthesized according to the method of Aherne *et al.*[3] by adding AA (150 μL, 10 mM) to one aliquot of the as-prepared TSNP corresponding to 3 mL of added $AgNO_3$ solution, followed by addition of an appropriate volume of $HAuCl_4$ (0.5 mM) at a rate of 0.2 mL/min while stirring vigorously. The volume of $HAuCl_4$ added is observed to correlate to the size of the TSNPs and the location of their LSPR peak wavelength. Figure 4.3 shows the relationship between the volume of $HAuCl_4$ to add and the LSPR peak wavelength of TSNP sols. For instance, the volumes of $HAuCl_4$ to add for the TSNP sols with maximum wavelengths at 600 nm and 700 nm are 170 μL and 79 μL, respectively. This graph was used as a reference for the preparation of AuTSNP sols from TSNP sols.

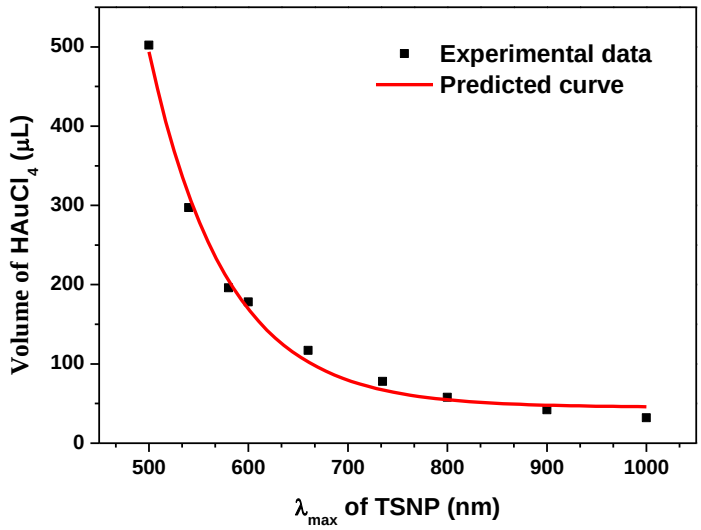

Figure 4.3 Relationship between the volume of $HAuCl_4$ needed to gold coat TSNP sample and the plasmon peak wavelength of TSNP sols. Data supplied by Dr. Damian Aherne, TCD.

4.3.4 CRP assay

The synthesized TSNP and AuTSNP sols were functionalized with PC to prepare the sensors. Typically, PC (0.5 mL, 0.1 M) was added to an aliquot of TSNP or AuTSNP sol (9.5 mL). The PC-TSNP and PC-AuTSNP sols were then incubated overnight at 4 ℃ in the dark. Before the assay performance, the unbound PC molecules were removed through centrifugation for 20 min at 15,616 × g and 4 ℃. The supernatant was discarded and the pellet was resuspended in water. The centrifugation procedure was repeated and the pellet was resuspended to 10% of the initial volume in water. In a typical assay, an aliquot of PC-TSNP or PC-AuTSNP (10 µL) was added to the combination of phosphate buffer (270 µL, 10 mM, pH 7.4), $CaCl_2$ (10 µL, 1 mM) and CRP (10 µL) at various concentrations in phosphate buffer (10 mM, pH 7.4). The concentration of CRP detected in the assay ranged between 3.3×10^{-3} and 3.34 mg/L. The incubation time for the assay was 30 min. All assays were carried out in disposable UV micro cuvettes and characterized using a fiber optic spectrophotometer (Ocean Optics USB4000). The data obtained from the complete assay were fitted with the four-parameter logistic curve model,

$$y = \frac{A_1 - A_2}{1 + \left({}^{x}/_{x_0}\right)^{p}} + A_2 \tag{4.1}$$

where A_1 and A_2 are the lower and upper asymptotes for the binding assay, respectively. The inflection point is given by the variable x_0 and the slope of the tangent in this point is given by the parameter p. The curve-fitting model used is based on an analytical expression, and this logistic function is used as a mathematical model to describe a sigmoid curve progression.

4.3.5 cTnI assay

To remove sodium azide and saline buffer contained in the anti-troponin I (aTnI) antibody stock solution, the antibody (300 μL, 0.2 mg/mL) was dialyzed against phosphate buffer (300 mL, 100 mM, pH 8.0) for 2 hours. The buffer was changed once and 2 more hours were allowed for the dialysis. The TSNP and AuTSNP sols were functionalized with aTnI by adding an aliquot of dialyzed aTnI (80 μL, 0.2 mg/mL) to an aliquot of TSNP or AuTSNP sol (10 mL). The aTnI-TSNP and aTnI-AuTSNP sols were then incubated overnight at 4 ℃. Before the assay performance, the unbound antibody was removed by centrifugation at 9240 × g and 4 ℃ for 20 min. The supernatant was discarded and the pellet was resuspended in water. The centrifugation procedure was repeated and the pellet was resuspended to the original volume in water. In a typical assay, an aliquot of aTnI-TSNP or aTnI-AuTSNP (10 μL) was added to the combination of phosphate buffer (280 μL, 10mM, pH 8.0) and cTnI (10 μL) at various concentrations in phosphate buffer (10 mM, pH 8.0). The concentration of cTnI used in the experiment was ranged from 0.15 to 333 μg/L. The incubation time for the assay was 30 min. The assays were carried out in disposable UV micro cuvettes and characterized using the fiber optic spectrophotometer. The data collected for the complete assay were fitted with the four-parameter logistic model as above.

4.3.6 Refractive index sensitivity measurement

In order to investigate the refractive index sensitivity of the nanoplates, sucrose solutions of various concentrations were prepared by dissolving a range of quantities of sucrose (≥ 99.5%) in water. All the solutions were used at room temperature. Table 4.3

shows the preparation of the sucrose solutions and the corresponding refractive indices in refractive index units (RIU) as generally known using the Brix scale.[42]

Table 4.3 Sucrose solutions of various concentrations and the corresponding Brix scale refractive indices

Sucrose (mg)	Water (mL)	Concentration of sucrose (%)	Brix scale refractive index (RIU)
0	10	0	1.3333
1	9	10	1.3479
2	8	20	1.3639
3	7	30	1.3811
4	6	40	1.3997
5	5	50	1.4200

The refractive index sensitivities of sols including bare TSNP, bare AuTSNP, PC-TSNP, PC-AuTSNP, aTnI-TSNP and aTnI-AuTSNP were measured using the sucrose method. The extinction spectra of the sols suspended in various sucrose solutions were acquired using the optic fiber spectrophotometer. In a typical measurement, 50 μL of a nanoplate sol was added to 350 μL of a certain sucrose solution in a disposable UV micro cuvette.

As the nanoplates are originally suspended in water before they are mixed with the sucrose solutions, the refractive indices of the sucrose-sol mixtures need to be adjusted according to the Lorentz-Lorenz equation,[43, 44]

$$\frac{n_{12}^2 - 1}{n_{12}^2 + 2} = \varphi_1 \frac{n_1^2 - 1}{n_1^2 + 2} + \varphi_2 \frac{n_2^2 - 1}{n_2^2 + 2} \tag{4.2}$$

where n_{12} is the refractive index of the sucrose-sol mixture, n_1 and n_2 are the refractive indices of nanostructure sol (1.3333) and sucrose solution respectively, φ_1 and φ_2 are the volume fractions of the two components. The calculated refractive indices of the sucrose-sol mixtures based on the preparation described above in this section are shown in Table 4.4.

Table 4.4 Refractive indices of the sucrose-sol mixtures used for refractive index sensitivity measurements.

Sucrose concentration (%)	φ_1	φ_2	Refractive index (RIU)
10	0.125	0.875	1.3461
20	0.125	0.875	1.3600
30	0.125	0.875	1.3750
40	0.125	0.875	1.3912
50	0.125	0.875	1.4089

4.4 Results and discussion

4.4.1 Synthesis of TSNPs and AuTSNPs

In this work, the synthesis of TSNPs is based on a two-step seed-mediated method that produces TSNPs in a rapid and reproducible fashion under very mild conditions (room temperature and water as solvent, see section 4.3.2 for details).[1] The first step involves seed preparation by reducing $AgNO_3$ with $NaBH_4$ in the presence of PSS. $NaBH_4$, as a strong reducing agent, is used to rapidly reduce the Ag^+, forming a large quantity of monodisperse silver seed particles. PSS has been observed to play an important role in producing monodisperse nanoplates when growing the nanoplates from the seeds. Though the role of PSS has not been completely understood, it is considered to have a face selectivity and play a shape-directing role during the growth step.[1] The second step involves the growth of silver seeds into TSNPs through the reduction of Ag^+ with AA in the presence of silver seed particles. AA is a mild reducing agent that requires the facilitation of seed particles to reduce the Ag^+, forming silver atoms which are deposited on the seed particles.

Silver nanoparticles tend to chemically degrade due to a catalytic oxidation (etching) of the surface in the presence of halides and other anions.[45-47] Cl^- has been reported to selectively etch the tips and side faces of the silver nanoprism,[48] inducing changes in the nanoprism's geometry (e.g. truncation of apices and reduction of aspect ratio) and thus blueshifting the LSPR wavelength. Therefore, to improve the stability of TSNPs, gold as a more stable metal was used to coat the nanoplates. Typically, a thin layer of gold

was selectively deposited on the edges of the nanoplates through galvanic replacement reaction.[3] Galvanic replacement involves a process by which a metal is deposited as a result of the consumption of another metal with a lower reduction potential. This reaction has been successfully used for preparing bimetallic nanoparticles of various shapes.[49, 50] Figure 4.4 A shows UV-vis spectra of a typical TSNP sol and the AuTSNP sol prepared from it. The gold coating results in an 18 nm redshift in the LSPR peak from 609 nm to 627 nm and a slight broadening of the band. The success of gold coating was determined by placing the AuTSNP sol in 10 mM NaCl for 5 min. As shown in Figure 4.4 B, no shift in the LSPR peak is observed for the AuTSNP sample whereas the LSPR peak of TSNP sol blueshifts to 397 nm in the presence of Cl^-. This indicates that the unprotected TSNPs are etched backed to the silver seed particles as 397 nm is close to the position of the LSPR for small silver nanoparticles.[51]

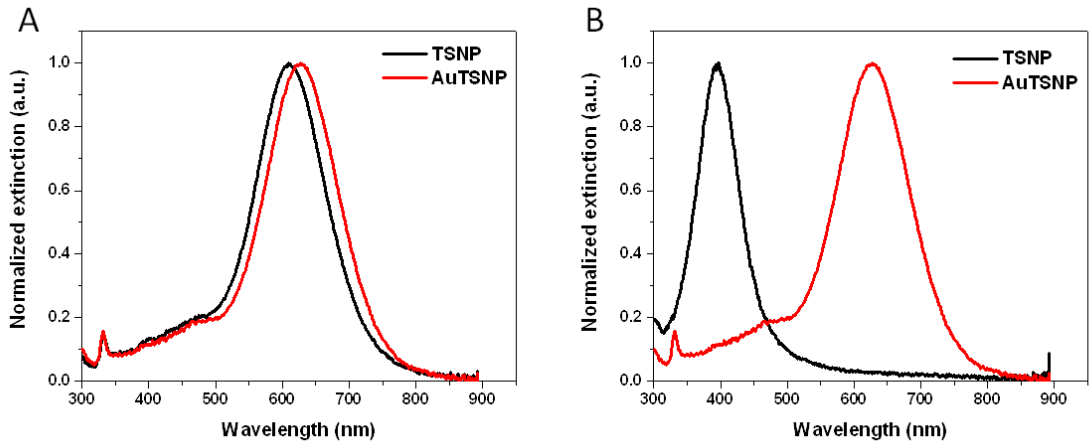

Figure 4.4 (A) UV-vis spectra of a TSNP sol and the AuTSNP sol derived from it; (B) UV-vis spectra of the same sols placed in 10 mM NaCl for 5 min.

4.4.2 CRP assay

4.4.2.1 PC-functionalized nanoplates

PC was used to functionalize the nanoplates including TSNPs and AuTSNPs according to the method described in section 4.3.4. It is postulated that a monolayer of PC is formed on the nanoplate surface by spontaneous adsorption of the molecule to the metallic surface. The interaction between TSNP and the PC molecule may involve the carbonyl group (C=O), amino group ($-NH_2$) and N_1 atom of the cytosine ring, while the

AuTSNP is more likely to interact with carbonyl group (C=O), amino group (-NH_2) and N_3 atom of the cytosine ring (Figure 4.5).[52-55] Moreover, the phosphate and choline groups form a high-affinity binding site for CRP.

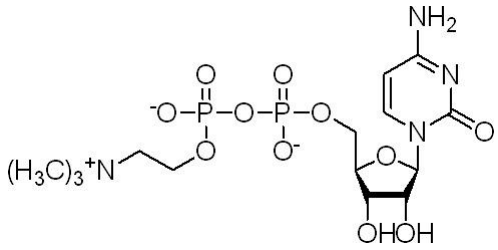

Figure 4.5 Chemical structure of cytidine 5'-diphosphocholine (PC).

Figure 4.6 shows representative UV-vis spectra of TSNP (A) and AuTSNP (B) sols and their corresponding PC-functionalized samples. Upon PC functionalization, TSNP and AuTSNP are found to typically exhibit 7 and 9 nm redshifts in their peak wavelengths, respectively. The redshift in the extinction spectrum is attributed to the adsorption of PC onto the surface of the nanoplate which thereby increases the local refractive index. The magnitude of the redshift is determined by the refractive index sensitivity of the nanoplates as well as the density of PC molecules adsorbed to the surface (i.e. surface coverage). Either high refractive index sensitivity or high surface coverage may result in a large redshift of the plasmon peak.

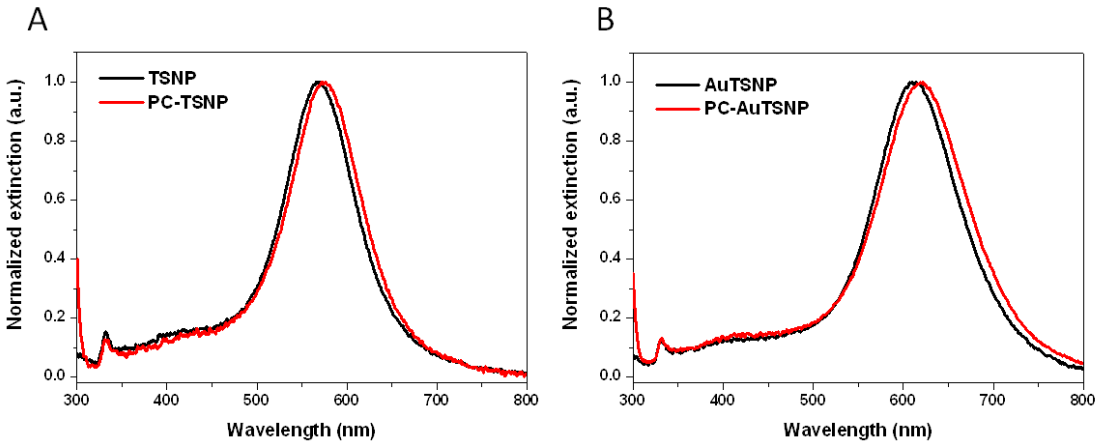

Figure 4.6 (A) Extinction spectra of TSNP sol and its corresponding PC-functionalized sample with LSPR λ_{max} located at 567 nm and 574 nm, respectively; (B) Extinction spectra of AuTSNP sol and its corresponding PC-functionalized sample with LSPR λ_{max} located at 611 nm and 620 nm, respectively.

4.4.2.2 Refractive index sensitivities of the nanoplates

Refractive index sensitivities of the bare TSNP, PC-TSNP, bare AuTSNP and PC-AuTSNP samples before and after centrifugation were determined using the sucrose testing method described in section 4.3.6. This sucrose test provides a simple, reproducible method for the refractive index sensitivity analysis of the nanoplates without causing any destruction and destabilization. It ensures that any shift observed can be ascribed to the variation in the refractive index of the surrounding medium. Therefore, this method is a highly valuable approach for estimating the performance efficiency of the nanoplates as biosensors. Figure 4.7 shows the typical extinction spectra of TSNPs suspended in sucrose solutions of various concentrations corresponding to different refractive indices. The LSPR peak wavelength is observed to redshift as the sucrose concentration is increased, which indeed is also observed for PC-TSNP, bare AuTSNP and PC-AuTSNP sols. Additionally, centrifugation is a necessary preparation step to remove the excess PC molecules before carrying out the CRP assay. Therefore, the effect of centrifugation on the refractive index sensitivities of the nanoplates was investigated.

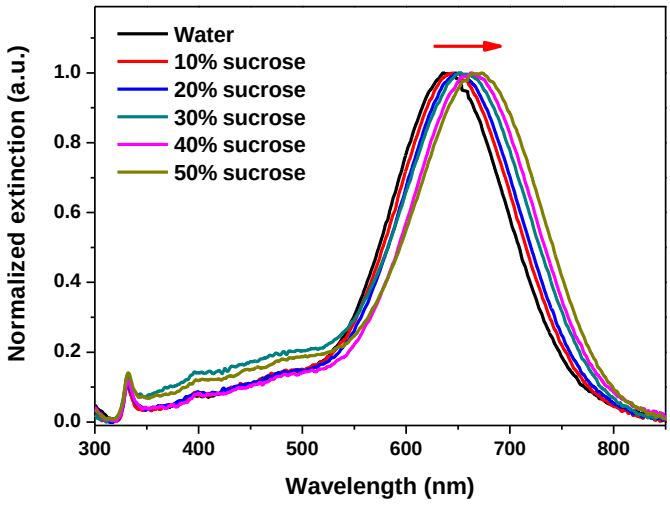

Figure. 4.7 Example of extinction spectra of TSNPs suspended in a range of sucrose solutions.

Figures 4.8 A and B show the refractive index sensitivities of the TSNP and PC-TSNP sols presented in Figure 4.6 A before and after centrifugation. Before centrifugation a

small reduction in the refractive index sensitivity is observed when TSNPs are functionalized with PC molecules (Figure 4.8 A). This observation is in agreement with a previous study of Ag nanoparticles modified with alkanethiol self-assembled monolayers (SAMs).[56] The measured reduction in the sensitivity of the nanoplates may be attributed to the coating of PC. When the LSPR is excited, the enhanced electric fields decay over the length scale of ~ 50 nm.[57] Therefore, the highest sensing capabilities are in the near surface vicinity of the nanoparticle where the electric fields are strongest. The PC coating may act as a barrier impeding sucrose molecules permeating to the surface of the nanoplate and hence shifts the sensing area further away from the surface where the electric fields are less strong. After centrifugation both samples showed decreased refractive index sensitivities when compared to their corresponding values before centrifugation (Figure 4.8 B). The sensitivity of bare TSNPs is reduced by ~ 23% while the sensitivity of PC-TSNPs is reduced by ~ 14%. Upon examination of the extinction spectra for all the samples suspended in water (Figure 4.8 C and D), different magnitudes of blueshift are found when TSNPs and PC-TSNPs are centrifuged, suggesting a reduction in size, i.e. aspect ratio, of the nanoplates. The centrifugation-induced blushift in the LSPR wavelength of the TSNPs has been previously reported by Zeng *et al.*[58] who also observed the truncation of sharp tips for the centrifuged triangular nanoplates. Moreover, the LSPR peak of the PC-TSNP sample shows less blueshift than that of the bare TSNP sample after centrifugation (Figure 4.8 C and D), suggesting that the PC coating may protect the TSNP structure to some extent and reduce the prevalence of truncation.

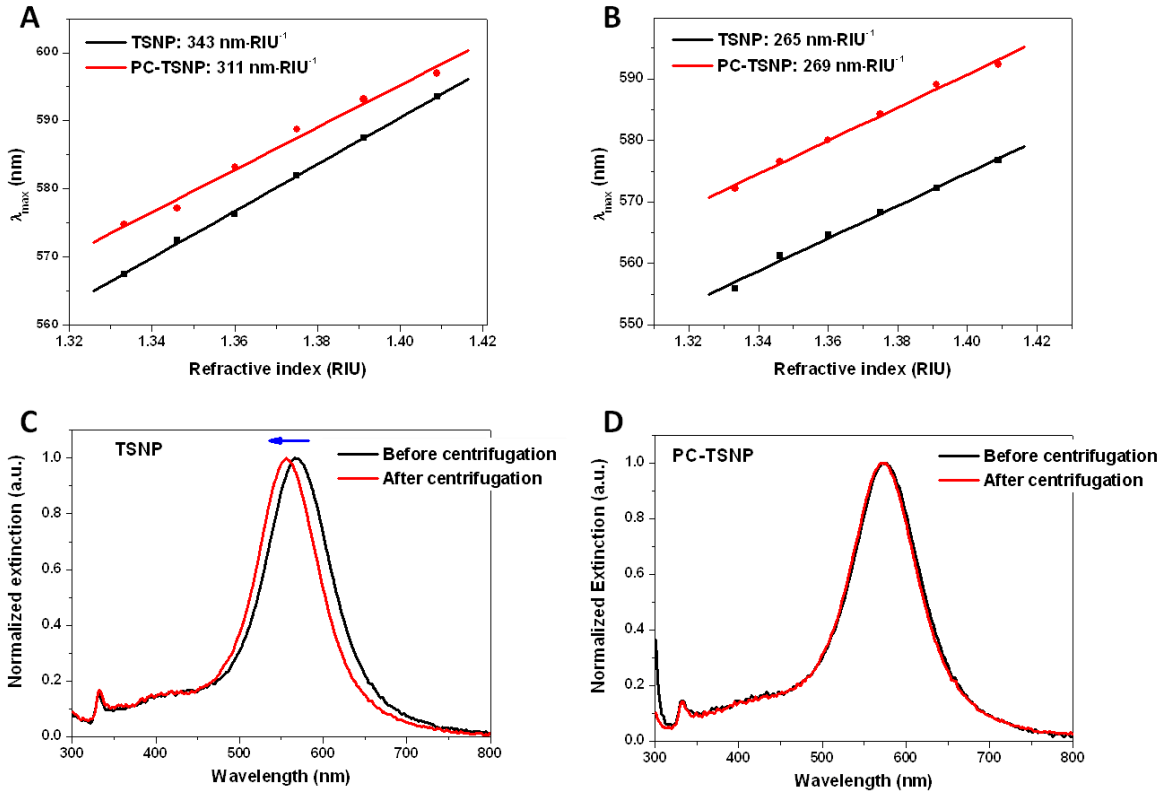

Figure 4.8 (A) Refractive index sensitivities of TSNP and PC-TSNP before centrifugation, (B) Refractive index sensitivities of TSNP and PC-TSNP after centrifugation, (C) Extinction spectra of TSNP before (black curve, λ_{max} = 567 nm) and after (red curve, λ_{max} = 556 nm) centrifugation and (D) Extinction spectra of PC-TSNP before (black curve, λ_{max} = 574 nm) and after (red curve, λ_{max} = 572 nm) centrifugation.

Figures 4.9 A and B show the refractive index sensitivities of the AuTSNP and PC-AuTSNP sols presented in Figure 4.6 B before and after centrifugation. Before centrifugation the sensitivity of AuTSNP is decreased when the sample is functionalized with PC (Figure 4.9 A), which is consistent with the observation for the as-prepared TSNP sample presented in Figure 4.8 A. However, significantly the sensitivities of AuTSNPs and PC-AuTSNPs are found to remain almost unchanged after centrifugation (Figure 4.9 B), which is distinct from the observation for TSNPs and PC-TSNPs (Figure 4.8 B). By analyzing the extinction spectra of the AuTSNP and PC-AuTSNP samples suspended in water (Figure 4.9 C and D), no blueshift is observed for both samples after centrifugation. This is an important result suggesting that no significant change in the

aspect ratio of the nanoplates occurs and that this may be attributed to the protection from the gold coating on the edges of these nanoplates.

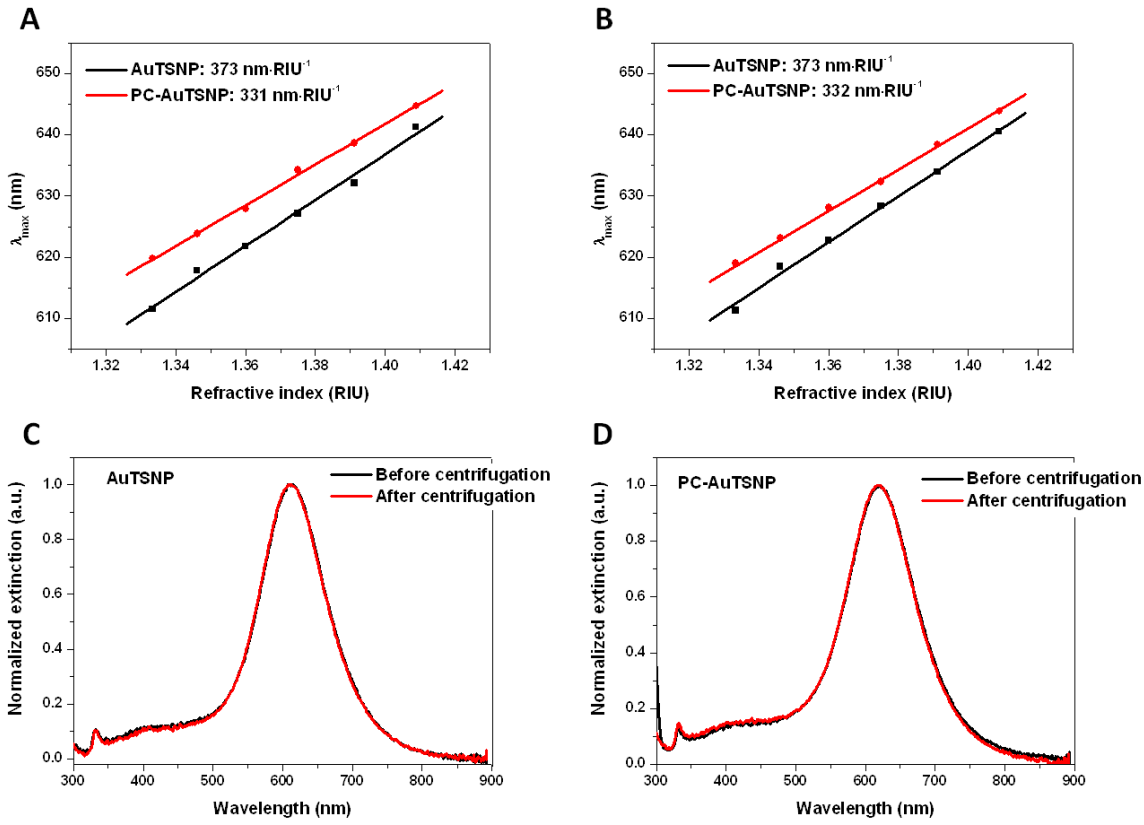

Figure 4.9 (A) Refractive index sensitivities of AuTSNP and PC-AuTSNP before centrifugation, (B) Refractive index sensitivities of AuTSNP and PC-AuTSNP after centrifugation, (C) Extinction spectra of AuTSNP before (black curve) and after (red curve) centrifugation and (D) Extinction spectra of PC-AuTSNP before (black curve) and after (red curve) centrifugation.

The sensitivities of all the samples before and after centrifugation were compared to the Miller line (Figure 4.10). The Miller line is a theoretical upper bound to sensitivities of arbitrary nanoparticles to the changes of local refractive index.[59] It is apparent that the sensitivities of all as-prepared and centrifuged samples exceed the maximum values predicted by the theory of Miller *et al.* (Figure 4.10). In addition, PC-AuTSNPs may present higher sensitivity and stability than PC-TSNP due to the gold coating. These results imply that the PC-AuTSNP sols have the potential to serve as robust and highly sensitive biosensors for detection of CRP.

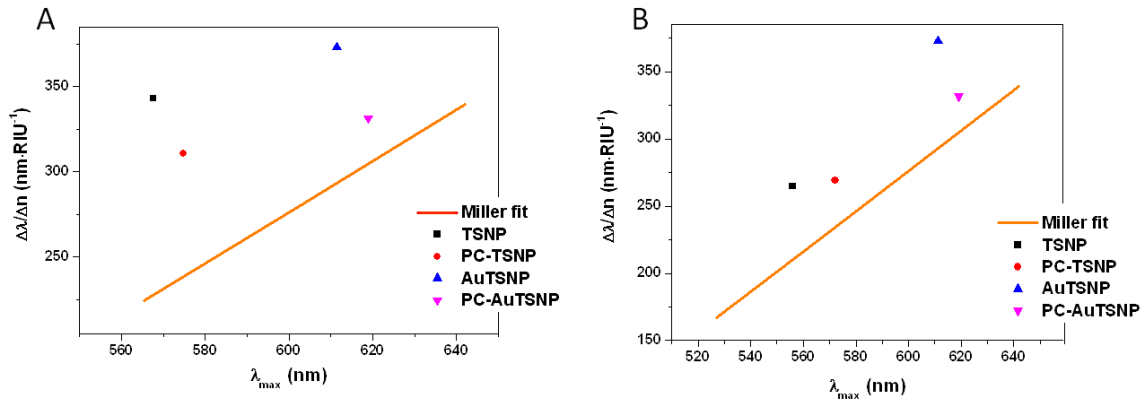

Figure 4.10 Comparison of experimental sensitivities of as-prepared (A) and centrifuged (B) sols to the Miller line.

4.4.2.3 CRP detection

CRP assays were carried out using PC-TSNP and PC-AuTSNP sols via a direct-binding method as described in section 4.3.4. In a typical assay the final concentration of the sensors was estimated to be ~ 2×10^{12} particles per liter. Upon exposing to the CRP dilutions ranging from 3.3×10^{-3} to 3.34 mg/L, different magnitudes of shift in LSPR wavelength were observed for PC-TSNP and PC-AuTSNP sols. The LSPR peak shifts were plotted against the concentrations of CRP as shown in Figure 4.11. For the assay using PC-TSNP (Figure 4.11 red plotting), minute blueshifts are observed when the CRP concentration is below 0.017 mg/L. This can be attributed to the etching of the nanoplates by Cl^- ions from $CaCl_2$ solution. $CaCl_2$ is used in this assay because PC-CRP binding is Ca^{2+} dependent. Above 0.017 mg/L of CRP, the LSPR peak is observed to redshift and experiences an increased redshift as the concentration of the analyte is increased. For the assay using PC-AuTSNP (Figure 4.11 black plotting), no blueshifting is found with a redshift of 0.28 nm in the LSPR peak observed for the lowest concentration of CRP (3.3×10^{-3} mg/L). The redshift increases with CRP concentration. Below 0.67 mg/L of CRP, both PC-TSNP and PC-AuTSNP sensors present similar responses to the analyte. Significantly, when the concentration of CRP is above 0.67 mg/L, the PC-AuTSNP sensor presents a greater redshift than the PC-TSNP in response to the analyte. At the highest analyte concentration (3.34 mg/L), both sensors approach saturation.

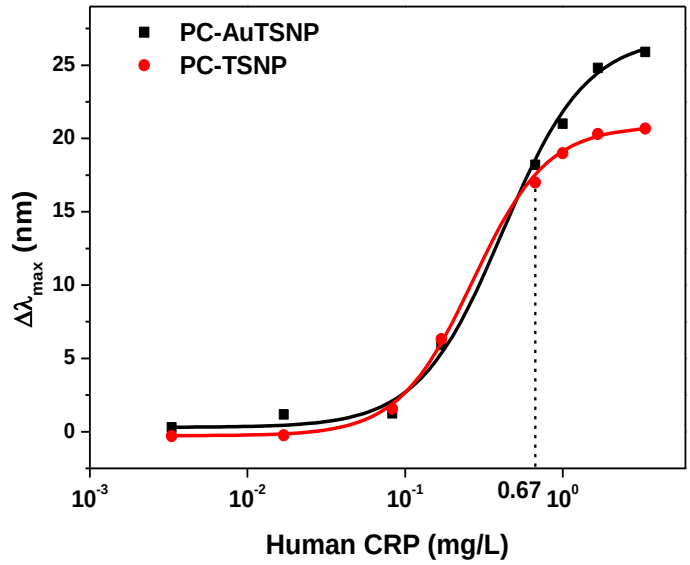

Figure 4.11 LSPR peak shift as a function of the CRP concentration for PC-TSNP (red) and PC-AuTSNP (black).

Clearly, the assay data in Figure 4.11 has the expected shape and demonstrates an improved response for the AuTSNP sample compared to the TSNP sample. This assay is a preliminary study for the detection of CRP and improvements are needed. First of all, blocking of the free sites on the nanoplate surface is needed to prevent non-specific binding. Secondly, a control assay using a protein other than CRP (e.g. IgG) is needed for comparison purposes. Furthermore, the assay needs to be repeated for a number of times to evaluate the LOD and precision. However, there are limitations present due to the subsequent restrictions imposed on the use of these Kelly particles, it was not feasible to make the required improvements as discussed above. This work on solution-phase assays using alternative AuTSNPs will be continued in the next chapter.

4.4.3 cTnI assay

4.4.3.1 aTnI-functionalized nanoplates

aTnI antibody was used to functionalize the nanoplates including both TSNPs and AuTSNPs, by following the procedure outlined in section 4.3.5. The spontaneous adsorption of antibody molecules to the surface of metallic nanoparticles in aqueous solution is complex and dependent on the structure of the protein molecules, ionic

strength, pH and temperature.[60] In general, the antibody molecules when bound to metallic nanoparticles are assumed to retain their bioactivity.[61] The potential interactions between the antibody and the nanoplates include (i) the electrostatic attraction between the positively charged amino acid groups of the antibody and the negatively charged colloids, (ii) the hydrophobic interaction between the hydrophobic pockets of the antibody and the metal surface, and (iii) semi-covalent binding of the metal to free sulfhydryl groups of the antibody, if present.[62] Figure 4.12 shows examples of LSPR peak shifts for TSNP and AuTSNP sols before and after aTnI functionalization. The adsorption of antibody to the nanoplates typically induced a 17 nm redshift for the TSNP sol and a 15 nm redshift for the AuTSNP sol.

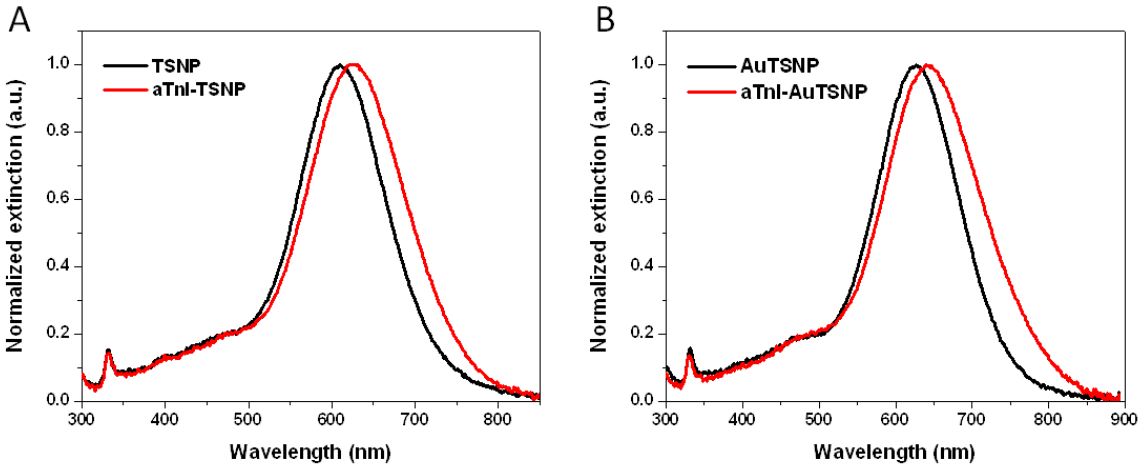

Figure 4.12 (A) Extinction spectra of TSNP sol and its corresponding aTnI-functionalized sample with LSPR λ_{max} located at 609 nm and 626 nm, respectively; (B) Extinction spectra of AuTSNP sol and its corresponding aTnI-functionalized sample with LSPR λ_{max} located at 627 nm and 642 nm, respectively.

4.4.3.2 Refractive index sensitivity analysis

Refractive index sensitivities of bare TSNP, aTnI-TSNP, bare AuTSNP and anti-TnI-AuTSNP samples before and after centrifugation were determined using the sucrose testing method described earlier. The refractive index sensitivities of TSNP and aTnI-TSNP sols before centrifugation are shown in Figure 4.13 A. The sensitivity of the TSNP sample slightly decreased upon functionalization of the nanoplates with the antibody, which is in agreement with the observation for the PC-functionalized TSNP

sol. After centrifugation, both TSNP and aTnI-TSNP sols show decreased sensitivities (Figure 4.13 B). The sensitivity of the bare TSNP sample is reduced by ~ 14% while the sensitivity of aTnI-TSNP sample is reduced by ~ 5%. When examining the extinction spectra of the two sols before and after centrifugation (Figure 4.13 C and D), it is apparent that the LSPR peaks for both TSNP and aTnI-TSNP samples experience different magnitudes of blueshift after centrifugation. As stated previously, the blueshift in the LSPR peak indicates the reduced aspect ratio of the nanoplates which results in a decreased sensitivity to changes of the local dielectric environment. In addition, the plasmon band of aTnI-TSNP sol became broadened after centrifugation (Figure 4.13 D), suggesting that coupling and/or aggregation of the nanoplates may have occurred.

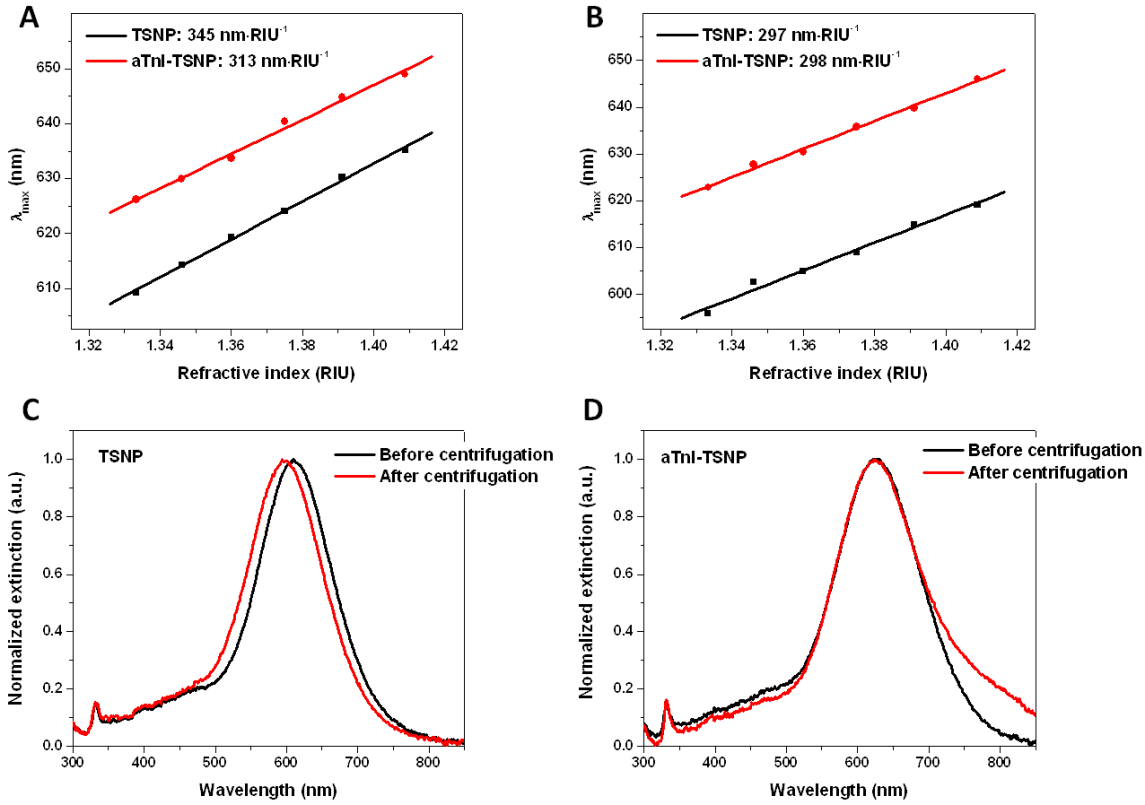

Figure 4.13 (A) Refractive index sensitivities of TSNP and aTnI-TSNP sols before centrifugation; (B) Refractive index sensitivities of TSNP and aTnI-TSNP sols after centrifugation; (C) Extinction spectra of TSNPs suspended in water, showing a peak shift from 609 nm (black) to 596 nm (red) upon centrifugation; (D) Extinction spectra of aTnI-TSNPs suspended in water, showing a peak shift from 626 nm (black) to 623 nm (red) upon centrifugation.

Figure 4.14 A shows the refractive index sensitivities of the as-prepared AuTSNP and aTnI-AuTSNP sols. Similar to the case of CRP, the adsorption of antibody to the metal surface reduces the sensitivity of the nanoplate. After centrifugation, the sensitivity of AuTSNPs remains unchanged while the aTnI-AuTSNP sol exhibits a slightly increased sensitivity (Figure 4.14 B). Upon analyzing the extinction spectra for both samples, no shift is observed in the LSPR peak for AuTSNP and aTnI-AuTSNP after centrifugation (Figure 4.14 C and D). This is attributed to the protection of the gold coating on the edges of TSNP. Similar to the aTnI-TSNP sample, the plasmon band of aTnI-AuTSNPs is broadened after centrifugation, indicating the coupling and/or aggregation of the nanoplates.

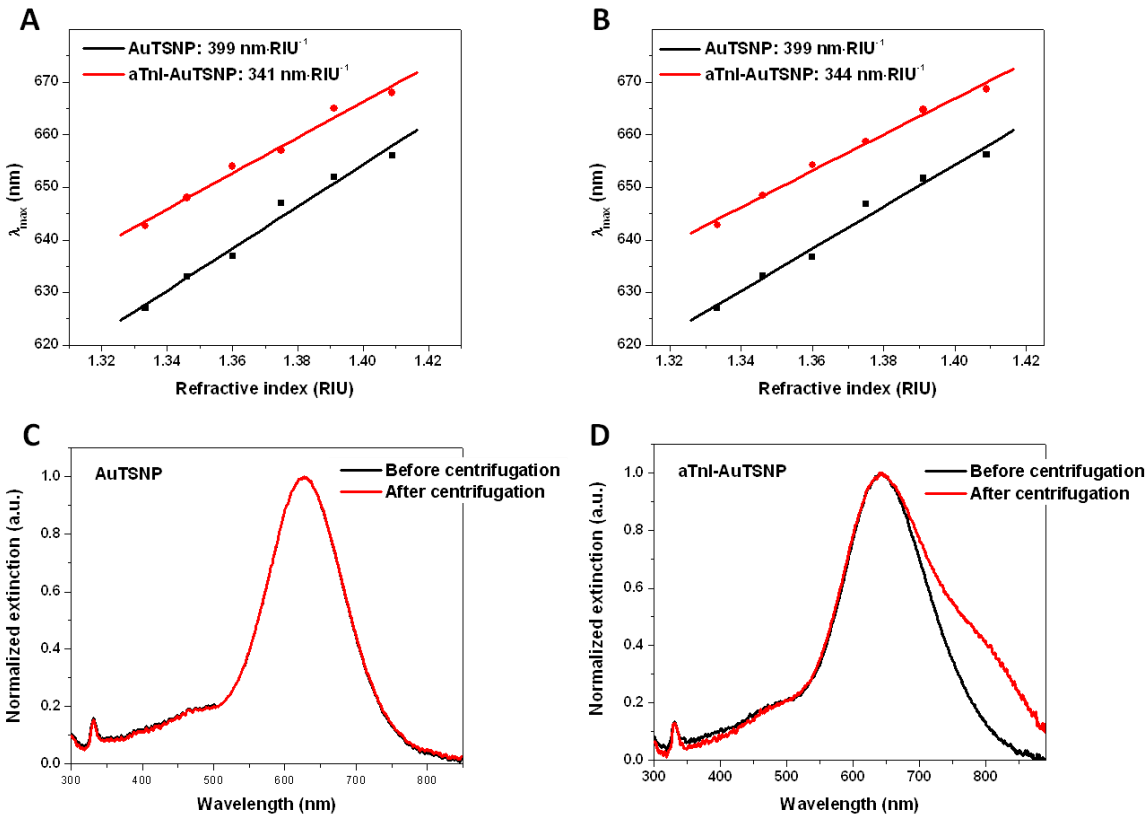

Figure 4.14 (A) Refractive index sensitivities of AuTSNP and aTnI-AuTSNP sols before centrifugation; (B) Refractive index sensitivities of AuTSNP and aTnI-AuTSNP sols after centrifugation; (C) Extinction spectra of AuTSNPs suspended in water (D) Extinction spectra of aTnI-TSNPs suspended in water.

Figure 4.15 displays the refractive index sensitivities observed for all the sols in comparison to the Miller line. Most of the sols give sensitivities above the optimum

values predicted by the theory of Miller *et al.*, while the sensitivities of aTnI-AuTSNPs are slightly below the predicted trend. This would therefore suggest that aTnI-TSNP and aTnI-AuTSNP sols have the potential to serve as highly sensitive sensors for the detection of cTnI.

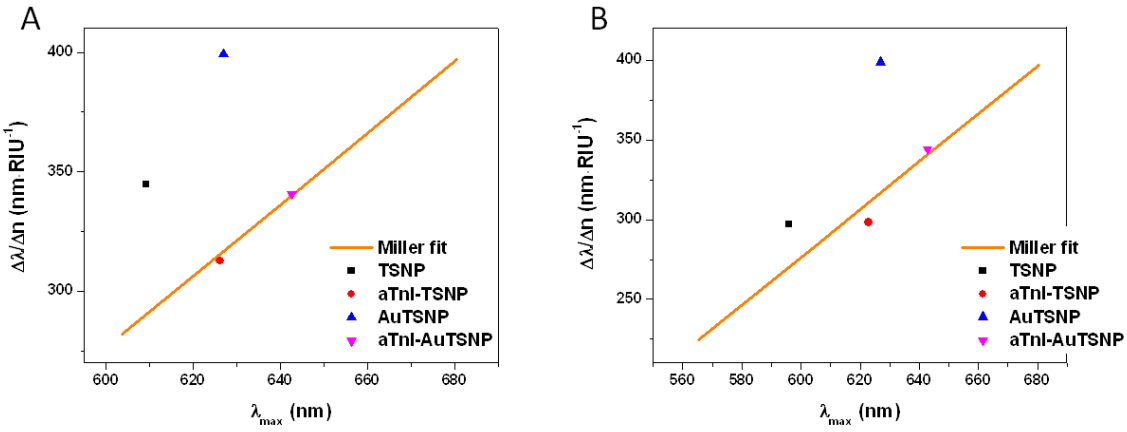

Figure 4.15 Comparison of experimental sensitivities of as-prepared (A) and centrifuged (B) sols to the Miller line.

4.4.3.3 cTnI detection

The aTnI-TSNP and aTnI-AuTSNP sols were used for the cTnI assays by following the protocol described in section 4.3.5. In a typical assay the final concentration of the sensors was estimated to be 2×10^{11} particles per liter. The shifts of the LSPR peak in response to cTnI were plotted against the concentrations of the analyte ranged between 0.15 and 333 µg/L, as shown in Figure 4.16. For the assay using aTnI-TSNPs (Figure 4.16 red plotting), blueshifts in LSPR λ_{max} are observed for the concentrations of cTnI below 4.1 µg/L, indicating that certain etching of the nanoplates may have taken place. When the concentration of cTnI increases to 4.1 µg/L, a redshift of 0.3 nm in the LSPR peak is observed. The redshift continues to increase with the concentration of cTnI up to 333 µg/L. For the assay using aTnI-AuTSNP (Figure 4.16 black plotting), the LSPR peak starts to redshift when cTnI increases to 4.1 µg/L. Additionally, aTnI-AuTSNP sol generally presents a greater redshift than aTnI-TSNP sol in response to different concentrations of cTnI as was found in the case of the CRP assay. At the highest cTnI concentration, both sensors appear not to reach saturation.

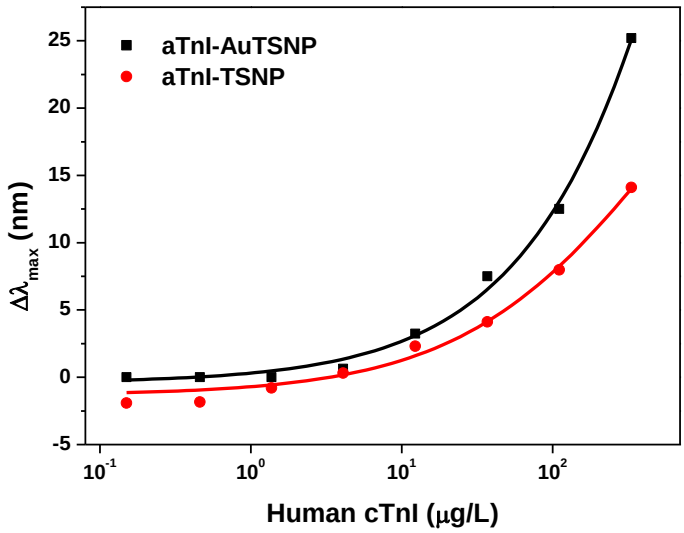

Figure 4.16 LSPR peak shift as a function of the concentration of human cTnI for aTnI-TSNP (red) and aTnI-AuTSNP (black).

Similar to the CRP assay, this assay is a preliminary study on the cTnI detection and improvements are required, including the blocking step, control assay and replication. However, it was impossible to make the improvements due to the restriction on the use of these nanoparticles. While the CRP work is continued in subsequent chapters, unfortunately it was necessary to discontinue the cTnI work, partly due to high costs of the antibodies and also due to the change in direct of the project work.

4.5 Conclusions

In this work, solution-phase TSNPs and AuTSNPs with high refractive index sensitivities have been used as LSPR sensors for one-step, wash-free detection of CRP and cTnI via a direct binding assay format. Though these two assays need to be optimized, the triangular nanoplates have shown excellent potential for efficient biosensing. Particularly, AuTSNPs have shown advantages over TSNPs with respect to stability and sensitivity, which can be further employed in biosensing in physiological environments.

In the case of CRP assays, TSNPs and AuTSNPs were functionalized with PC molecules. The refractive index sensitivities of TSNPs, PC-TSNPs, AuTSNPs and PC-

AuTSNPs were examined before and after centrifugation. Centrifugation, as a necessary process to remove the excess PC from the sols, was found to affect the refractive index sensitivities of the nanoplates. The sensitivities of as-prepared TSNPs and AuTSNPs were observed to decrease upon PC functionalization, indicating the PC molecules adsorbed on the nanoplate surface may dampen the attenuation of the environmental sensitivity. After centrifugation, the sensitivities of both TSNPs and PC-TSNPs reduced whereas those of AuTSNPs and PC-AuTSNPs remained unchanged or slightly increased. It is postulated that centrifugation-induced truncation may contribute to the reduction in the sensitivities of TSNP and PC-TSNP sols. Additionally, gold coating is considered to protect the silver nanoplates against truncation. Sensitivities of the samples exceeded the Miller line regardless of centrifugation, suggesting that PC-TSNPs and PC-AuTSNPs can act as efficient sensors for CRP detection. For the assays using the two sensors, PC-AuTSNPs showed larger LSPR response of the analyte concentration range than PC-TSNPs. Furthermore, a redshift in the LSPR peak of the AuTSNPs was observed for lower analyte concentrations when CRP was as low as 3.3×10^{-3} mg/L.

In the case of the cTnI assay, aTnI was used to functionalize TSNP and AuTSNP sols. Both as-prepared TSNP and AuTSNP sols exhibited reduced refractive index sensitivities upon aTnI functionalization. After centrifugation, the refractive index sensitivities of TSNP and aTnI-TSNP sols decreased whereas those of AuTSNP and aTnI-AuTSNP sols maintained the same or slightly increased. All observations are consistent with those obtained for the bare and PC-functionalized nanoplates. When comparing with the Miller line, aTnI-TSNPs and aTnI-AuTSNPs showed high sensitivities even after centrifugation, suggesting their potential efficiency for the detection of cTnI. For the assays using these two sensors, in both cases the LSPR peaks commenced redshifting when cTnI was 4.1 μg/L.

Both CRP and cTnI assays are preliminary work for biosensing application using triangular nanoplates. Improvements are needed for these two assays, including the blocking of the free sites on the nanoplate surface, the control assay and appropriate replication. In addition, increased performance should be achievable through optimization of the CRP and cTnI assays by controlling several parameters such as the quantity of sensors used, pH, temperature and incubation time. Unfortunately, the work

on the Kelly particles had to be discontinued at this point, due to intellectual property restrictions on the use of the particles, which was outside of my control. Consequently, no improvements were carried out for the CRP and cTnI assays. As indicated above, the CRP assay work will be continued in the next chapter albeit using different AuTSNPs while solid-phase MEF-based CRP assays will be reported in Chapter 6. It was necessary to discontinue the cTnI assay work.

References

1. D. Aherne, D. M. Ledwith, M. Gara and J. M. Kelly, Advanced Functional Materials **18** (14), 2005-2016 (2008).
2. D. E. Charles, D. Aherne, M. Gara, D. M. Ledwith, Y. K. Gun'ko, J. M. Kelly, W. J. Blau and M. E. Brennan-Fournet, ACS Nano **4** (1), 55-64 (2009).
3. D. Aherne, D. E. Charles, M. E. Brennan-Fournet, J. M. Kelly and Y. K. Gun'ko, Langmuir **25** (17), 10165-10173 (2009).
4. W. S. Tillett and T. Francis, The Journal of Experimental Medicine **52** (4), 561-571 (1930).
5. T. J. Abernethy and O. T. Avery, The Journal of Experimental Medicine **73** (2), 173-182 (1941).
6. A. P. Osmand, B. Friedenson, H. Gewurz, R. H. Painter, T. Hofmann and E. Shelton, Proceedings of the National Academy of Sciences of the United States of America **74** (2), 739-743 (1977).
7. T.-Y. Liu, F. A. Robey and C.-M. Wang, Annals of the New York Academy of Sciences **389** (1), 151-162 (1982).
8. A. K. Shrive, G. M. T. Gheetham, D. Holden, D. A. A. Myles, W. G. Turnell, J. E. Volanakis, M. B. Pepys, A. C. Bloomer and T. J. Greenhough, Nat Struct Mol Biol **3** (4), 346-354 (1996).
9. D. Thompson, M. B. Pepys and S. P. Wood, Structure **7** (2), 169-177 (1999).
10. J. Hurlimann, G. J. Thorbecke and G. M. Hochwald, The Journal of Experimental Medicine **123** (2), 365-378 (1966).
11. I. Kushner, Annals of the New York Academy of Sciences **389** (1), 39-48 (1982).
12. S. Black, I. Kushner and D. Samols, Journal of Biological Chemistry **279** (47), 48487-48490 (2004).
13. S. S. Macintyre, D. Schultz and I. Kushner, Annals of the New York Academy of Sciences **389** (1), 76-87 (1982).
14. M. B. Pepys and G. M. Hirschfield, The Journal of Clinical Investigation **111** (12), 1805-1812 (2003).
15. A. Peisajovich, L. Marnell, C. Mold and T. W. Du Clos, Expert Review of Clinical Immunology **4** (3), 379-390 (2008).
16. P. M. Ridker, Circulation **107** (3), 363-369 (2003).
17. T. W. Du Clos, Annals of Medicine **32** (4), 274-278 (2000).

18. I. M. van der Meer, H.-H. S. Oei, A. Hofman, H. A. P. Pols, F. H. de Jong and J. C. M. Witteman, Atherosclerosis **189** (2), 464-469 (2006).
19. P. M. Ridker, N. Rifai, M. A. Pfeffer, F. M. Sacks, L. A. Moye, S. Goldman, G. C. Flaker, E. Braunwald, f. t. Cholesterol and R. E. Investigators, Circulation **98** (9), 839-844 (1998).
20. I. Kushner, M. L. Broder and D. Karp, The Journal of Clinical Investigation **61** (2), 235-242 (1978).
21. F. C. de Beer, C. R. Hind, K. M. Fox, R. M. Allan, A. Maseri and M. B. Pepys, British Heart Journal **47** (3), 239-243 (1982).
22. L. H. Kuller, R. P. Tracy, J. Shaten and E. N. Meilahn, American Journal of Epidemiology **144** (6), 537-547 (1996).
23. E. Haverkate, S. G. Thompson, S. D. M. Pyke, J. R. Gallimore and M. B. P. Group, The Lancet **349** (9050), 462-466 (1997).
24. W. Koenig, M. Sund, M. Fröhlich, H.-G. Fischer, H. Löwel, A. Döring, W. L. Hutchinson and M. B. Pepys, Circulation **99** (2), 237-242 (1999).
25. L. E. P. Rohde, C. H. Hennekens and P. M. Ridker, The American Journal of Cardiology **84** (9), 1018-1022 (1999).
26. J. K. Pai, T. Pischon, J. Ma, J. E. Manson, S. E. Hankinson, K. Joshipura, G. C. Curhan, N. Rifai, C. C. Cannuscio, M. J. Stampfer and E. B. Rimm, New England Journal of Medicine **351** (25), 2599-2610 (2004).
27. T. A. Pearson, G. A. Mensah, R. W. Alexander, J. L. Anderson, R. O. Cannon, M. Criqui, Y. Y. Fadl, S. P. Fortmann, Y. Hong, G. L. Myers, N. Rifai, S. C. Smith, K. Taubert, R. P. Tracy and F. Vinicor, Circulation **107** (3), 499-511 (2003).
28. M. L. Greaser and J. Gergely, Journal of Biological Chemistry **248** (6), 2125-2133 (1973).
29. S. V. Perry, Molecular and Cellular Biochemistry **190** (1), 9-32 (1999).
30. W. J. Vallins, N. J. Brand, N. Dabhade, G. Butler-Browne, M. H. Yacoub and P. J. R. Barton, FEBS Letters **270** (1-2), 57-61 (1990).
31. G. Bodor, D. Porterfield, E. Voss, S. Smith and F. Apple, Clin Chem **41** (12), 1710-1715 (1995).
32. I. Giuliani, J.-P. Bertinchant, C. Granier, M. Laprade, S. Chocron, G. Toubin, J.-P. Etievent, C. Larue and S. Trinquier, Clin Chem **45** (2), 213-222 (1999).

33. I. Giuliani, J.-P. Bertinchant, M. Lopez, H. Coquelin, C. Granier, M. Laprade, B. Pau and C. Larue, Clinical Biochemistry **35** (2), 111-117 (2002).
34. C. Larue, C. Calzolari, J. Bertinchant, F. Leclercq, R. Grolleau and B. Pau, Clin Chem **39** (6), 972-979 (1993).
35. J. Adams, 3d, G. Bodor, V. Davila-Roman, J. Delmez, F. Apple, J. Ladenson and A. Jaffe, Circulation **88** (1), 101-106 (1993).
36. P. O. Collinson, F. G. Boa and D. C. Gaze, Annals of Clinical Biochemistry **38**, 423-449 (2001).
37. B. Cummins, M. L. Auckland and P. Cummins, American Heart Journal **113** (6), 1333-1344 (1987).
38. J. Mair, I. Wagner, B. Puschendorf, P. Mair, P. Lechleitner, F. Dienstl, C. Calzolari and C. Larue, The Lancet **341** (8848), 838-839 (1993).
39. E. M. Antman, M. J. Tanasijevic, B. Thompson, M. Schactman, C. H. McCabe, C. P. Cannon, G. A. Fischer, A. Y. Fung, C. Thompson, D. Wybenga and E. Braunwald, New England Journal of Medicine **335** (18), 1342-1349 (1996).
40. E. Antman, J.-P. Bassand, W. Klein, M. Ohman, J. L. Lopez Sendon, L. Rydén, M. Simoons and M. Tendera, Journal of the American College of Cardiology **36** (3), 959-969 (2000).
41. K. Thygesen, J. S. Alpert, A. S. Jaffe, M. L. Simoons, B. R. Chaitman and H. D. White, European Heart Journal **33** (20), 2551-2567 (2012).
42. F. Schneider and I. C. f. U. M. o. S. Analysis, *Sugar analysis: official and tentative methods recommended by the International Commission for Uniform Methods of Sugar Analysis (ICUMSA)*. (ICUMSA, 1979).
43. R. Mehra, Journal of Chemical Sciences **115** (2), 147-154 (2003).
44. H. Chen, X. Kou, Z. Yang, W. Ni and J. Wang, Langmuir **24** (10), 5233-5237 (2008).
45. X. C. Jiang and A. B. Yu, Langmuir **24** (8), 4300-4309 (2008).
46. P. Mulvaney, T. Linnert and A. Henglein, The Journal of Physical Chemistry **95** (20), 7843-7846 (1991).
47. T. Pal, T. K. Sau and N. R. Jana, Langmuir **13** (6), 1481-1485 (1997).
48. J. An, B. Tang, X. Zheng, J. Zhou, F. Dong, S. Xu, Y. Wang, B. Zhao and W. Xu, The Journal of Physical Chemistry C **112** (39), 15176-15182 (2008).

49. M. Ramos, D. A. Ferrer, R. R. Chianelli, V. Correa, J. Serrano-Matos and S. Flores, Journal of Nanomaterials **2011** (2011).
50. L. Polavarapu and L. M. Liz-Marzan, Nanoscale **5** (10), 4355-4361 (2013).
51. N. Shirtcliffe, U. Nickel and S. Schneider, Journal of Colloid and Interface Science **211** (1), 122-129 (1999).
52. T. Doneux and L. Fojt, ChemPhysChem **10** (9-10), 1649-1655 (2009).
53. J. V. García-Ramos and S. Sánchez-Cortés, Journal of Molecular Structure **405** (1), 13-28 (1997).
54. K.-H. Cho and S.-W. Joo, Bulletin of the Korean Chemical Society **29** (1), 69-75 (2008).
55. M. Östblom, B. Liedberg, L. M. Demers and C. A. Mirkin, The Journal of Physical Chemistry B **109** (31), 15150-15160 (2005).
56. M. D. Malinsky, K. L. Kelly, G. C. Schatz and R. P. Van Duyne, Journal of the American Chemical Society **123** (7), 1471-1482 (2001).
57. T. Jensen, L. Kelly, A. Lazarides and G. C. Schatz, Journal of Cluster Science **10** (2), 295-317 (1999).
58. J. Zeng, S. Roberts and Y. Xia, Chemistry – A European Journal **16** (42), 12559-12563 (2010).
59. M. M. Miller and A. A. Lazarides, The Journal of Physical Chemistry B **109** (46), 21556-21565 (2005).
60. F. R. Eirich, Journal of Colloid and Interface Science **58** (2), 423-436 (1977).
61. M. Horisberger, Gold Bull **14** (3), 90-94 (1981).
62. G. T. Hermanson, *Bioconjugate Techniques*. (Academic Press, 2008).

Chapter 5

Nanoparticles for development of sensitive assays

5.1 Introduction

This chapter focuses on the development of immunoassays using nanoparticles for biosensing applications, including LSPR refractive index sensitivity-based assays, aggregation-based assays and nanoparticle-enhanced SPR assays. The LSPR refractive index sensitivity-based assay involves the detection of human CRP using antibody-conjugated AuTSNP sols. This part of the work continues on from that of Chapter 4 except the AuTSNPs used are synthesized using a different method from that used for the Kelly particles. For reasons explained later, aggregation-based assays and nanoparticle-enhanced SPR assays, both for human IgG, were also investigated.

5.2 Overview of assays

Three different types of assays were used in this section of the work, (i) LSPR refractive index sensitivity-based assay, following on from Chapter 4, using the AuTSNPs, (ii) aggregation-based assay using spherical gold particles (AuNPs) and (iii) nanoparticle-enhanced SPR assay using the AuTSNPs.

5.2.1 Refractive index sensitivity-based assay

Instead of PC which was used in Chapter 4, two types of monoclonal anti-human CRP (aCRP) antibodies C2 and C6 are used to functionalize the AuTSNPs, forming C2-AuTSNP and C6-AuTSNP conjugates. These two antibodies specifically bind to different epitopes of the CRP molecule, and hence C2-AuTSNP and C6-AuTSNP conjugates can be used individually or cooperatively for the detection of CRP. The mechanism for the assay based on LSPR refractive index sensitivity has been discussed in Chapter 4 (Figure 4.2). In this chapter, C2-AuTSNP and C6-AuTSNP conjugates were individually used for CRP assays. Additionally, a 1:1 mixture of these two sensors was used for CRP detection. Due to the pentameric structure of the CRP molecule and

the fact that one antibody can bind to one CRP monomer, it is possible that more than one sensor binds to a CRP molecule forming aggregates. All assays were characterized with a UV-vis spectrophotometer and DLS.

5.2.2 Aggregation-based assay

The aggregation-based assay involves the detection of human IgG in aqueous solution using antibody-conjugated spherical gold nanoparticles (AuNPs) (Figure 5.1). It was decided to use IgG here for this model assay instead of CRP for cost reasons, coupled with the fact that the main focus was to compare the relative performance of this commonly used assay format with that of the LSPR refractive index sensitivity approach. Polyclonal anti-human IgG (H+L) antibody (aIgG) was used to functionalize 13 nm AuNPs, forming aIgG-AuNP conjugates. The antibody reacts with both heavy and light chains of a human IgG molecule at different epitopes. Therefore, it is easy to cause aggregation of the AuNPs when the analyte is added to the aIgG-AuNP solution. The aIgG-AuNP sol is red in color with an LSPR wavelength peaked at 525 nm. The aggregation of the AuNPs results in a redshift of the LSPR peak due to the electric dipole-dipole interaction and coupling between the plasmons of the adjacent particles in the aggregates.[1] In addition, the LSPR wavelength region between 580 and 800 nm experiences substantial changes in the extinction intensity during aggregation, which can be monitored for the aggregation progress.[1-4] In this experiment, the largest change in LSPR extinction at longer wavelength occurred at 600 nm. Therefore, the aggregation rate of aIgG-AuNPs in the presence of various IgG concentrations was monitored by measuring the extinction of the sol at 600 nm. In addition, the aggregation process was characterized using TEM and the size of the aggregates formed in the assay was measured using DLS.

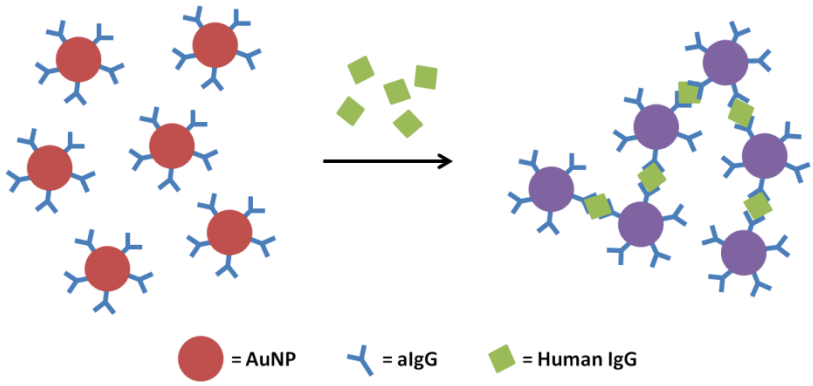

Figure 5.1 Schematic illustration of aggregation-based assay for human IgG detection using AuNPs.

5.2.3 Nanoparticle-enhanced SPR assay

This assay design incorporates AuTSNPs in an SPR assay for real-time detection of human IgG. As shown in Figure 5.2, the assay is performed on the gold surface of a commercial sensor chip. Protein A is immobilized on the gold surface to capture human IgG via a specific interaction with the Fc region of the antibody. The aIgG-AuTSNP conjugates are used to bind to the analyte at specific epitopes. A control assay using free aIgG is performed under the same conditions for comparison purposes. The utilization of AuTSNPs results in significantly improved SPR response due to three main factors: (i) an increase in the refractive index of the analyte, (ii) the plasmon resonant coupling between the nanoplates and the gold film, and (iii) an increase in the surface mass.[5] All experiments were carried out using a Biacore 3000 system which was described in Chapter 3.

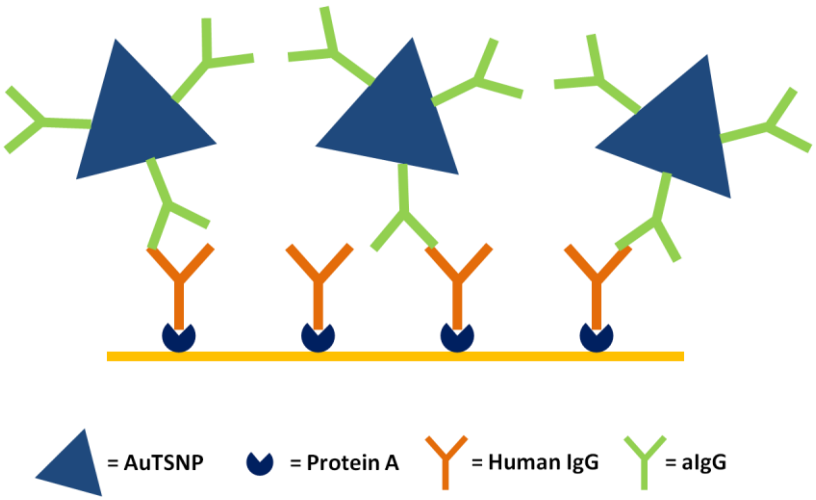

Figure 5.2 Schematic illustration of AuTSNP-enhanced SPR detection of human IgG.

5.3 Experimental methods

5.3.1 Materials

$AgNO_3$ (≥ 99.9%), TSC, $NaBH_4$, AA, hydrogen peroxide (H_2O_2, 30 wt. %), $HAuCl_4$ (≥ 99.9%), sodium chloride (NaCl), boric acid (H_3BO_3), sodium tetraborate decahydrate ($Na_2B_4O_7{\cdot}10H_2O$), Na_2HPO_4, NaH_2PO_4, phosphate buffered saline (PBS, pH 7.4), sucrose, nitric acid (HNO_3, 69%), sulfuric acid (H_2SO_4, 95-98%) and polyclonal anti-human IgG (Fab specific) antibody were purchased from Sigma-Aldrich and were used as received unless mentioned otherwise. Human CRP was purchased from Millipore (USA). Monoclonal mouse anti-human CRP antibodies C2 and C6 were purchased from HyTest (Finland). Protein A was purchased from Fisher Scientific (USA). Human IgG was purchased from SeraCare (USA). Bovine serum albumin (BSA) and polyclonal goat anti-human IgG (H+L) antibody were purchased from Jackson ImmunoResearch (USA). Gold sensor chips (SIA kit Au) were purchased from GE Healthcare (Sweden). All glassware used in the synthesis of nanoparticles was first rinsed with concentrated HNO_3 (69%) and then rinsed thoroughly with Millipore water before use. All the consumables were obtained from Fisher Scientific. Millipore water was used throughout.

5.3.2 Refractive index sensitivity-based CRP assay using AuTSNP

5.3.2.1 Synthesis of AuTSNP

The TSNP sol was synthesized using the method of Zhang *et al.* instead of the method of Aherne *et al.* used in Chapter 4.[6] In a typical experiment, aqueous $AgNO_3$ (0.05M, 50 µL), TSC (75 mM, 0.5 mL) and H_2O_2 (30 wt. %, 60 µL) solutions were added to 24.14 mL of water with vigorous agitation at room temperature in air, followed by rapid addition of $NaBH_4$ (100 mM, 0.25 mL) to the mixture. Within 10 min, the solution turned from light yellow to dark yellow and finally blue. The size of the nanoplates can be varied by adjusting the concentration of added $NaBH_4$.

The AuTSNP sol was prepared by adopting a previously reported method.[7] Typically, AA (10 mM, 50 µL) was added to 5 mL of as-prepared TSNP sol with rigorous agitation, followed by the gradual addition of $HAuCl_4$ (0.5 mM, 100 µL). The success of the Au coating was determined by exposing the nanoplates to 10 mM NaCl. UV-vis spectra were taken after 5 min incubation to monitor the stability of the sample.

5.3.2.2 aCRP-AuTSNP conjugation

Monoclonal mouse anti-human CRP antibodies (aCRPs) C2 and C6 were used to functionalize the nanoplates. Before adding antibody to the sol, the as-prepared AuTSNP sol was centrifuged at 20℃ and 16,100 × g for 15 min. The supernatant was removed and the pellet was resuspended in 0.01M borate buffer (BB, pH 8.5). In order to determine the quantity of antibody to be added to an aliquot of AuTSNP sol, different concentrations of antibody ranging from 2.5 to 10 µg/mL were used to functionalize aliquots of the sol. Following 2h incubation, the sols were incubated in 0.05 M NaCl for 2 h and then were characterized with a Cary 50 UV-vis spectrophotometer.

In order to prepare the aCRP-AuTSNP conjugates for CRP assay, antibodies C2 and C6 were used to functionalize two aliquots of AuTSNP sol, respectively. The final concentration of C2 or C6 in the sol was 10 µg/mL. After 2 h incubation with gentle shaking, BSA (final concentration 5 µg/mL) was added and the sols were incubated for another hour. The antibody-functionalized AuTSNP sols were then stored at 4 ℃ before use.

Prior to the assay performance, the unbound antibody was removed by centrifuging the sol for 20 min at 4 ℃ and 9240 × g. The supernatant was discarded and the pellet was resuspended in BB (0.01 M, pH 8.5) containing 10 µg/mL BSA. The centrifugation procedure was repeated and the pellet was resuspended to one third of the initial volume in BB (0.01 M, pH 8.5) containing 10 µg/mL BSA.

5.3.2.3 CRP detection

C2-AuTSNPs, C6-AuTSNPs and a 1:1 mixture of these two sensors were used for CRP detection. In a typical assay using individual aCRP-AuTSNP conjugates (C2-AuTSNPs or C6-AuTSNPs), 10 µL of CRP at various concentrations was added to the combination of 50 µL of aCRP-AuTSNP (C2-AuTSNP or C6-AuTSNP) sol and 40 µL of phosphate buffer (PB, 0.01M, pH 7.2) containing 10 µg/mL BSA. In a typical assay using the 1:1 mixture of both conjugates, 10 µL of CRP at various concentrations was added to the combination of 25 µL of C2-AuTSNP sol, 25 µL of C6-AuTSNPs sol and 40 µL of phosphate buffer (PB, 0.01M, pH 7.2) containing 10 µg/mL BSA. The concentrations of CRP used in those two types of assay ranged from 0.86 to 110 mg/L. Human IgG (110 mg/L) was used as negative control. All assays were performed in triplicate on a 96-well microplate (Greiner Bio-One) at room temperature. Separately, the assays were monitored for 2 h using a plate reader (Tecan, USA) as discussed later. The LOD of the assay was calculated from the mean signal of the lowest concentration of CRP producing a signal higher than the zero calibrator plus three standard deviations (SDs). The assays with 90 min incubation were also characterized using Delsa Nano C (Beckman Coulter, USA) for particle size analysis.

5.3.2.4 Refractive index sensitivity measurement

The refractive index sensitivities of the bare AuTSNP, C2-AuTSNP and C6-AuTSNP sols before and after centrifugation were measured using the sucrose method described in section 4.3.6.

5.3.2.5 TEM

TEM of AuTSNPs was performed with a Tecnai G^2 20 twin microscope (FEI, USA), operating at an acceleration voltage of 200 kV. To prepare the TEM sample, an aliquot of AuTSNP sol was centrifuged for 15 min at 16,100 × g. The supernatant was removed

and the pellet was resuspended to 10% of the initial volume. A 10 µL aliquot of concentrated sol was dropped on a 300 mesh copper grid coated with Formvar/carbon (Agar Scientific, UK) and dried in air for one hour. The excess solution was wicked away and the sample was further dried overnight prior to imaging. The size analysis of the nanoplates was performed using ImageJ.

5.3.3 Aggregation-based IgG assay using AuNP

5.3.3.1 Synthesis of AuNP

Spherical AuNPs were synthesized by TSC reduction of $HAuCl_4$.[8, 9] Aqueous TSC (38.8 mM, 25 mL) was added to an aqueous solution of $HAuCl_4$ (1 mM, 250 mL) when it was brought to the boil with vigorous stirring. The mixture was refluxed for 20 min during which time the solution turned from pale yellow to deep red. After the solution was cooled to room temperature, it was filtered through a 0.2 µm Isopore membrane filter (Millipore). The resulting Au colloid was stored at 4℃ in the dark before use.

5.3.3.2 aIgG-AuNP conjugation

AuNPs were functionalized with polyclonal goat anti-human IgG (H+L) (aIgG) via spontaneous adsorption. Before functionalization, an aliquot of AuNP sol was centrifuged for 12 min at 16,100 × g. The supernatant was removed and the pellet was resuspended to the original volume in BB (0.01 M, pH 8.5). To determine the quantity of aIgG to be added, different concentrations of aIgG ranging from 5 to 25 µg/mL were used to functionalize aliquots of the AuNP sol. Following 2 h incubation, the sols were incubated in 0.05 M NaCl for 2 h and then were characterized with the UV-vis spectrophotometer.

To prepare the aIgG-AuTSNP conjugates for IgG assay, aIgG (20 µg/mL) was used to functionalize an aliquot of AuTSNP sol. After 2 h incubation with gentle shaking, BSA (final concentration 0.1%) was added and the sol was incubated for another hour. The aIgG-AuTSNP sol was then stored at 4 ℃ before use.

Prior to the assay performance, the unbound antibody was removed by centrifugation for 12 min at 4 ℃ and 15,616 × g. The supernatant was discarded and the pellet was resuspended in PB (0.01 M, pH 7.2) containing 0.1% BSA. The centrifugation

procedure was repeated and the pellet was resuspended to half of the initial volume in PB (0.01 M, pH 7.2) containing 0.1% BSA.

5.3.3.3 IgG detection

In a typical assay, 10 µL of CRP at various concentrations was added to the combination of 50 µL of aIgG-AuNP sol and 40 µL of PB (0.01 M, pH 7.2) containing 0.1% BSA. The concentrations of IgG used in this assay ranged from 0.78 to 400 mg/L. Anti-human IgG (Fab specific) antibody (200 mg/L) was used as negative control. All assays were performed in triplicate on a 96-well microplate (Greiner Bio-One) at room temperature. As previously, the assays were monitored for 2 h using a plate reader (Tecan, USA). In addition, the assays incubated for 90 min were characterized using Delsa Nano C (Beckman Coulter, USA) for particle size analysis.

5.3.3.4 TEM

The AuNPs were characterized with a Tecnai G^2 20 twin microscope (FEI, USA) operated at 200 kV. The TEM sample was prepared using the method described in section 5.3.2.5. The IgG assay incubated for various durations was characterized with TEM. Typically, a 10 µL aliquot of the assay sample was dropped on a 300 mesh copper grid coated with Formvar/carbon (Agar Scientific, UK) and dried in air for one hour. The excess solution was wicked away and the sample was further dried overnight prior to imaging.

5.3.4 AuTSNP-enhanced SPR detection of human IgG

5.3.4.1 aIgG-AuTSNP conjugation

Polyclonal anti-human IgG (H+L) antibody (aIgG) was used to functionalize the AuTSNP sol that was prepared with the method stated in section 5.3.2.1. Typically, an aliquot of AuTSNP sol was functionalized with 10 µg/mL of aIgG and blocked with 5 µg/mL of BSA using the method described in section 5.3.2.2. The aIgG-AuTSNP sol was stored at 4 ℃ before use.

Before the assay performance, the unbound aIgG was removed from the sol by centrifugation for 20 min at 4 ℃ and 9240 × g. The supernatant was discarded and the pellet was resuspended in BB (0.01 M, pH 8.5) containing 10 µg/mL of BSA. The

centrifugation was repeated and the pellet was resuspended to the original volume in PBS (0.01 M, pH 7.4) containing 10 µg/mL of BSA.

5.3.4.2 IgG assay using AuTSNP-enhanced SPR

In a typical experiment, a gold chip (SIA kit Au) was cleaned with acid piranha (a 3:1 mixture of concentrated H_2SO_4 and 30% H_2O_2) for 2 min. Next, the chip was rinsed thoroughly with water and assembled onto the holder. The IgG assay performed on the Au chip was monitored by Biacore 3000. PBS (0.01M, pH 7.4) was used throughout. The volume of each reagent was 100 µL with a flow rate of 10 µL/min. Four flow cells were used for a set of assay. Flow cells 2 and 4 were assigned to the control and AuTSNP-enhanced assay, respectively. Flow cells 1 and 3 were assigned to the corresponding reference cells of flow cells 2 and 4. For the AuTSNP-enhanced assay, protein A (50 µg/mL), BSA (1%), human IgG at various concentration and aIgG-AuTSNP were sequentially injected to flow cell 4. The same reagents except protein A were injected to the corresponding reference cell (i.e. flow cell 3). For the control assay, protein A (50 µg/mL), BSA (1%), human IgG at various concentration and aIgG (1 µg/mL) were sequentially injected to the flow cell 2. The same reagents except protein A were injected to the corresponding reference cell (i.e. flow cell 1). The concentrations of human IgG ranged from 0.001 to 10 µg/mL.

5.4 Results and discussion

5.4.1 Refractive index sensitivity-based CRP assay using AuTSNP

5.4.1.1 Synthesis and characterizations of AuTSNP

As discussed at the beginning of this chapter, it was necessary to adopt a different particle synthesis approach for the remaining work on solution assays. The method reported by Zhang *et al.* for the preparation of TSNPs was chosen.[6] The method of Zhang *et al.* involves the reduction of $AgNO_3$ with $NaBH_4$ in the presence of H_2O_2 and TSC. $NaBH_4$ is a strong reducing agent that reduces Ag^+ to form Ag nanoparticles and TSC acts as a stabilizer to keep the particles from aggregating. H_2O_2 plays a critical role in determining the shape evolution into triangular nanoplates. To improve the stability of the silver nanoplates against etching, a thin layer of gold was coated on the edges of the nanoplates by adopting the method reported by Aherne *et al.*for the Kelly particles.[7]

Figure 5.3 A shows an example of a TSNP sol and the corresponding AuTSNP sol derived from it. The gold coating induces a small redshift and a slight broadening of the LSPR wavelength, similar to that described in Chapter 4. The success of the gold coating was monitored by placing an aliquot of AuTSNP sol in 10 mM NaCl solution for 5 min. Figure 5.3.B illustrates the effect of 10 mM NaCl on the TSNPs and AuTSNPs after 5 min. The TSNPs are etched back to small silver particles as indicated by the LSPR blueshifting to 395 nm which is the characteristic LSPR wavelength for small spherical silver particles.[10] In contrast, the AuTSNP sol shows high stability with no change in the LSPR wavelength in 10 mM NaCl, indicating successful and complete gold coating, again similar to the behavior of the Kelly particles.

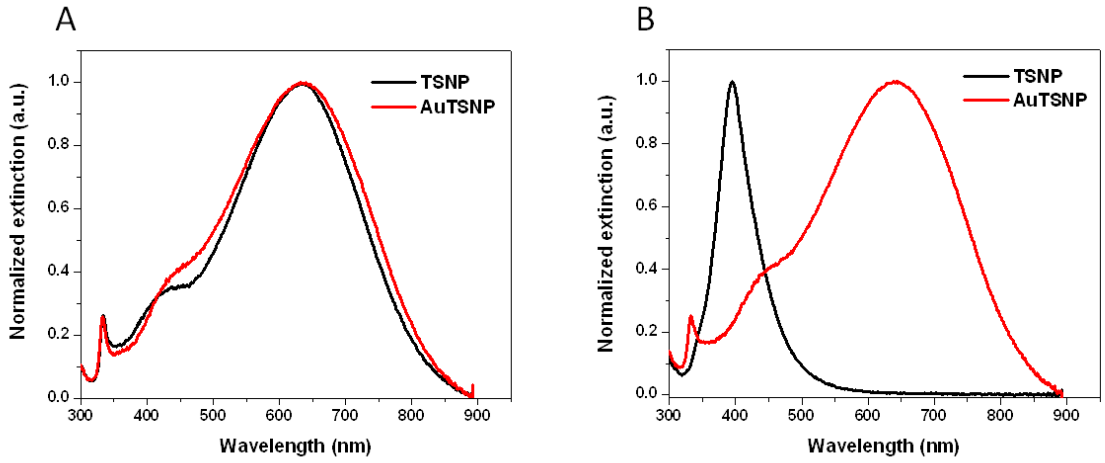

Figure 5.3 (A) UV-vis spectra of TSNPs (black) and AuTSNPs (red) suspended in water; (B) UV-vis spectra of the same samples after 5 min in 10 mM NaCl.

A representative set of alternative AuTSNPs was compared with a set of AuTSNPs prepared using the method of Aherne *et al.*. The two sets of AuTSNPs have a LSPR peak located at 695 nm as shown in Figure 5.4. Apparently, the alternative AuTSNPs exhibit much broader plasmon band than the nanoplates prepared using the method of Aherne *et al.*, indicating the former have greater size distribution and inhomogeneity within the sol. Both samples were characterized with TEM as shown in Figure 5.5. The mean edge length for the nanoplates prepared using the method of Aherne *et al.* and the alternative nanoplates is 41 ± 9 nm and 30 ± 8 nm, respectively. The nanoplates prepared using the method of Aherne et al. (CV = 22%) are more homogeneous than the altenative nanoplates (CV = 27%). According to the AFM measurement stated in

Chapter 6, the thickness of the alternative nanoplates is ~ 7 nm which is similar to that of the nanoplates prepared using the method of Aherne *et al*..[11] This therefore results in aspect ratio being ~ 4.3 for the alternative nanoplates and ~ 5.9 for the nanoplates prepared using the method of Aherne *et al.*. In both samples, most of the nanoplates are triangular with varying degrees of tip truncation while a few nanoframes are observed due to the galvanic replacement of the silver by the gold.[7]

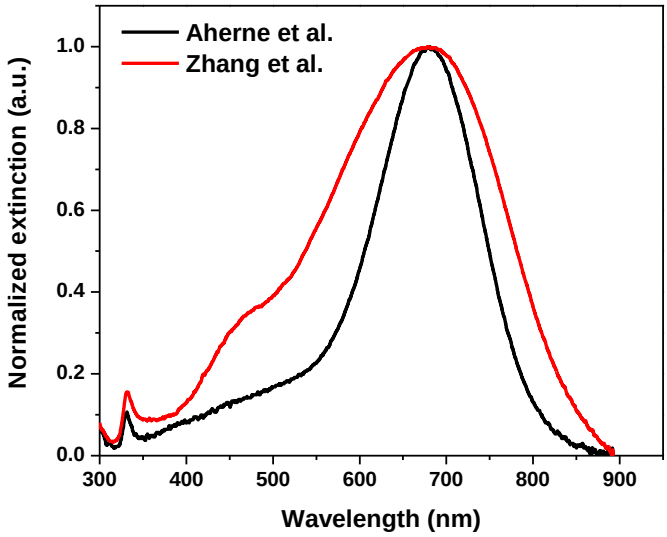

Figure 5.4 UV-vis spectra of representative AuTSNP samples prepared using the method of Aherne *et al.* (black) and the method of Zhang *et al.* (red).

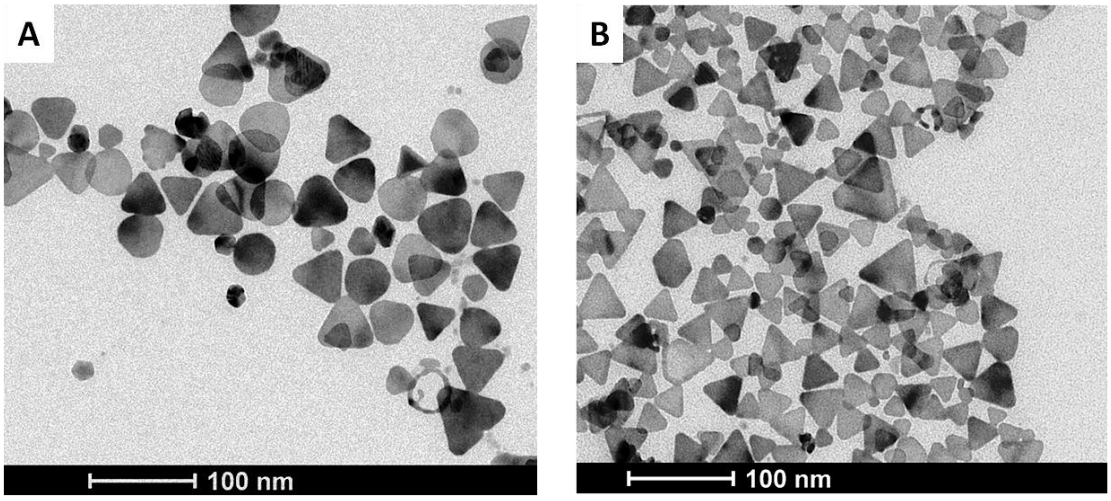

Figure 5.5 TEM images of AuTSNP samples prepared using the method of Aherne *et al.* (A) and the method of Zhang *et al.* (B).

5.4.1.2 aCRP-AuTSNP conjugation

The addition of electrolyte such as NaCl to the colloidal suspension induces aggregation of the nanoparticles due to the screening of the repulsive electrostatic interactions between the particles. As shown in Figure 5.6, the concentration of NaCl causing AuTSNP aggregation is ~ 0.03 M, after 1 h incubation. When the concentration of NaCl increases to 1 M, the LSPR spectrum of the AuTSNP is undetectable, suggesting the nanoplates aggregate and completely fall out of the solution. These observations provide an estimation of the nanoplates' stability and an indication of the appropriate ionic strength for the antibody-AuTSNP conjugation.

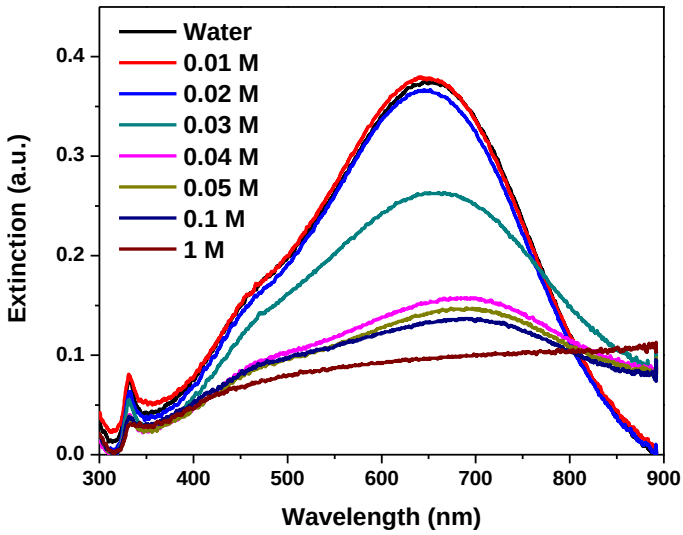

Figure 5.6 UV-vis spectra of AuTSNPs suspended in different concentrations of NaCl for 1 h.

As discussed earlier in section 5.2.1, two types of aCRP antibodies, C2 and C6, were used to functionalize the nanoplates, which specifically bind to different epitopes of a CRP molecule. The antibody-AuTSNP conjugates are formed by spontaneous adsorption of the protein on the surface of the nanoplates with the interactions involving electrostatic, hydrophobic and Van der Waals forces.[12] The AuTSNPs become more stable and less aggregation-prone when they are conjugated with antibody. To determine the quantity of antibody (C2 or C6) required for the stabilization of the nanoplates, various concentrations of antibody were added to aliquots of the AuTSNP

sol. The LSPR spectra of the resulting sols were collected after they were incubated in 0.05 M NaCl for 2 h, which is illustrated in Figure 5.7. Bare AuTSNPs which are incubated in NaCl solution completely aggregate and no LSPR wavelength is detectable. This observation is different from the UV-vis spectrum observed for the bare AuTSNPs incubated in 0.05 M NaCl for 1 h as shown in Figure 5.6 because further aggregation occurred during longer incubation period. For both C2 and C6 antibody functionalization, no aggregation is observed when the concentration of antibody is increased to 5 and 10 µg/mL. To ensure that all nanoplates are conjugated with the antibody and the conjugates are sufficiently stable, 10 µg/mL of antibody (C2 or C6) was used for the conjugation.

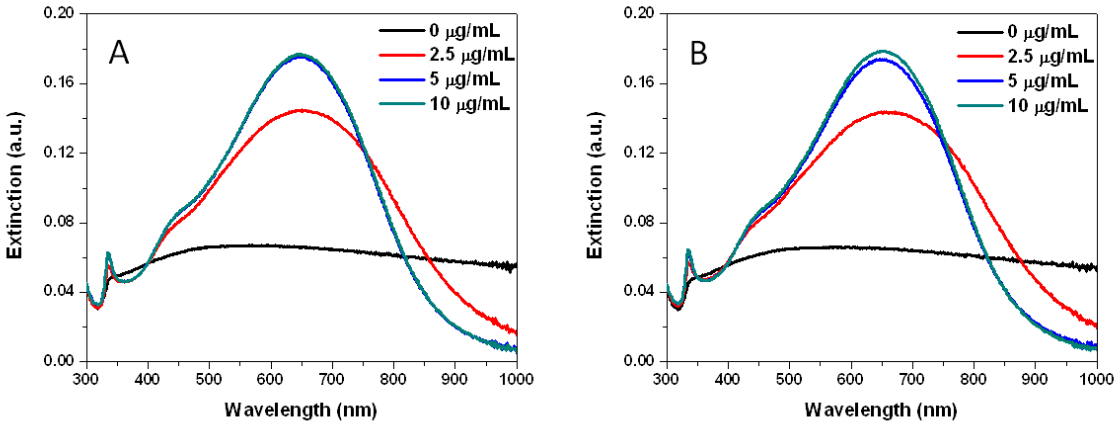

Figure 5.7 UV-vis spectra of C2-AuTSNPs (A) and C6-AuTSNPs (B) conjugates incubated in 0.05 M NaCl for 2 h. The concentrations of C2 or C6 used for the conjugation are given in the legend.

5.4.1.3 Refractive index sensitivity analysis

The refractive index sensitivities of bare AuTSNP, C2-AuTSNP and C6-AuTSNP sols before and after centrifugation were determined using the sucrose method as described in section 4.3.6. The refractive index sensitivities of the samples before centrifugation are shown in Figure 5.8 A. The adsorption of antibody on the surface of nanoplates results in decreased refractive index sensitivities, which is in agreement with the observations for PC and aTnI functionalized nanoplates in Chapter 4. After centrifugation, the sensitivity of AuTSNP sol remains the same while the sensitivities of C2-AuTSNP and C6-AuTSNP sols slightly increase (Figure 5.8 B). When examining

the UV-vis spectra of the samples, no significant shift is observed for all samples after centrifugation (Figure 5.8 C and D), similar to observations for the PC and aTnI functionalized AuTSNPs in Chapter 4. The refractive index sensitivities measured in the experiment were compared with the theoretical values predicted by Miller *et al.*,[13] as illustrated in Figure 5.8 E and F. All samples exhibit sensitivities below the optimum values calculated by Miller's theory, regardless of centrifugation. This suggests that the alternative sol is less sensitive than the one prepared using the method of Aherne *et al.* described in Chapter 4. This can be due to the discrepancies between the two sols in terms of aspect ratio and spectral width under the same condition of maximum LSPR wavelength. As shown earlier in section 5.4.1.1, the nanoplates prepared using the method of Aherne *et al.* exhibit greater aspect ratio and narrower plasmon band than those prepared using the method of Zhang *et al.*. Since large aspect ratios and narrow plasmon bands are considered to contribute to high sensitivity.[11, 14-16] The nanoplates prepared using the method of Aherne *et al.* are expected to be more sensitive than the alternative nanoplates.

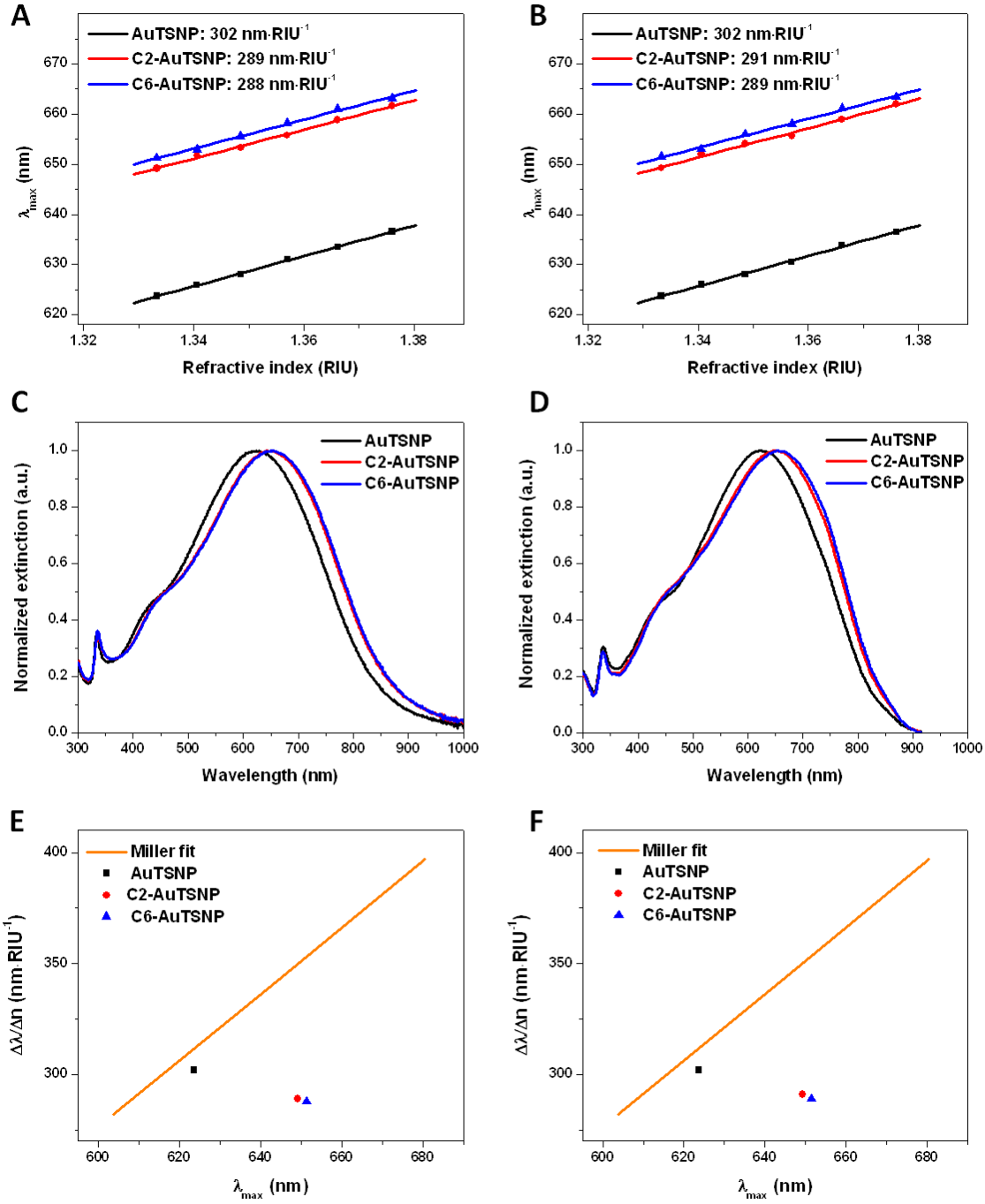

Figure 5.8 (A) Refractive index sensitivities of AuTSNP, C2-AuTSNP and C6-AuTSNP sols before centrifugation; (B) Refractive index sensitivities of the same samples after centrifugation; (C) UV-vis spectra of the samples before centrifugation, the LSPR peak for AuTSNP, C2-AuTSNP and C6-AuTSNP is 624 nm, 649 nm and 651 nm, respectively; (D) UV-vis spectra of the samples after centrifugation, no significant shift is observed for the LSPR peaks; (E) Comparison between the Miller line and

measured sensitivities of as-prepared samples; (F) Comparison between the Miller line and measured sensitivities of centrifuged samples.

5.4.1.4 CRP assay

Two individual sets of aCRP-AuTSNP conjugates including C2-AuTSNPs and C6-AuTSNPs and a 1:1 mixture of the two conjugates were used for the detection of CRP. All assays were monitored for 2 h to investigate the effect of incubation time on the LSPR shift. Figure 5.9 A shows the LSPR peak for the three sols in the presence of 110 mg/L CRP over 2 h. All sols present a similar trend in the peak shift over time where the LSPR peak continues to shift to longer wavelengths during the 2 h incubation. This indicates that the antibody-antigen binding can take more than 2 h to reach equilibrium. In contrast, no significant change is observed for the LSPR peaks of the three sols in the presence of 110 mg/L human IgG which was used as a negative control (Figure 5.9 B). This suggests that no non-specific binding occurred during the assay.

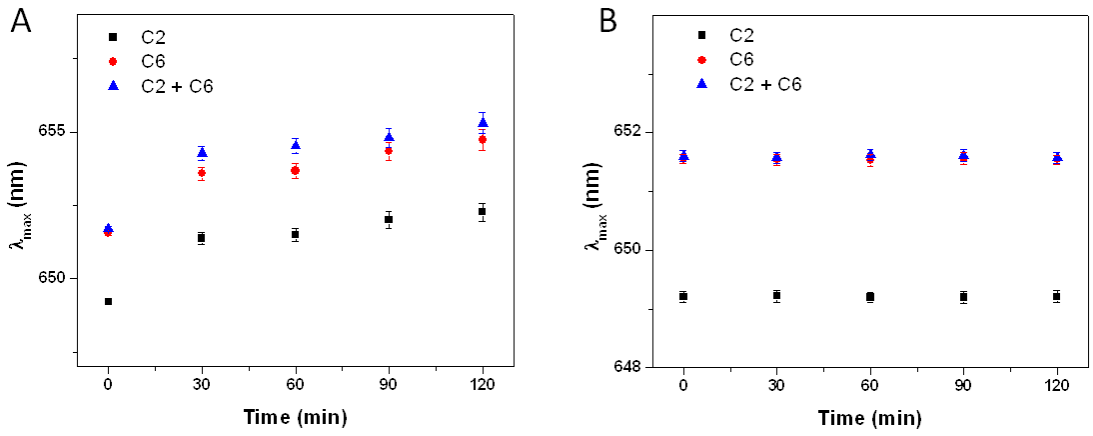

Figure 5.9 LSPR peak of the C2-AuTSNPs (black), C6-AuTSNPs (red) and the mixture of both (blue) in the presence of 110 mg/L CRP (A) and 110 mg/L human IgG (B) over time. (n = 3)

Response curves were constructed by measuring the LSPR wavelength shifts after exposure of the three sols to concentrations of CRP between 0.86 and 110 mg/L for 90 min (Figure 5.10 A). The LSPR shifts observed for the assay using mixed sensors are generally greater than the shifts observed for the assay using either C2-AuTSNPs or C6-AuTSNPs. The LODs for the assays using C2-AuTSNPs, C6-AuTSNPs and the mixture

of both were calculated to be 1.53, 1.62 and 1.29 mg/L, respectively. At the highest concentration of analyte (110 mg/L), all assays appear not to reach saturation. Compared with the commercial hs-CRP assays listed in Table 4.1, the assays using AuTSNPs present much higher LODs. The commercial assays are either based on immunoturbidimetric or immunoluminometric methods. These assays are well-developed and optimized, resulting in much lower LODs than the refractive index sensitivity-based assay. However, the refractive index sensitivity-based assay is a more straightforward method that requires no separation steps when compared with the commercial assays based on immunoluminometric method.

The assays incubated for 90 min were characterized using DLS for particle size analysis (Figure 5.10 B). The hydrodynamic diameter of aCRP-AuTSNPs (either C2-AuTSNPs or C6-AuTSNPs) is measured to be 35 ± 6 nm. On exposure to increasing concentrations of CRP, the sizes of the conjugates increase. Typically, in the presence of 110 mg/L CRP the sizes of the conjugates in direct binding and sandwich assays are measured to be 250 ± 48 nm and 431 ± 69 nm, respectively. This indicates that small aggregates are formed on exposure of aCRP-AuTSNPs to high concentrations of analyte.

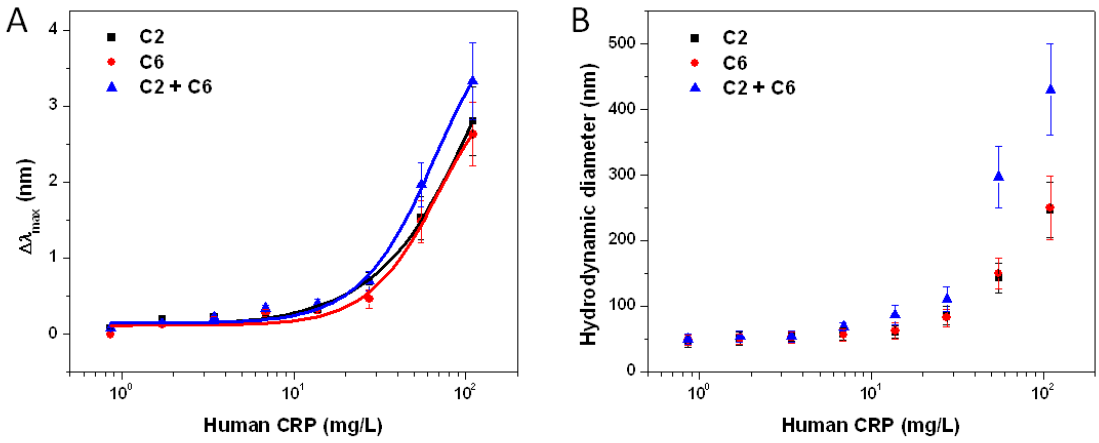

Figure 5.10 (A) Shift in the LSPR peak for C2-AuTSNPs (black), C6-AuTSNPs (red) and the mixture of both as a function of CRP concentration after 90 min incubation; (B) Change in hydrodynamic diameter for the same samples as the concentration of CRP increases. (n = 3)

It is assumed that better assay performance could be achieved if the Kelly particles were used in the same assays. This assumption is mainly based on the comparison of the refractive index sensitivities observed for Kelly and alternative particles. The Kelly particles generally exhibit sensitivities above or near the Miller line whereas the alternative particles have sensitivities below the Miller line.

5.4.2 Aggregation-based IgG assay using AuNPs

The decision to switch from refractive index sensitivity-based CRP assay using AuTSNPs to aggregation-based assay using spherical AgNPs was taken as a result of difficulties encountered with maintaining stability of the antibody-functionalized AuTSNPs. The AuTSNPs were found to aggregate and fall out of the solution after 1 week when conjugated to antibody. While the refractive index sensitivity-based assays have potential for high sensitivity as indicated in the previous chapter for the Kelly particles, it was decided to evaluate the potential performance achievable with the commonly developed aggregation-based assay approach using a simpler nanoparticle model, namely a spherical AuNP.

5.4.2.1 aIgG-AuNP conjugation

The AuNPs used for the aggregation-based assay are spherical with a mean diameter of 13 ± 1 nm (Figure 5.11) and it was decided to use human IgG instead of human CRP. Similar to AuTSNPs, the addition of NaCl can reduce the stability of the nanoparticles in suspension and cause aggregation. As shown in Figure 5.12 A, AuNPs aggregate and completely fall out of the solution when the concentration of NaCl is above 0.04 M. To determine the quantity of antibody to be added, aliquots of AuNP sol were functionalized with various concentrations of aIgG ranging from 5 to 25 µg/mL. The conjugates were then placed in 0.05 M of NaCl solution and incubated for 2 h. Particles incubated in aCRP show increased stability towards increasing ionic strength in the surrounding solution. As shown in Figure 5.12 B, no aggregation is observed for the AuNPs incubated in the solutions containing aIgG ranging between 15 and 25 µg/mL. To make sure the antibody concentation is sufficient but not excessive for conjugation, 20 µg/mL of aIgG was used, since high overloads of protein can cause subsequent leaching of bound material.[17] Upon adding aIgG to the AuNP sol, the LSPR peak

redshifted from 519 nm to 525 nm due to the adsorption of the protein increasing the local refractive index of the nanoparticles.

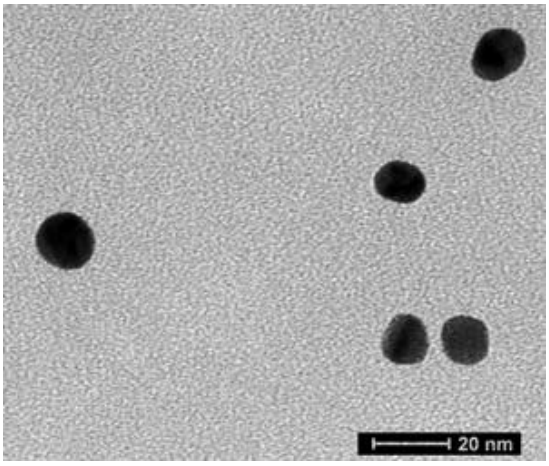

Figure 5.11 TEM images of as-prepared AuNPs

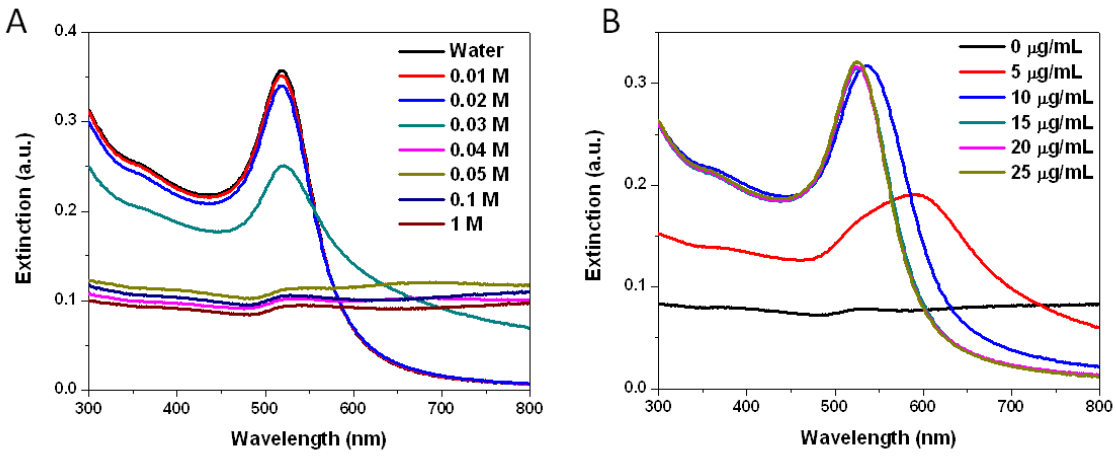

Figure 5.12 (A) UV-vis spectra of AuNPs suspended in different concentrations of NaCl solutions for 2 h. (B) UV-vis spectra of aIgG-AuNP conjugates incubated in 0.05 M NaCl solution for 2 h. The quantities of aIgG used for conjugation are given in the legend.

The addition of human IgG to aIgG-AuNP results in aggregation within 30 min. The UV-vis spectra of solutions containing aIgG-AuNPs and 200 mg/L of IgG at different times during the assay are shown in Figure 5.13 A. The concentration of AuNPs used for the assay was estimated to be 4.3×10^{12} particles/mL (Appendix A). The spectrum

in black is a typical spectrum of aIgG-AuNP sol presenting an LSPR peak at 525 nm. After 30 min incubation, the LSPR peak redshifts to 535 nm accompanied by a decrease in the extinction intensity at the maximum wavelength and an increase in extinction intensity at longer wavelengths. Similar observations have been reported by other groups.[2, 3, 18] The redshift is attributed to the antibody-antigen binding event that increases the local refractive index of the AuNPs and substantially decreases the interparticle distance.[2, 3] The changes in the intensity of the LSPR wavelength result from the formation of AuNP aggregates and their subsequent precipitation.[18] Though the decrease in the intensity of the LSPR peak has been measured and correlated to the analyte concentration,[19, 20] it is found that measuring the change in extinction intensity at longer wavelengths rather than at the maximum wavelength improved the sensitivity.[21] Moreover, measuring the intensity of the LSPR peak maximum to monitor the aggregation of the particles led to a long assay time of about 8 h since the intensity of the plasmon band decreases only when large aggregates are formed.[22] In this experiment, the largest change in extinction during the aggregation of aIgG-AuNP is found to be at 600 nm. Figure 5.13 B shows the extinction intensity at 600 nm for the aIgG-AuNPs incubated with 0 mg/L of IgG, 200 mg/L of aIgG (Fab) and 200 mg/L of IgG over time. It is apparent that no significant change in the extinction intensity at 600 nm for the samples containing 0 mg/L of IgG and 200 mg/L of aIgG (Fab). In the presence of 200 mg/L IgG, the extinction intensity at 600 nm starts to increase within 30 min, peaks at t = 90 min and decreases at t = 120 min. Therefore, all assays were incubated for 90 min to obtain the maximum change in the extinction intensity at 600 nm.

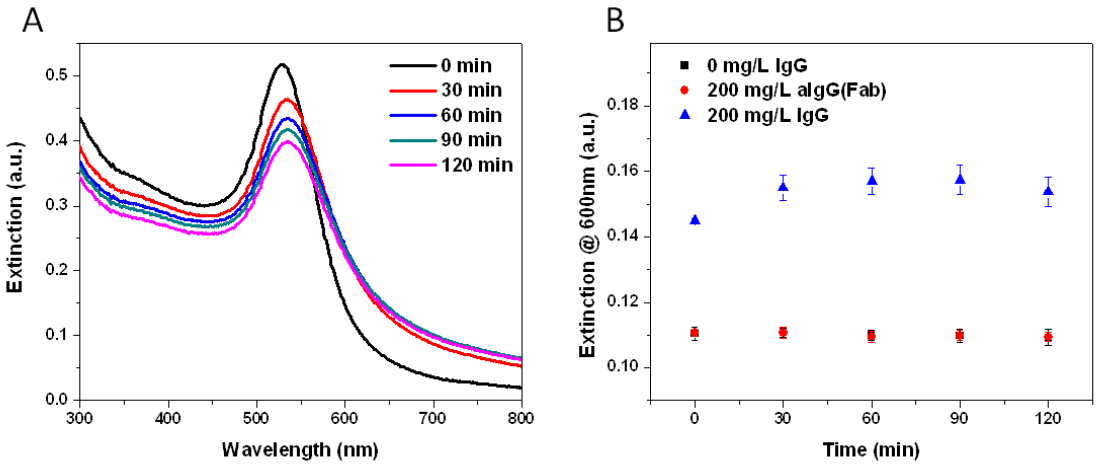

Figure 5.13 (A) UV-vis spectra of aIgG-AuNP conjugates in the presence of 200 mg/L IgG over time; (B) Extinction at 600 nm for aIgG-AuNP conjugates in the presence of 0 mg/L IgG (black), 200 mg/L aIgG(Fab) (red) and 200 mg/L IgG (blue) over time. (n = 3)

A response curve was constructed by plotting the change in extinction intensity at 600 nm against human IgG concentrations ranged from 0.78 to 400 mg/L (Figure 5.14 A). The LOD was determined to be 1.59 mg/L of IgG, which shows a greater sensitivity than a similar assay reported by Cao *et al.* who used less concentrated antibody-AuNP conjugates for IgG detection.[23] The aggregation rate depends mostly on the collision frequency of the particles, which is directly related to the density of AuNPs in the analyte solution. As expected, the extinction change is larger at a higher concentration of AuNPs. Though the fitted assay curve is not a complete sigmoid curve, it indicates the working range of the assay is approximately two orders of magnitude. When compared with a commercial human IgG assay, the LOD of this aggregation-based assay is much higher than that of Abcam's ELISA kit which has an LOD of 0.15 µg/L. This is due to the fact that the commercial assay has been well-developed and optimized whereas improvements are required for the aggregation-based assay. The required improvements involve the optimization of AuNP concentration, pH and temperature.

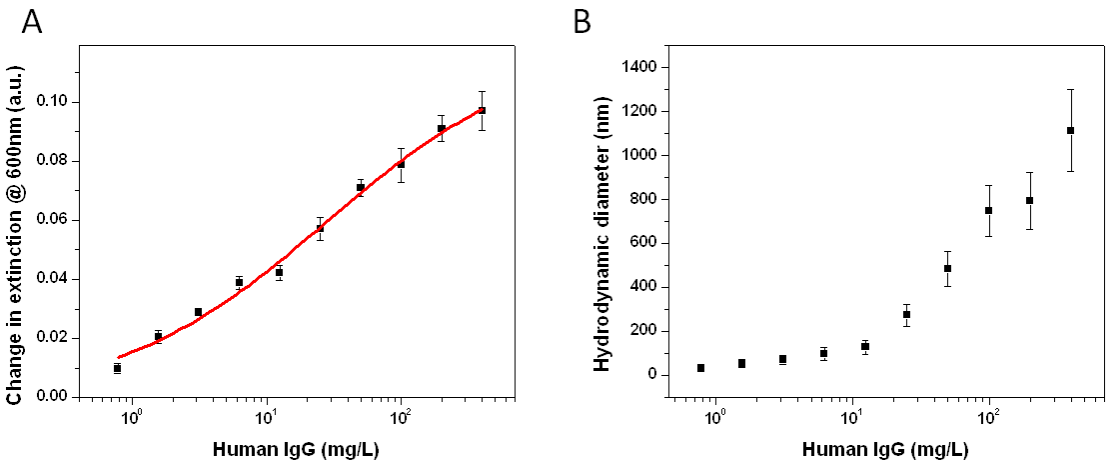

Figure 5.14 (A) Extinction change at 600 nm against the concentration of human IgG (n = 3); (B) Hydrodynamic diameter of the aIgG-AuNP conjugates as the concentration of human IgG increases. All assays were incubated for 90 min.

The sizes of the aIgG-AuNP conjugates used for the assay were characterized with DLS. As shown in Figure 5.14 B, the size of the conjugates increases with IgG concentration. The mean size of aIgG-AuNP conjugates is measured to be 28 ± 8 nm. Upon exposing to 400 mg/L of IgG, the mean size of the conjugates increases to 1115 ± 187 nm, suggesting that a high degree of aggregation has occurred. An example of the aggregation progress over time is given in Figure 5.15. Figure 5.15 A shows the TEM image of aIgG-AuNP conjugates prior to the addition of IgG. Following the addition of 200 mg/L IgG, increased density of nanoparticles is observed at t = 30 min, in accompany with the formation of islands of small aggregates (Figure 5.15 B). At t = 90 min, abundant nanoparticles are assembled forming a microscale structure (Figure 5.15 C).

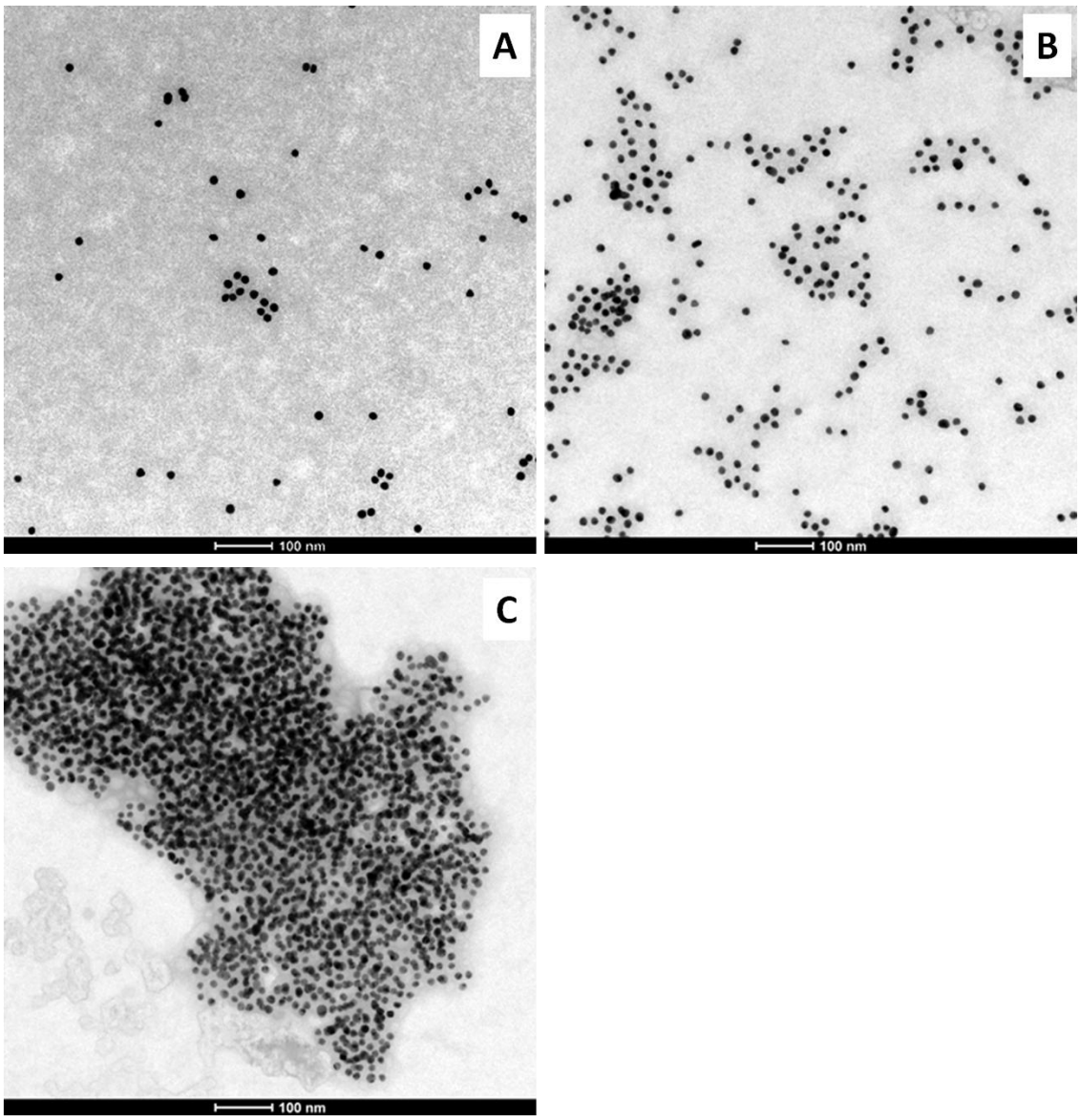

Figure 5.15 TEM images during the aggregation process of the AuNPs in the presence of 200 mg/L IgG at (A) t = 0 min, (B) t = 30 min and (C) t = 90 min.

In this work, both refractive index sensitivity-based assay and aggregation-based assay belong to the colorimetric detection. To date, spherical AuNPs have been the most commonly used particles for the aggregation-based assays in relation to plasmonic sensing. However, only a narrow color change of the sol is observed when AuNPs are used for the colorimetric detection. On the contrary, the spectral wavelength of AuTSNPs can be tuned through the entire visible spectrum, rendering them more possibility as a colorimetric sensor. In addition to the refractive index sensitivity-based assays using nanoparticle ensembles, single nanoparticle sensing has been developed for

the assays.[24, 25] Therefore, refractive index sensitivity-based assays exhibit more potential than aggregation-based assays.

5.4.3 AuTSNP-enhanced SPR detection of human IgG

As discussed in Chapter 2, there is a growing interest in the potential of plasmonic nanoparticles to enhance conventional label-free SPR assays. This section acts as a bridge between the purely solution-based assays reported in Chapter 4 and the earlier part of this Chapter and the final results chapter which deals with solid-phase MEF assays. This section also provides the opportunity to explore the use of the alternative AuTSNPs for another assay approach, given that their performance was not very satisfactory when used in refractive index sensitivity-based assays.

In order to carry out this assay, an aliquot of AuTSNP sol was functionalized with 10 µg/mL of polyclonal anti-human IgG (aIgG), followed by the addition of BSA (5 µg/mL) to block the free sites on the nanoplate surface. As shown in Figure 5.16, the LSPR peak redshifts from 632 nm to 658 nm due to the spontaneous adsorption of protein molecules to the nanoplate surface. To evaluate the effect of AuTSNPs on SPR-based biosensing, an immunoassay was carried out using human IgG model. In a typical assay, protein A was first immobilized on the gold surface of a sensor chip, followed by a blocking step with BSA. Various concentrations of human IgG were injected and captured by protein A. Next, the aIgG-AuTSNP sol was injected and bound to the protein A/IgG layer on the gold surface. The concentration of aIgG-AuTSNP conjugates was estimated to be 3×10^{11} particles/mL. A control experiment was performed by simply introducing free aIgG (1 µg/ml) to the SPR system under the same experimental conditions. The concentration of free aIgG used in the control assay was determined by assuming that a monolayer of antibody remained after removing the unbound aIgG from aIgG-AuTSNP sol via centrifugation, which was ~ 1 µg/mL (Appendix B).

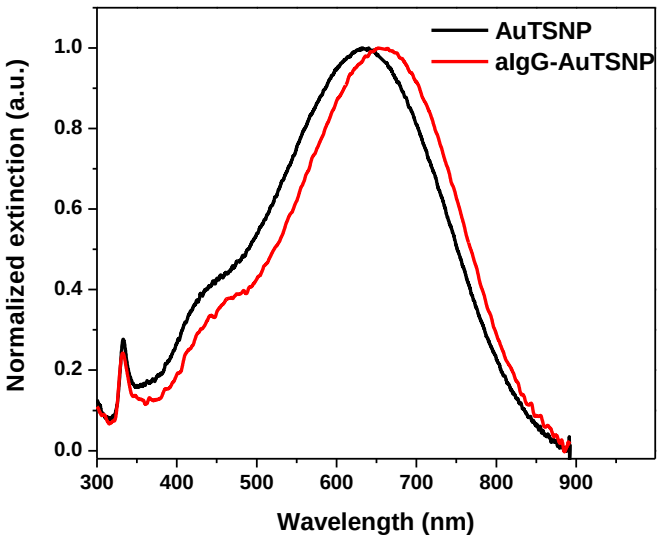

Figure 5.16 UV-vis spectra of AuTSNP and aIgG-AuTSNP sols.

An example of the obtained SPR response curves is given in Figure 5.17, showing the binding of free aIgG (black) and aIgG-AuTSNPs (red) to IgG immobilized on the gold chip. The concentration of IgG injected to the sensing system is 10 µg/mL. The binding response measured in response units (RU) is increased by ~ 11-fold when using aIgG-AuTSNP. Figure 5.18 shows the plottings of SPR response against IgG concentration for AuTSNP-enhanced (A) and control (B) assays. When no IgG is injected to the SPR system, binding responses of 3.4 RU and 145.9 RU are observed for the control and AuTSNP-enhanced assay, respectively. This indicates that non-specific binding has occurred. It is presumed that a higher concentration of BSA or a longer flow time could be used to minimize the non-specific binding. In general, the binding responses of the assay using aIgG-AuTSNPs are much higher than those of the control assay. The mechanism behind the nanoparticle-enhanced SPR detection is still under investigation. Three possible factors have been suggested, including (i) an increase in the surface mass, (ii) an increase in the refractive index of the analyte, and (iii) coupling between the LSPR of the nanoparticles and the propagating SPR of the gold film.[5, 26, 27] Nevertheless, AuTSNPs provide a potential approach to efficiently enhancing SPR-based biosensing.

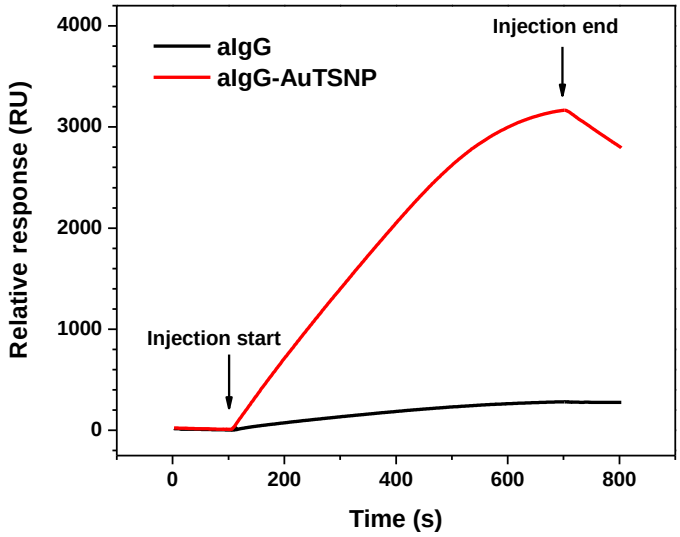

Figure 5.17 SPR responses of the binding of aIgG (black) and aIgG-AuTSNPs (red) onto the protein A/IgG layers formed on the gold surface. The concentration of IgG used to bind protein A is 10 µg/mL.

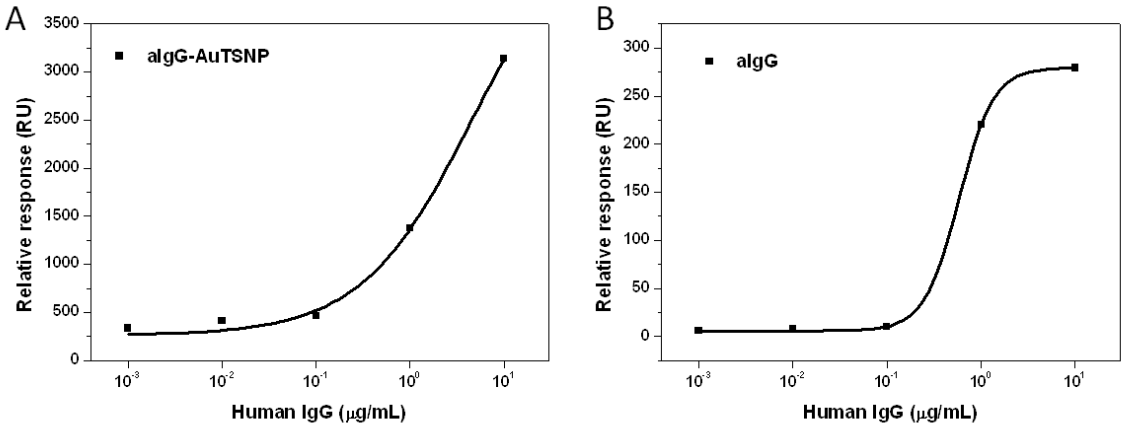

Figure 5.18 SPR responses at different IgG concentrations using (A) aIgG-AuTSNP and (B) free aIgG.

5.5 Conclusions

In this chapter, homogenous assays were developed using different nanoparticles. The first set of assays involves LSPR refractive index sensitivity based CRP assay using AuTSNPs. AuTSNPs were derived from TSNPs that were prepared with a different method from the one in Chapter 4. The refractive index sensitivities of as-prepared AuTSNPs and aCRP-AuTSNPs before and after centrifugation were determined using sucrose method. The refractive index sensitivity of AuTSNP decreased after antibody functionalization. As-prepared AuTSNPs exhibited no change in the refractive index sensitivity after centrifugation while a slight increase was observed for aCRP-AuTSNPs after centrifugation. The measured sensitivities of all samples were below the optimum values predicted by Miller *et al.*, indicating the AuTSNPs prepared using H_2O_2 and $NaBH_4$ do not exhibit sensitivities as high as the ones prepared using the seed-mediated method in Chapter 4. The lowest LOD (1.29 mg/L) was observed for the assay using a 1:1 mixture of two sensors (C2-AuTSNP and C6-AuTSNP). However, this LOD is much higher than those of the commercial hs-CRP assays as listed in Table 4.1. These commercial assays have been well-developed and optimized whereas improvements are needed for the refractive index sensitivity-based assay by optimizing the AuTSNP concentration, pH and temperature. Additionally, the triangular nanoplates with high refractive index sensitivities are required for the optimization of the assay. All assays were characterized using DLS for size analysis. It is found that the size of aCRP-AuTSNPs increases with CRP concentration, suggesting that larger aggregates are formed as more analytes are added.

The second set of assay involves aggregation-based IgG assay using spherical AuNPs. AuNPs were conjugated with aIgG. The extinction of aIgG-AuNP conjugates at 600 nm was measured when exposing to various concentrations of IgG. The LOD of the assay was 1.59 mg/L, which is lower than that of a similar assay reported by Cao *et al.*.[23] The assay was characterized with DLS and TEM. The third assay set involves nanoparticle-enhanced SPR detection of human IgG using AuTSNPs. The SPR responses observed for the assay using aIgG-AuTSNPs were much greater than those for assay using free aIgG. However, non-specific binding was noted and optimization is needed to minimize it. Though more study needs to be carried out for the AuTSNP-enhanced SPR assay, nanoparticles indeed show great potential to enhance the SPR detection. For instance,

the sensitivity of an SPR biosensor for the detection of IgG was improved by 23-fold when gold nanorods were integrated in the detection system.[5]

References

1. N. T. K. Thanh and Z. Rosenzweig, Analytical Chemistry **74** (7), 1624-1628 (2002).
2. P. Englebienne, Journal of Materials Chemistry **9** (5), 1043-1054 (1999).
3. J. J. Storhoff, A. A. Lazarides, R. C. Mucic, C. A. Mirkin, R. L. Letsinger and G. C. Schatz, Journal of the American Chemical Society **122** (19), 4640-4650 (2000).
4. L. A. Dykman, V. A. Bogatyrev, B. N. Khlebtsov and N. G. Khlebtsov, Analytical Biochemistry **341** (1), 16-21 (2005).
5. W.-C. Law, K.-T. Yong, A. Baev, R. Hu and P. N. Prasad, Opt. Express **17** (21), 19041-19046 (2009).
6. Q. Zhang, N. Li, J. Goebl, Z. Lu and Y. Yin, Journal of the American Chemical Society **133** (46), 18931-18939 (2011).
7. D. Aherne, D. E. Charles, M. E. Brennan-Fournet, J. M. Kelly and Y. K. Gun'ko, Langmuir **25** (17), 10165-10173 (2009).
8. G. Frens, Nature-Physical Science **241** (105), 20-22 (1973).
9. K. C. Grabar, R. G. Freeman, M. B. Hommer and M. J. Natan, Analytical Chemistry **67** (4), 735-743 (1995).
10. N. Shirtcliffe, U. Nickel and S. Schneider, Journal of Colloid and Interface Science **211** (1), 122-129 (1999).
11. D. E. Charles, D. Aherne, M. Gara, D. M. Ledwith, Y. K. Gun'ko, J. M. Kelly, W. J. Blau and M. E. Brennan-Fournet, ACS Nano **4** (1), 55-64 (2009).
12. G. T. Hermanson, *Bioconjugate Techniques*. (Academic Press, 2008).
13. M. M. Miller and A. A. Lazarides, The Journal of Physical Chemistry B **109** (46), 21556-21565 (2005).
14. L. J. Sherry, S.-H. Chang, G. C. Schatz, R. P. Van Duyne, B. J. Wiley and Y. Xia, Nano Letters **5** (10), 2034-2038 (2005).
15. E. M. Hicks, S. Zou, G. C. Schatz, K. G. Spears, R. P. Van Duyne, L. Gunnarsson, T. Rindzevicius, B. Kasemo and M. Käll, Nano Letters **5** (6), 1065-1070 (2005).
16. D. Charles, P. Fournet, S. Cunningham, D. Ledwith, J. M. Kelly, W. Blau and M. B. Fournet, 70322G-70322G (2008).
17. M. Horisberger and M. F. Clerc, Histochemistry **82** (3), 219-223 (1985).

18. V. Chegel, O. Rachkov, A. Lopatynskyi, S. Ishihara, I. Yanchuk, Y. Nemoto, J. P. Hill and K. Ariga, The Journal of Physical Chemistry C **116** (4), 2683-2690 (2011).
19. J. H. W. Leuvering, P. J. H. M. Thal, M. Van der Waart and A. H. W. M. Schuurs, Journal of Immunological Methods **45** (2), 183-194 (1981).
20. J. H. W. Leuvering, P. J. H. M. Thal and A. H. W. M. Schuurs, Journal of Immunological Methods **62** (2), 175-184 (1983).
21. P. Englebienne, Analyst **123** (7), 1599-1603 (1998).
22. H. Otsuka, Y. Akiyama, Y. Nagasaki and K. Kataoka, Journal of the American Chemical Society **123** (34), 8226-8230 (2001).
23. Q. Cao, H. Yuan and R. Cai, J. Wuhan Univ. Technol.-Mat. Sci. Edit. **24** (5), 772-775 (2008).
24. K. Mayer, M. , F. Hao, S. Lee, P. Nordlander and J. Hafner, H. , Nanotechnology **21** (25), 255503 (2010).
25. A. Haes, D. Stuart, S. Nie and R. Van Duyne, J Fluoresc **14** (4), 355-367 (2004).
26. L. He, M. D. Musick, S. R. Nicewarner, F. G. Salinas, S. J. Benkovic, M. J. Natan and C. D. Keating, Journal of the American Chemical Society **122** (38), 9071-9077 (2000).
27. D. Mustafa, T. Yang, Z. Xuan, S. Chen, H. Tu and A. Zhang, Plasmonics **5** (3), 221-231 (2010).

Chapter 6

Metal-enhanced fluorescence (MEF) -based immunoassays

6.1 Introduction

This chapter focuses on the investigation and development of fluorescence-based immunoassays enhanced by noble metal nanoparticles. In this work, two distinct types of nanoparticles including large spherical silver nanoparticles (AgNPs) and AuTSNPs have been investigated to further understand the underlying parameters required for optimal MEF. The enhancement effect of different dyes Cy5 and $[Ru(bpy)_2(pic)]^{2+}$ were also investigated. Silver nanoparticles can be prone to oxidation and restructuring, therefore gold coating of the large AgNPs was performed and the effect of the gold-coated AgNPs on the fluorescence of Cy5 was examined. An initial MEF assay was carried out using a human IgG model system. The assay format was further used to develop a fluorescence-based immunoassay for the detection of CRP.

6.2 Background and overview of the MEF assay

Recently noble metal nanoparticles have been incorporated into fluorescence-based assays, resulting in immunoassays with amplified fluorescence signals and increased sensitivities.[1-4] The increased fluorescence intensity and improved performance of these assays can be attributed to the phenomenon of MEF. MEF can arise from both enhanced excitation and emission processes. Nanoscale metals can interact with fluorophores through the presence of their local electromagnetic fields and through coupling of their plasmonic scattering modes to increase their fluorescence intensity.[5-7] The factors influencing fluorescence enhancement are complex and include parameters such as the spectral location of the nanostructure plasmon resonance, the intensity of its spectral scattering and absorption components, electric field enhancement, the overlap with the fluorophore excitation and emission spectra, the distance between the metal particle and the dye and the intrinsic quantum efficiency of the fluorophore.

The relative contributions of the factors above differ across several studies in the literature. A significantly greater influence on MEF from plasmonic scattering components over electric field contributions has been reported by many authors. [8, 9] Zhang *et al.* confirmed that the wavelength dependence of MEF for the solvent sensitive dye, Prodan, correlated more strongly with the scattering component of the extinction with a poor correlation observed with the wavelength dependence of the electric field.[10] Controlling and optimizing the relative contributions of these often competitive properties provides a significant challenge to harnessing the potential of MEF. Furthermore, strategies towards the fabrication of substrates, which overcome the negative effects of ensemble averaging and provide statistically representative ultrabright fluorescence signals are required, particularly for biological assay applications. Towards this goal, planar substrates with highly ordered 100-nm gold triangular nanoprism patterns have been demonstrated by Pompa *et al.* to produce a 33-fold enhancement for CdSe/ZnS semiconductor nanocrystals.[11]

In this work, a model immunoassay involving polyclonal anti-human IgG antibodies and human IgG was firstly used to investigate the enhancement effect of noble metal nanoparticles on the fluorescence-based assay. Following that, the MEF assay format was extended to the detection of human CRP. Both MEF immunoassays were performed in a sandwich format on the nanoparticle-modified substrates. A schematic diagram of the MEF assay setup is shown in Figure 6.1. The nanoparticle-modified substrate was prepared by depositing the nanoparticles onto a polyelectrolyte (PEL)-coated substrate.[12] A sandwich immunoassay was carried out on the modified substrate, where the analyte (i.e. IgG or CRP) was sandwiched between the capture antibody and the fluorophore-labeled antibody (i.e. detection antibody). The fluorescence signal of the immunoassay was amplified due to the phenomenon of MEF by using the nanoparticle-modified substrate. Consequently, the sensitivity and LOD of the assay was improved when compared to the control assay without nanoparticles.

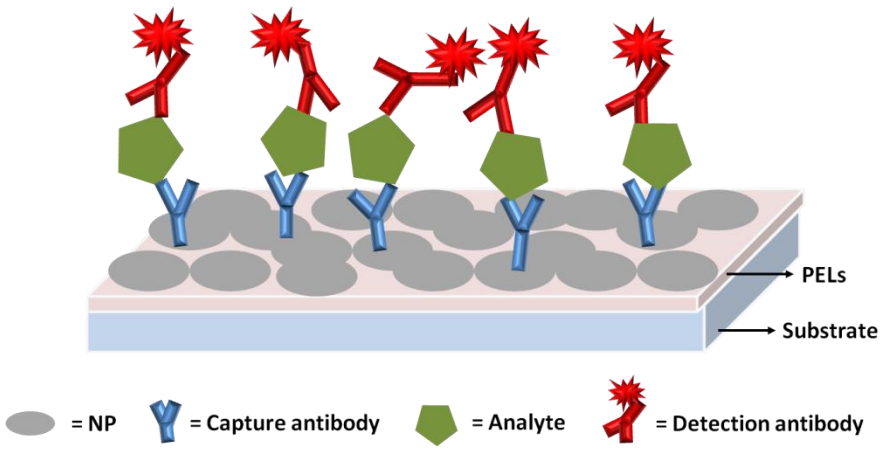

Figure 6.1 Schematic diagram of MEF immunoassay.

6.3 Experimental methods

6.3.1 Materials

$AgNO_3$ (≥ 99.9%), TSC, $NaBH_4$, H_2O_2 (30 wt. %), aniline (≥99.5%), AA, $HAuCl_4$ (≥ 99.9%), NaCl, sodium bicarbonate ($NaHCO_3$), sodium carbonate (Na_2CO_3), poly(ethyleneimine) (PEI, average M_w ~ 750,000), poly(allylamine) hydrochloride (PAH, average M_w ~ 58,000), poly (sodium 4-styrene sulfonate) (PSS, average M_w ~ 70,000), hydrochloric acid (HCl, 37%), sodium hydroxide (NaOH), PBS, 2-(*N*-Morpholino)ethanesulfonic acid (MES), Tween 20, potassium cyanide (KCN) and *N*,*N*-dimethylformamide (DMF, ≥99.8%) were purchased from Sigma-Aldrich and were used as received.

Goat anti-human IgG polyclonal antibody (Fab specific) and human IgG were purchased from Sigma-Aldrich. Alexa Fluor 647 labeled goat anti-human IgG polyclonal antibody (H+L) was purchased from Invitrogen. The dye-to-protein molar ratio was 5. Mouse anti-human CRP monoclonal antibody C2 was purchased from HyTest (Turku, Finland). Human CRP was purchased from Millipore (California, USA). DY647-labeled mouse anti-human CRP monoclonal antibody C6 was purchased from Exbio Praha (Vestec, Czech Republic). The dye-to-protein molar ratio was 4.5. Bovine serum albumin (IgG-free) was purchased from Jackson ImmunoResearch (Pennsylvania, USA). Cy5 mono NHS ester was purchased from GE Healthcare (Buckinghamshire, UK). DY647 NHS ester was purchased from Dyomics (Jena, Germany). $[Ru(bpy)_2(pic)]^{2+}$ was obtained from the group of Prof. Tia Keyes in School of

Chemical Sciences. Black 96-well microtiter plates with clear bottom were purchased from Greiner Bio-one (Solingen, Germany). Nunc Maxisorp 96-well microtiter plates were purchased from Fisher Scientific (Roskilde, Denmark). Water purified by a Milli-Q Academic system (Millipore, USA) to a resistivity of 18.2 MΩ cm^{-1} was used throughout.

6.3.2 Synthesis of nanoparticles

6.3.2.1 Synthesis of AuTSNPs

AuTSNPs were prepared using the method described in section 5.3.2.1.

6.3.2.2 Synthesis of spherical silver nanoparticles

Large spherical silver nanoparticles (AgNPs) were prepared by the reduction of $AgNO_3$ with TSC in the presence of aniline.[13] Typically, $AgNO_3$ (0.02 M, 4 mL) and aniline (7.3 µL) were added to 108 mL of water with vigorous stirring. The solution was heated to reflux and TSC (1 wt. %, 8 mL) was added. The stirring was stopped after 10 seconds and the solution was refluxed for 30 min during which the solution color changed from clear to milky grey. The obtained AgNP suspension was doubly concentrated by 5 min centrifugation at 15,616 × g and re-dispersion in water. The final suspension was kept at 4 ℃ before use.

6.3.2.3 Synthesis of gold-coated AgNPs

In a typical synthesis, a batch of AgNPs was prepared using the method stated in section 6.3.2.2 without the concentration process. The colloid was then split into four aliquots of identical volume, with each aliquot containing 1.6×10^{-5} mol of $AgNO_3$. AA (10 mM, 1.6 mL) was added to one aliquot with vigorous stirring, followed by gradually adding the appropriate volume of $HAuCl_4$ solution (0.5 mM) corresponding to the desired Au/Ag ratio. The obtained samples were then doubly concentrated by centrifugation as described above in section 6.3.2.2. The final colloids were kept at 4 ℃ before use.

6.3.3 Synthesis of dye-PAH conjugates

Different NHS ester-activated fluorescence dyes including Cy5, DY647 and $[Ru(bpy)_2(pic)]^{2+}$ were used in this work. The conjugation of each dye with PAH was

carried out using the same procedure. The dye-to-PAH ratio was maintained at 1 to 40. Taking Cy5 as an example, the Cy5-PAH conjugate was synthesized by mixing Cy5-NHS ester (1.5 mg) dissolved in DMF (50 µL) and PAH (4.76 mg) dissolved in $NaHCO_3/Na_2CO_3$ buffer (4.7 mL, 0.1 M, pH 8.5) for four hours. The free dye was removed by filtration using a Vivaspin 6 centrifugal column with a 10,000 MWCO. The conjugate solution was stored at 4 ℃ before use.

6.3.4 Layer-by-layer assembly of PEL multilayer films

Black 96- well microtiter plates with transparent polystyrene bottoms were used as an experimental assay platform. To immobilize AgNPs onto the substrate, five layers of PEL were firstly constructed using the layer-by-layer (LbL) deposition technique.[12] Five is the minimum number of preliminary PEL layers required to ensure the complete coverage of PEL on the substrate. PEI, PAH and PSS solutions at 2 mg/mL were prepared by dissolving individual PEL in an aqueous solution containing 0.5 M NaCl. All PEL solutions were adjusted to pH 7 using NaOH or HCl. Prior to PEL modification, a plate was oxygen plasma-treated for 5 min under vacuum in a Harrick PDC-200 plasma chamber. PEL layers were deposited onto the plate substrate by incubating 150 µL aliquots of PEL solutions in individual wells for 15 minutes, followed by three washes with water. The deposition sequence of PEL layers was PEI/PSS/PAH/PSS /PAH with the uppermost layer providing a positively-charged surface for subsequent assembly of a nanoparticle film.

6.3.5 Assembly of nanoparticle film

150 µL aliquots of nanoparticle solution were added to the PEL-modified wells of the microtiter plate. The plate was sealed with Parafilm and incubated overnight at room temperature in the dark. After three washes with water, extinction spectra of the nanoparticle films were obtained with 150 µL of water in each well.

6.3.6 Assembly of PEL multilayer spacers and deposition of dye-PAH conjugate

To create different thicknesses of spacers between the nanoparticle film and fluorescence dye, a series of $(PAH/PSS)_n$ bilayers were assembled by alternately depositing PAH and PSS onto the nanoparticle film using the same approach as

described in section 6.3.4. The number of bilayers (*n*) ranged from 0 to 7. After constructing PEL multilayer spacers, 150 µL aliquots of dye-PAH conjugate solution were added to the wells with an incubation time of 15 minutes, followed by thorough washes with water. A set of control wells was prepared by directly depositing dye-PAH conjugate onto the PEL-modified substrate in the absence of nanoparticles.

6.3.7 IgG assay[2]

The MEF human IgG immunoassay was carried out in a sandwich assay format with four replicates. In a typical experiment, a Greiner 96-well microtiter plate with a transparent polystyrene bottom was coated with AgNPs, and a Nunc Maxisorp 96-well black microtiter plate was used for the control assay without AgNPs. In the case of the plasmon-enhanced immunoassay, AgNPs were firstly deposited onto the PEL-modified wells of the Greiner plate using the method described in section 6.3.5. Goat anti-human IgG polyclonal antibody (Fab specific) (5 µg/mL, 100µL) was then added to each well and the plate was incubated for 1 hour at 37 ℃. For the control assay without AgNPs, the plate was incubated overnight at 4 ℃ after adding capture antibody (5 µg/mL, 100µL) to each well. The two plates were washed three times with PBS and three times with PBS solution containing 0.05 (v/v) % Tween 20 (PBST) before blocking each well with 300 µL of 1 (w/v) % BSA in PBS for 1 hour at 37 ℃. The wash cycle was repeated. Next, 100 µL aliquots of human IgG in 0.1 (w/v) % BSA ranged from 0.1 to 10^5 µg/L were added to appropriate wells and the plates were incubated for 1 hour at 37 ℃. Following the wash cycle, 100 µL aliquots of Alexa Fluor 647-labeled polyclonal anti-human IgG (H+L) (0.025 mg/mL) were added to each well and the plates were incubated for 1 hour at 37 ℃ in the dark. The plates were then washed one more time and 100 µL aliquots of PBS were added to each well before the measurements.

6.3.8 CRP assay

Solid phase sandwich assays based on MEF were carried out for the detection of human CRP. A series of CRP dilutions ranging from 1.5×10^{-4} to 10 mg/L were assayed in four replicates. Typically, a Greiner 96-well microtiter plate with transparent polystyrene substrate was coated with AgNPs, and a Nunc Maxisorp 96-well black microtiter plate was used for the control assay in the absence of AgNPs. In the case of the MEF immunoassay, AgNPs were firstly deposited onto the PEL-modified wells of

the Greiner plate using the method described in section 6.3.5. Mouse anti-human CRP monoclonal antibody C2 (5 µg/mL, 100µL) was added to each well and the plate was incubated for 1 hour at 37 ℃. In the case of control assay without AgNPs, the plate was incubated overnight at 4 ℃ after adding capture antibody (5 µg/mL, 100µL) to each well. The plates were washed three times with PBS and three times with PBST before blocking each well with 300 µL of 1 (w/v) % BSA in PBS for 1 hour at 37 ℃. The wash cycle was repeated. Next, 100 µL aliquots of human CRP in 0.1 (w/v) % BSA ranged from 1.5×10^{-4} to 10 mg/L were added to appropriate wells and the plates were incubated for 1 hour at 37 ℃. Following the wash cycle, 100 µL aliquots of DY647-labeled mouse monoclonal anti-human CRP C6 (0.02 mg/mL) were added to each well and the plates were incubated for 1 hour at 37 ℃ in the dark. The plates were then washed one more time and 100 µL aliquots of PBS were added to each well before the measurements.

6.3.9 KCN test

Following the measurements of the CRP assay plate with AgNPs, 10 µL aliquots of PBS were removed from one replicate of the assay. Aliquots of KCN (1 M, 10 µL) were then added to each well in this replicate. After 45 min incubation, the wells were measured using the plate reader.

6.3.10 Characterization techniques

6.3.10.1 UV-vis and fluorescence spectroscopy

Ultraviolet-visible (UV-vis) extinction measurements were collected using either a Cary 50 (Varian) or a microplate reader (Tecan Infinite 200). All fluorescence measurements were collected using the Tecan plate reader.

6.3.10.2 TEM

TEM of the nanoparticles was performed with a Tecnai G^2 20 twin microscope (FEI, USA), operating at an acceleration voltage of 200 kV. Typically, an aliquot of the as-prepared nanoparticle sample was three-fold concentrated by 5 min centrifugation at 16,100 × g and room temperature. A 10 µL drop of concentrated sample in water was placed onto a 300 mesh copper grid coated with Formvar/carbon (Agar Scientific, UK)

and dried in air for one hour. The excess solution was wicked away and the sample was further dried overnight prior to imaging. ImageJ was used for measuring the dimensions of nanoparticles.

6.3.10.3 AFM

AFM was performed to analyze the surface profile of the nanoparticle-coated substrates using a Veeco BioScope II. In a typical sample preparation, a glass slide (Menzel-Gläser, Germany) was firstly cleaned by sequential sonication for 30 min in 1(v/v) % detergent, water and absolute ethanol. The glass slide was dried with nitrogen gas and oxygen plasma treated for 5 min. It was sequentially immersed in PEL solutions (PEI/PSS/PAH/PSS/PAH) with an incubation time of 15 minutes. The glass slide was washed with water and dried using a slide centrifuge between immersions. A 1cm × 1 cm gene frame (Thermo Scientific ABgene) was adhered to the PEL-coated glass slide and a 150 µL aliquot of nanoparticle solution was added to the substrate. Following an overnight incubation at room temperature in the dark, the nanoparticle solution and the frame were removed. The slide was washed with water and dried thoroughly with nitrogen gas before the analysis. The AFM measurements were performed in tapping mode using silicon probes (NanoWorld AG). The obtained images were analyzed using ImageJ software.

6.4 Results and discussion

6.4.1 Nanoparticle deposition and characterization

Two distinct nanoparticle systems were selected, large spherical AgNPs and AuTSNPs, to investigate and compare their ability to enhance the fluorescence of Cy5, and to illustrate the relative enhancement obtained as a function of the nanoparticle extinction contributions, namely the absorption and scattering components of the nanoparticles.

In this work, AgNP and AuTSNP sols were individually used to coat the substrates. Nanoparticle-coated substrates were conveniently prepared by depositing the nanoparticles on PEL-modified polystyrene substrates (Figure 6.2).[2] PELs are polymers with ionized groups. In aqueous solutions such as water, these groups dissociate, leading to charged polymers. The PEL multilayer film is assembled onto the substrate through the alternate adsorption of cationic (PEI and PAH) and anionic (PSS) polymers

from solution. This sequential self-assembly method is known as layer-by-layer (LbL) deposition technique. As the film is assembled layer by layer, the use of PELs allows control over the layer thicknesses at the nanometer scale. Two possible interactions are involved in the adsorption of the nanoparticles to the substrate. One is the electrostatic interaction between the negatively charged nanoparticles and the positively charged PAH layer, the other is via semi-covalent bonding between the metal and the amine group in PAH.

Figure 6.2 Schematic for the stepwise preparation of the nanoparticle-coated substrates.

The UV-Vis spectra of the two nanoparticle samples before and after deposition are shown in Figure 6.3. The AgNP sol displayed a plasmon band at 435 nm and a shoulder at 630 nm. The LSPR band at 435 nm corresponds to the quadrupole peak and the shoulder corresponds to the dipole peak of the AgNP sol. Following deposition the plasmon band was observed to shift to 455 nm. The AuTSNP sol exhibited a plasmon band at 695 nm which was broadened and redshifted to 800 nm upon immobilizing the nanoplates on the substrate. This shift in the LSPR band can be attributed to the change in refractive index and could also possibly be due in part to near field coupling.[14] The LSPR of high aspect ratio TSNPs has been shown to be very sensitive to changes in refractive index due to the strong localized electromagnetic field at the particles surface and can account for the large shift observed.[15, 16] A similar behavior has been observed by Jensen *et al.* using a DDA calculation and experiment, whereby they found that the extinction maxima of silver truncated tetrahedrons and silver oblate ellipsoids shifted to longer wavelengths after immobilization on a substrate.[17] In our work, a standard deviation of 1% and 3% was observed for the extinction maxima of the AgNP films and the AuTSNP films respectively (Figure 6.3), confirming the high reproducibility of the nanoparticle deposition.

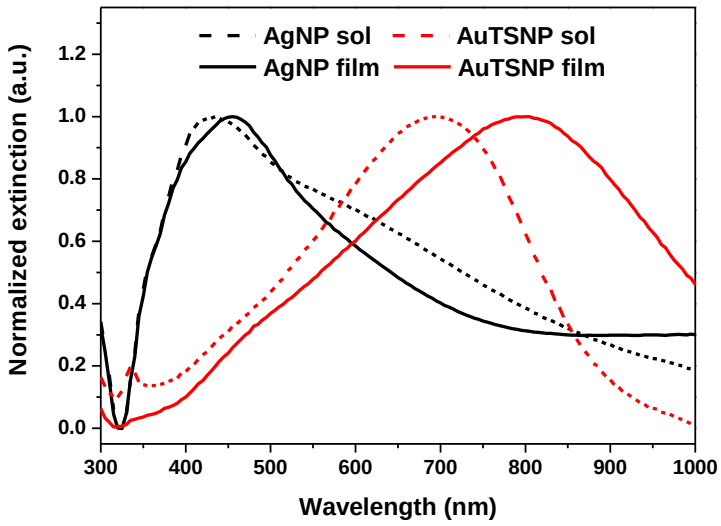

Figure 6.3 Normalized UV-Vis spectra of the AgNP (black) and AuTSNP (red) in suspension (dashed lines) and the corresponding samples immobilized on the substrates (solid lines).

The TEM images of the synthesized AgNP and AuTSNP samples are shown in Figure 6.4. The majority (88 %) of AgNPs featured a roughly faceted spherical structure with an average diameter of 146 ± 21 nm while rod-like structures account for 12 % of the nanoparticle sample (Figure 6.4 A). The AuTSNPs with an average edge length of 30 ± 8 nm showed a high degree of geometric uniformity (Figure 6.4 B). Figure 6.5 A and B show the AFM images of the AgNP and AuTSNP samples deposited on the substrate, respectively. The AuTSNPs were noted to be immobilized onto the substrate via their flat surfaces (Figure 6.5 B). The average height was estimated to be 129 ± 23 nm for the AgNPs and 7 ± 1 nm for the AuTSNPs sample. It was estimated that the surface coverage for AgNPs and AuTSNPs was 43% and 81%, respectively.

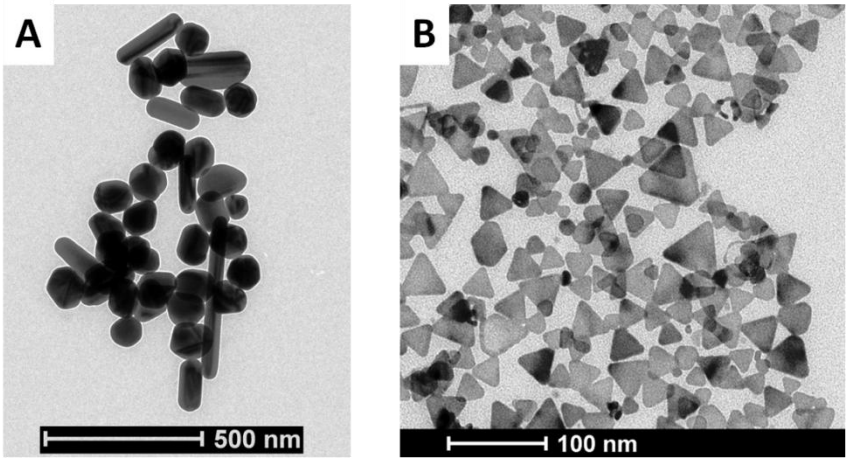

Figure 6.4 TEM images of (A) AgNPs and (B) AuTSNPs.

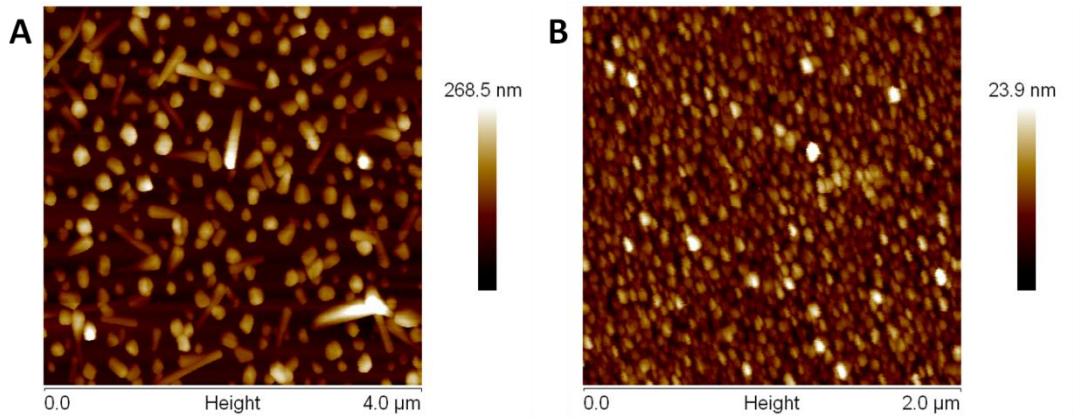

Figure 6.5 AFM images of (A) AgNPs and (B) AuTSNPs deposited on the PEL modified substrate.

6.4.2 Distance dependence of MEF

The prepared nanoparticle films were used to investigate the phenomenon of MEF using Cy5 dye. MEF has been shown to have a distance dependence and this was probed by assembling PAH/PSS bilayers over the nanoparticle films. As illustrated in Figure 6.6, various numbers of bilayers can be deposited on the nanoparticle films to create different distances between the metal and the dye. Each PAH/PSS bilayer has been shown to correspond to an average thickness of 3 nm by ellipsometry.[12] The top graph in Figure 6.7 shows the normalized extinction bands of the AgNP (red) and AuTSNP

(black) films while the bottom graph shows the excitation and emission spectra of Cy5. Clearly, the optical properties of the Cy5 dye are compatible with both nanoparticle systems with their broad plasmon bands.

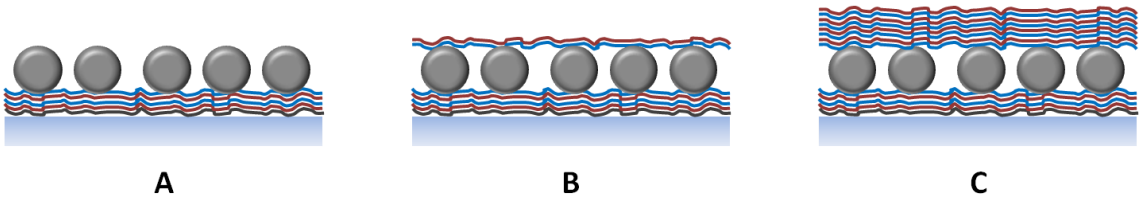

Figure 6.6 Schematic diagram illustrating controlled assembly of PEL layers.

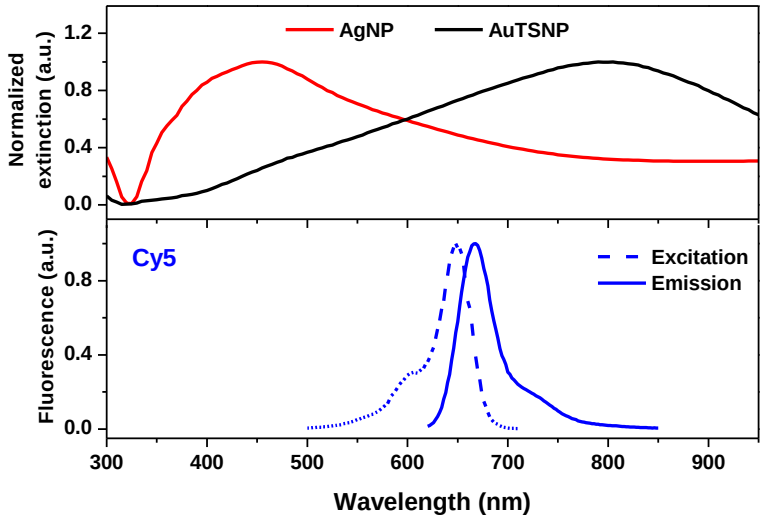

Figure 6.7 Normalized UV-Vis spectra of AgNP (red) and AuTSNP (black) immobilized on the PEL-modified substrate and the excitation (blue dashed line) and emission (blue solid line) of Cy5-PAH conjugate.

The relative enhancement, R_{en}, of fluorescence was calculated using the following equation,

$$R_{en} = \frac{F_{dye-PAH,NP} - F_{NP}}{F_{dye-PAH} - F_{PEL}} \tag{6.1}$$

where $F_{dye-PAH,NP}$ is the fluorescence of the dye-PAH in the vicinity of the nanoparticles, F_{NP} is the background fluorescence of the nanoparticles, $F_{dye-PAH}$ is the

fluorescence of the dye-PAH conjugate alone and F_{PEL} is the background fluorescence of the five PEL layers. A 23-fold relative enhancement of fluorescence for Cy5 in the vicinity of AgNPs was obtained (Figure 6.8 black line) whereas no enhancement was observed for the fluorescence of the dye in the vicinity of AuTSNPs (Figure 6.8 red line). For the Cy5-AgNP system, the lowest enhancement was 10-fold when no PEL layers were placed between the nanoparticles and the dye. The highest enhancement of 23-fold was observed when the thickness of PEL layers was increased to 9 nm. On increasing the thickness of PEL layers to 21 nm, the relative enhancement of the fluorescence slightly dropped to 20-fold. Therefore, the highest enhancement was observed when the distance between the AgNPs and Cy5 molecules was around 9 nm, which is in agreement with previous reports of 3 nm to 50 nm for different systems.[18]

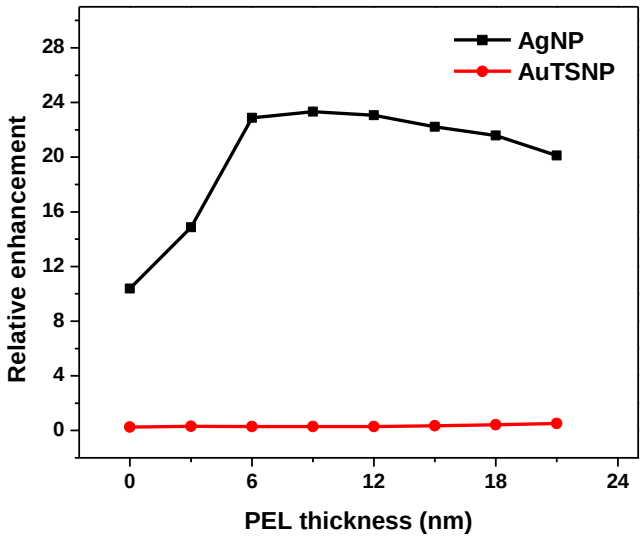

Figure 6.8 Relative enhancement of Cy5 as a function of PEL thickness. Different layers of PEL were placed between the nanostructures and the dye. AgNPs (black) and AuTSNPs (red).

There are a number of reports in the literature of TSNPs showing MEF.[19, 20] The TSNPs showing MEF generally have thicknesses of 12-15 nm whereas the AuTSNPs used in this study are ~ 7 nm thick. It has previously been shown that due to the platelet nature/geometry of similar high aspect ratio TSNPs that their extinction is dominated by absorption processes and that they have a low scattering contribution with a localized electromagnetic field at the particle surface,[16] which is distinct from reports on thicker

TSNPs prepared by a photo-mediated method.[21] The large volume of the AgNPs results in a high scattering contribution to their extinction and thus the observed fluorescence enhancement can be primarily attributed to the scattering component of the nanoparticle extinction. Xu *et al.* have also shown large AgNPs to be better substrates for MEF than TSNPs using a ruthenium dye.[22] They attributed the larger enhancement to the coupling of the AgNP plasmon with the excitation band of the dye without considering the extinction properties of the particles. In our case both our particle systems overlap with the dye spectrum and thus we attribute the difference in enhancement observed to be due to the relative scattering contribution of the nanoparticles.

6.4.3 MEF of the Ru complex using AgNPs

Studies have shown that MEF is influenced by the spectral overlap between fluorophores and the plasmon band of the metal nanoparticles.[19, 22-24] As discussed previously, the optimum enhancement can be achieved when the LSPR band coincides with the excitation/emission wavelength of the fluorophore. Herein, a Ru complex was used to evaluate the effect of spectral overlap on the fluorescence enhancement by large AgNPs. A distance dependence experiment was carried out using PEL multilayers as spacers between the AgNP films and the Ru complex conjugated with PAH. Figure 6.9 A shows the LSPR wavelength of AgNP film and the excitation and emission wavelength of the Ru complex. The excitation wavelength of the Ru complex is ~ 465 nm which overlaps the plasmon resonance of the nanoparticles. As shown in Figure 6.9 B, the optimized thickness of the PEL multilayers is observed to be ~ 9 nm which is in agreement with the value obtained for Cy5. The optimum enhancement of ~ 50-fold is much higher than the value measured for Cy5. This significant improvement of the enhancement factor is probably attributed to the better matched spectra of the Ru-AgNP system compared with the Cy5-AgNP system (Figure 6.7). In addition, the Ru complex exhibits a lower quantum yield (~ 0.067)[25] than Cy5 (~ 0.27).[26] Since greater enhancements have been observed for fluorophores with lower quantum yields,[5] fluorescence enhancement of the Ru complex is expected to be more significant than that of Cy5.

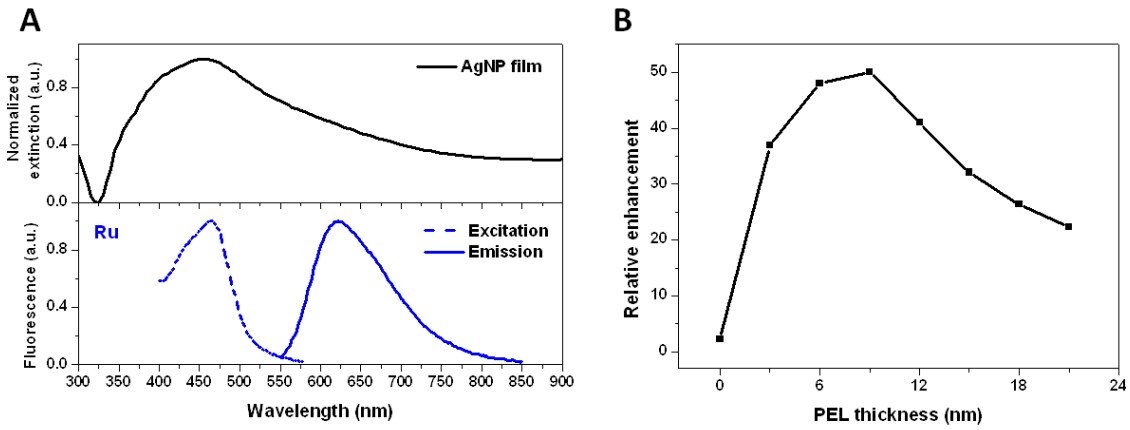

Figure 6.9 (A) Normalized UV-Vis spectra of AgNP (black) immobilized on the PEL-modified substrate and the excitation (blue dashed line) and emission (blue solid line) of Ru-PAH conjugate; (B) Relative enhancement of Ru as a function of PEL thickness.

6.4.4 MEF study using gold coated AgNPs

Silver nanoparticles are prone to oxidation and restructuring with time. [27] In Chapters 4 and 5 we have shown that triangular-shaped nanoparticles undergo an etching process by anions like Cl^-.[28, 29] The use of nanoparticles, in future applications, is reliant on the properties of the nanoparticle being maintained over an extended time period, and thus the long-term stability of the particle is key. To improve the stability of the AgNPs used for the preparation of the enhancement substrates, coating the nanoparticles with a less reactive noble metal, i.e. gold, has been performed. In this work, the gold coating of AgNPs was based on a galvanic replacement reaction previously demonstrated as a means for the efficient saline protection of highly non-isometric TSNP.[30] To investigate the effectiveness of gold coating for improving the stability of the AgNPs, a series of samples was prepared with various quantities of added gold. As shown in Figure 6.10 A, increasing the quantity of gold leads to a redshift, a broadening and a decrease in the UV-vis spectra. The continuous redshift of the AgNP plasmon band, originally at ~ 435 nm, confirms the formation of gold-coated AgNPs. Additionally, this redshift is in agreement with the bimetallic Au/Ag nanoparticles reports on increasing Au molar fraction, where the extinction maximum shifts from the wavelength of pure AgNPs to that of pure AuNPs as the Au fraction increases.[31-33] The distance dependence study of MEF was carried out using the different gold-coated AgNP samples and Cy5. Figure 6.10 B shows the distance dependence of MEF for all samples. As the Au/Ag ratio

increases, the maximum enhancement of Cy5 decreases. In addition, the distance corresponding to the maximum enhancement increases from 9 nm (sample A) to 12 nm (samples B, C and D).

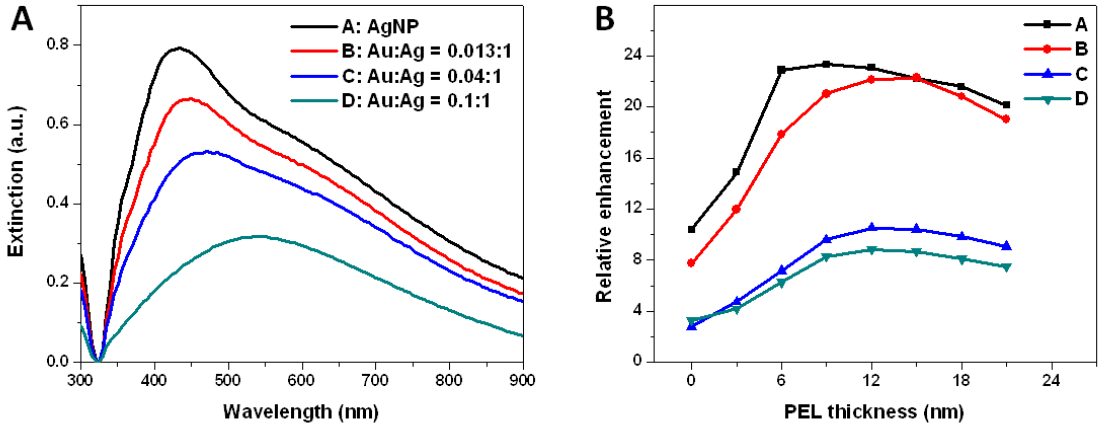

Figure 6.10 (A) UV-vis spectra of AgNPs (black) and three samples of AgNPs coated with increasing quantities of gold. The molar ratio of gold to silver for each sample is shown in the legend. (B) Relative enhancement of Cy5 as a function of PEL thickness using the four samples shown in (A).

The nanoparticles were characterized with TEM for size measurements. The nanoparticle-modified substrates were analyzed with AFM for determination of surface coverage. The TEM and AFM images for all samples are shown in Figure 6.11 and 6.12, respectively. The measurements are summarized in Table 6.1. As more Au is added to the Ag colloid, no significant change in the nanoparticle size is observed. Upon examining the TEM images, the surface of the nanoparticle samples C and D was covered by increasing numbers of small clusters which are assumed to be the gold particles formed during the reaction. According to the AFM images, the surface coverage of the nanoparticles deposited on the substrate is decreased as an increasing amount of gold is added to the Ag colloid. The decrease in surface coverage is considered to be the main factor resulting in the decrease of the fluorescence enhancement as observed in Figure 6.10 B. In order to achieve the appropriate comparison between AgNPs and gold-coated AgNPs, the surface coverage of the gold-coated AgNP samples should be similar to that of the AgNP samples. This can be achieved by increasing the concentrations of the gold-coated AgNP samples. From

these experiments, it is clear that, although the gold-coated AgNPs are likely to have less reactivity and improved long-term stability, they are not as good a choice for the MEF assay system due to the reduced enhancement and surface coverage. Consequently, the assays which follow were carried out using the spherical AgNPs.

Table 6.1 Characterization of samples A-D.

Sample	Mean diameter (nm)	Surface coverage (%)
A (AgNPs)	146 ± 21	43
B (Au:Ag = 0.013:1)	146 ± 25	38
C (Au:Ag = 0.04:1)	145 ± 32	32
D (Au:Ag = 0.1:1)	139 ± 36	21

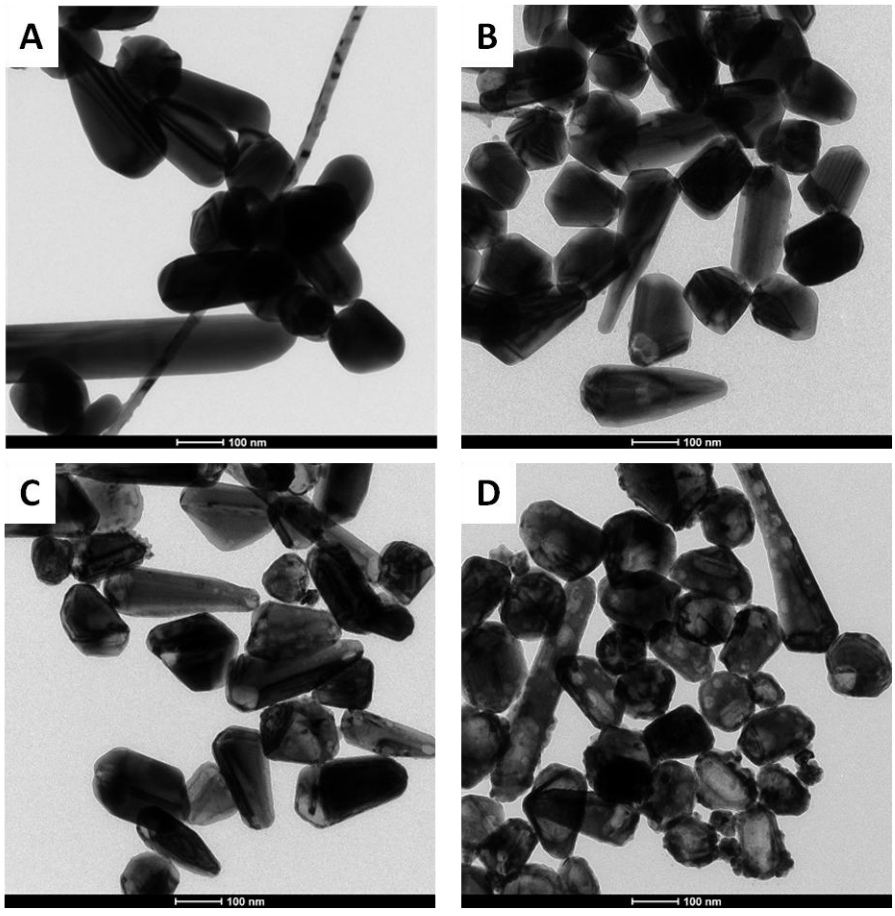

Figure 6.11 TEM images of samples A-D presented in Figure 6.10 A. The scale bar is 100 nm.

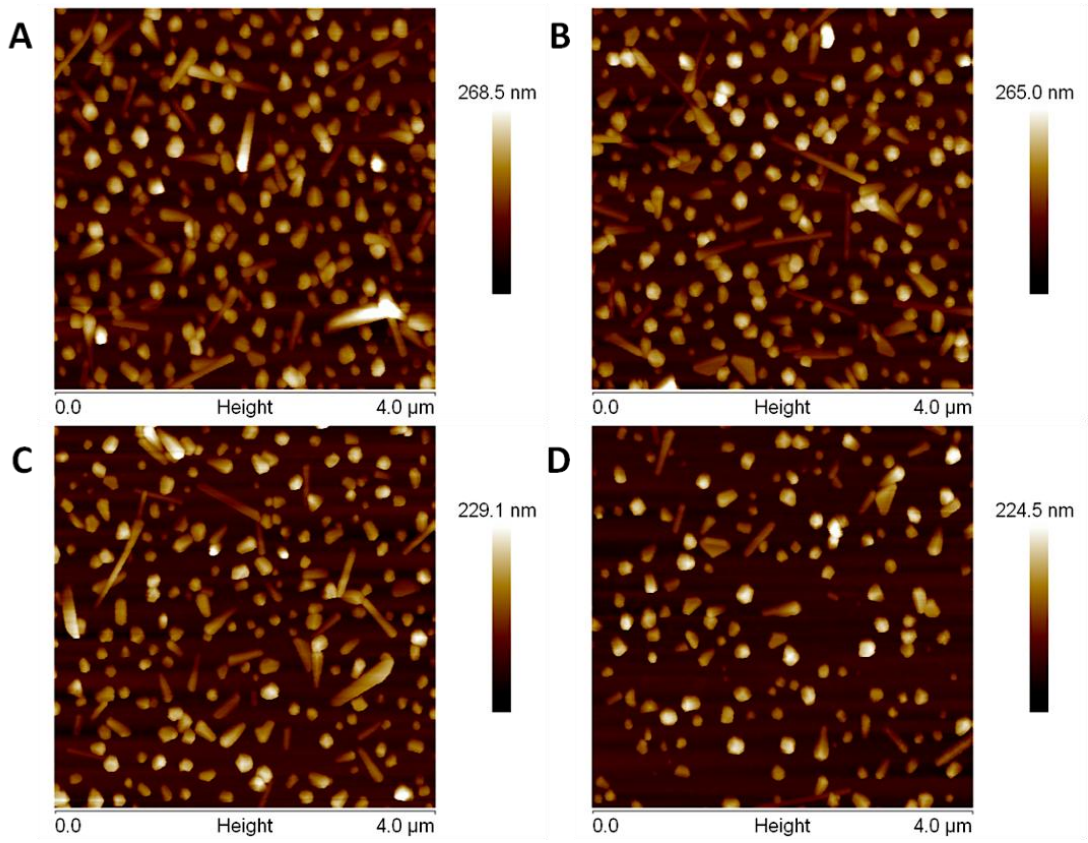

Figure 6.12 AFM images of samples A-D presented in Figure 6.10 A.

6.4.5 IgG assay based on MEF

Previous work has shown that nanoparticle platforms can be used to enhance the performance of immunoassays.[2, 34, 35] Initial work of the MEF assay was performed by adapting a previously reported model assay for the detection of human IgG on the nanoparticle-modified plate.[2] For comparison purposes, a control assay was performed on a conventional Nunc Maxisorp plate without AgNP modification. The detection antibody was labeled with Alexa Fluor 647 which has a similar spectrum to Cy5.

The fluorescence intensity of the assay signal was normalized according to the equation,[36]

$$S/N = \frac{S - B}{\delta_B} \tag{6.2}$$

where S/N is the signal-to-noise ratio, S is the fluorescence intensity of the signal, B is the fluorescence intensity of the background and δ_B is the standard deviation (SD) of

the background intensity. The S/N ratio as a function of human IgG concentration is shown in Figure 6.13.

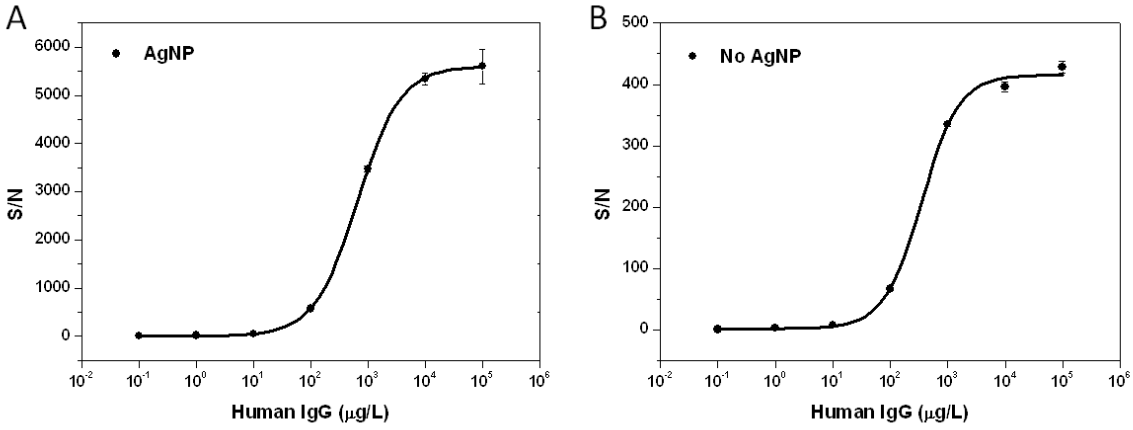

Figure 6.13 (A) Fluorescence immunoassay for the detection of human IgG using AgNPs. (B) A control assay in the absence of AgNPs. (n = 4)

As shown in Figure 6.13, the response for the MEF assay is compared to that for a control assay in the absence of AgNPs. At the highest IgG concentration (10^5 μg/L), the signal was enhanced by ~ 13 times. The background intensity of the enhanced assay (100 ± 9) was approximately four times higher than that of the control assay (23 ± 4), which was due to scattering of the nanoparticles. The LODs of AgNP-enhanced assay and the control assay were estimated to be 0.52 and 4.6 μg/L, respectively. This improvement of ~ 9-fold in LOD is much lower than that reported by Nooney *et al.*[2] who observed ~ 66-fold improvement in LOD. Such discrepancies can be attributed to the different nanoparticles used. One limitation of the method used for fabricating the AgNPs is the lack of batch-to-batch reproducibility. The improvement in LOD for the enhanced assay is mainly due to the MEF phenomenon which amplifies the fluorescence signal of the assay thereby allowing the system to sense lower concentrations of analyte. Upon analyzing the data obtained for both assays, the CV of the background intensity was found to be ~ 9 % for the enhanced assay and ~ 19% for the control assay. The reduction in this CV value for the enhanced assay resulted from the reproducible deposition of AgNPs on the substrate, which also contributes to the improvement of the LOD.

The relative enhancement of fluorescence for the immunoassay derived from the AgNPs in the vicinity of the dye molecules was calculated using the following equation:[2]

$$R_{en} = \frac{F_{assay,NP} - F_{0,NP}}{F_{assay} - F_0} \quad (6.3)$$

where $F_{assay,NP}$ is the fluorescence signal of the AgNP-enhanced assay, $F_{0,NP}$ is the background signal in the presence of AgNPs, F_{assay} is the fluorescence signal of the control assay without AgNPs and F_0 is the background signal of the control assay. The relative enhancement of the immunoassay is plotted against human IgG concentration as demonstrated in Figure 6.14. At the lowest concentration of IgG (0.1 µg/L), the relative enhancement was ~ 10 and this increased to ~ 28 at the highest IgG concentration (10^5 µg/L). A similar trend has been observed previously for a MEF assay.[2] According to the dimensions of IgG reported previously,[37] the estimated distance between the AgNP film and the fluorophore is within 11.4 – 42.6 nm, which is in the distance range that has been reported for MEF.[18] The variation of enhancement with the concentration of analyte will be discussed in the next section as the similar trend has been observed for the CRP assay using the MEF platform.

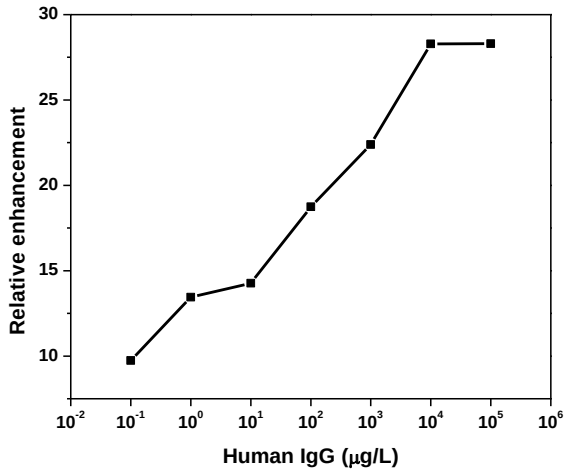

Figure 6.14 The change in relative enhancement of an AgNP-enhanced immunoassay with change in human IgG concentration.

6.4.6 CRP assay based on MEF

Since enhancement was observed for the model assay described in the previous section, the MEF assay format was extended to the application of human CRP detection. In this sandwich assay system, the detection antibody molecules were labeled with DY-647, which has a similar spectrum and properties to Cy5 and Alexa Fluor 647 as shown in Figure 6.15. A control assay was performed on a conventional Nunc Maxisorp plate without AgNP modification.

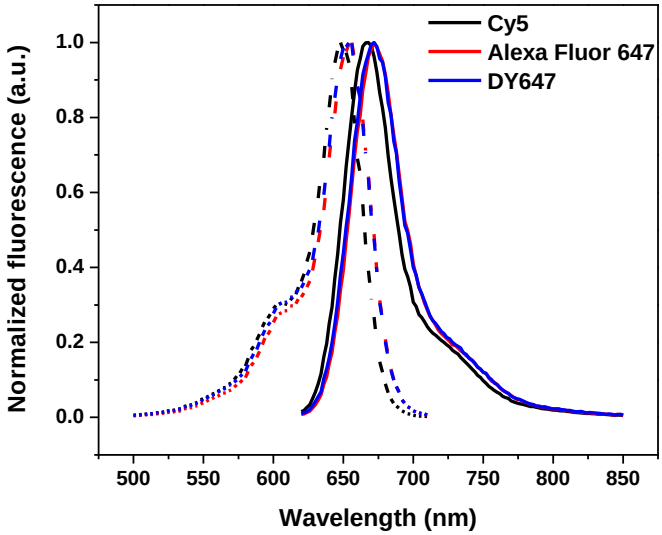

Figure 6.15 Excitation (dashed lines) and emission (solid lines) spectra of Cy5 (black), Alexa Fluor 647 (red) and DY647 (blue).

The fluorescence response as a function of human CRP concentration is shown in Figure 6.16. Compared to the control assay, a significant increase in the fluorescence signal was observed for the AgNP-enhanced assay. At the highest CRP level (10 mg/L), the signal was enhanced by 60 fold. The background intensity of the enhanced assay (76 ± 1.7) was roughly five times higher than that of the control assay (15 ± 4.6). This increase in the background intensity was also observed for the IgG assay, which is attributed to the scattering of nanoparticles. The LODs for the AgNP-enhanced assay and the control assay were 0.24 µg/L and 4.5 µg/L, respectively. This LOD compares well with that reported by Luo *et al.*[38] who obtained an LOD of 0.06 µg/L for their fluorescence-based CRP assay using quantum dot labels.[38] Luo *et al.* found that they

had to adopt a two-step detection to overcome the instability of their quantum dot-labeled antibody, whereas the MEF-based assay requires a single detection step. It was found that the CV of the background intensity was 2.3% for the enhanced assay and 29 % for the control assay. The reduction in this CV value was similar to the trend observed for the IgG assay, suggesting that the AgNP-modified substrate provides a more homogeneous platform for the assay performance, which is a key factor in the production of reproducible assays. When comparing with the homogenous CRP assays performed using AuTSNP sol as described in Chapter 5, the MEF assay shows a significantly lower LOD than the solution-phase assays which have LODs ranged from 1.29 to 1.62 mg/L.

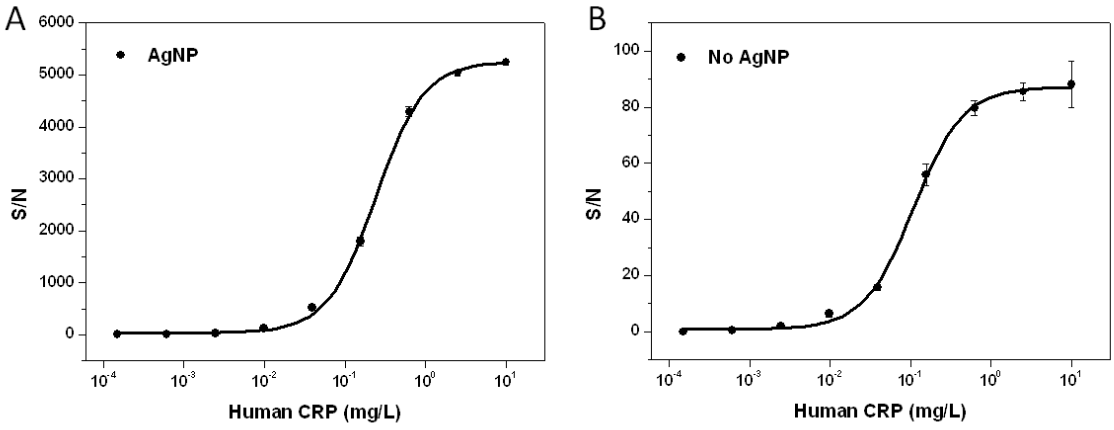

Figure 6.16 (A) Fluorescence immunoassay for the detection of human CRP using AgNPs. (B) A control assay in the absence of AgNPs. The insets show the corresponding assays for the detection of human CRP at low concentration. (n = 4)

The relative enhancement of the immunoassay is plotted against human CRP concentration as demonstrated in Figure 6.17 A. The relative enhancement was 2-fold at the lowest analyte level (1.5×10^{-4} mg/L) and increased to 22-fold at the highest CRP level (10 mg/L), showing a similar trend to the one observed for the IgG assay. For comparison purpose, a distance dependence experiment was carried out using DY647-PAH and the same batch of nanoparticles. As shown in Figure 6.17 B, the optimum enhancement (~ 31-fold) was observed when the distance between the dye and AgNPs was 6 nm, differing from the results obtained for the Cy5-AgNP system. The discrepancy between these two systems can be explained by the variation of

nanoparticles from batch to batch and the different dyes used for the study. Estimating the dimensions of an antibody molecule as 14.2 × 8.5 × 3.8 nm and a pentameric CRP molecule as 10.2 × 3.6 nm,[37, 39] the average distance between the fluorophores and the AgNP surface in this assay is within 10.8 - 38.6 nm. The increase in relative enhancement with increasing concentrations of CRP is likely to be due to a change in the protein orientation with higher loading. Since no attempt has been made in this assay platform to align the protein vertically, comparing the relative enhancement of 31 obtained for a separation distance of 6 nm using the PEL spacer layers (Figure 6.17 B) and 22 for the highest concentration of CRP (Figure 6.16) it can be suggested that the antibody is lying flat on the silver surface. Furthermore, the preferred orientation mode for an antibody spontaneously adsorbed to negatively charged surface has been reported to be flat-on by another group.[37, 40]

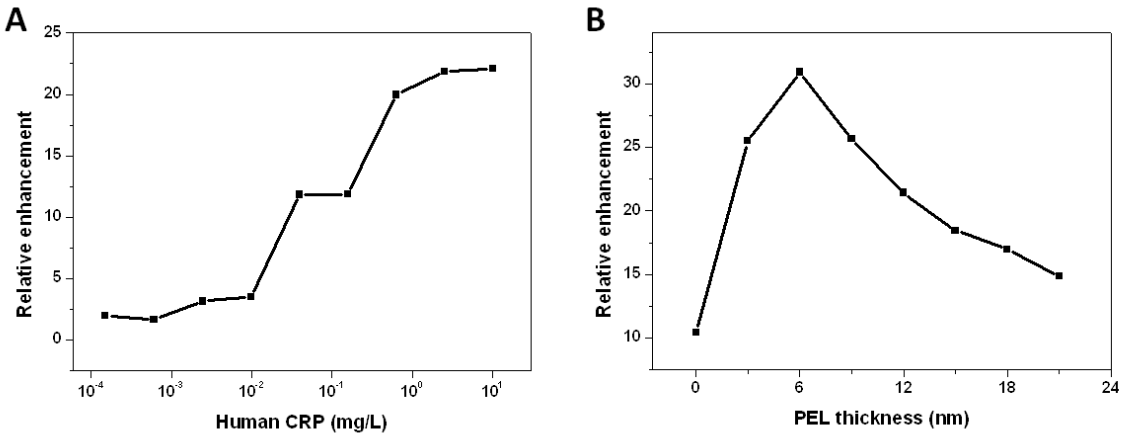

Figure 6.17 (A) The change in relative enhancement of the MEF immunoassay with change in human CRP concentration; (B) Relative enhancement of DY647 as a function of PEL thickness.

Initially, two hypotheses were proposed to explain the enhancement of the fluorescence immunoassay: (i) the coupling of the fluorophore excitation/emission with the plasmonic scattering components of the AgNPs and (ii) an increased surface area for the AgNP-modified plate that could bind more capture antibodies than the control plate, resulting in a higher fluorescence signal. To examine the second hypothesis, a KCN test was carried out on the AgNP-enhanced assay system. The addition of KCN (0.1 M) to the AgNP-modified wells induced the dissolution of the nanoparticles, releasing the

antibody-antigen complexes into the solution. Schneider and Decher previously showed that dissolving the Au cores of fluorescent core-shell nanoparticles by KCN made significant changes in the fluorescence.[41] Figure 6.18 shows the extinction spectra of the AgNP film before and after addition of KCN.

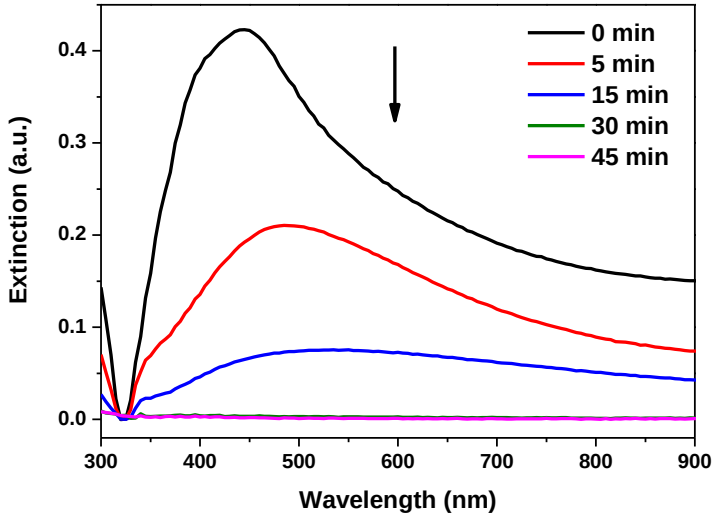

Figure 6.18 UV-Vis spectra of the AgNP film before (black) and after addition of 0.1 M KCN.

After addition of KCN, the extinction spectrum of the AgNP film was monitored. The LSPR band disappeared within 45 min confirming dissolution of the AgNPs. The fluorescence signal of the CRP assay was collected and the data was then compared with the enhanced assay and the control assay as shown in Figure 6.19. Upon dissolving the nanoparticles, the fluorescence signal of the assay with AgNPs dropped to a comparable level to that observed for the control assay. This indicates that the enhanced fluorescence signal is not as a result of the increased surface area but is directly as a result of the MEF effect.

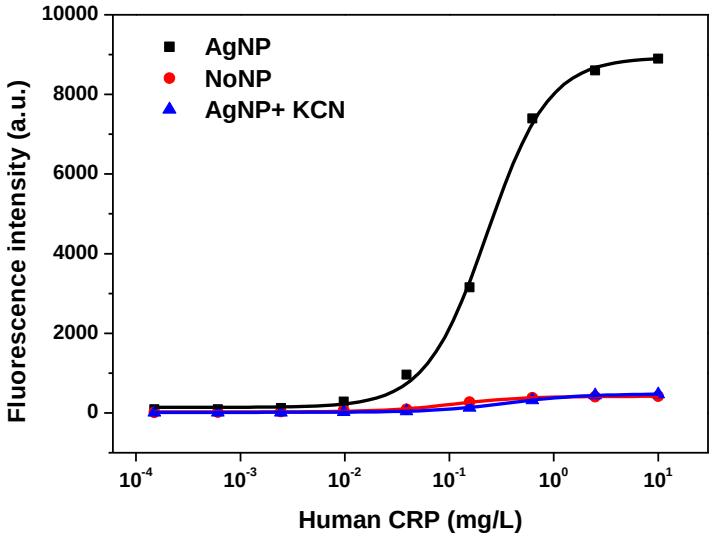

Figure 6.19 Fluorescence signal of the immunoassay enhanced with AgNPs before (black) and after (blue) dissolving the nanostructures in 0.1 M KCN. The data is compared with the control assay without AgNPs (red).

6.5 Conclusions

In this work, the effects of large AgNP and AuTSNP films on the enhancement of fluorescence were investigated. The AgNP film was observed to enhance the fluorescence of Cy5 by 23-fold whereas no enhancement was found for the AuTSNPs. This enhancement is attributed to the large scattering component of the AgNP sample. It is believed that this work further supports the emerging radiating plasmon model for MEF.[6] The radiating plasmon model suggests that the excited fluorophore interacts with the nearby metal nanoparticle, generating far-field radiation at the emission wavelength. According to this model, the relative scattering contribution of the nanoparticle extinction determines the MEF. A nanoparticle with its extinction dominated by scattering is believed to enhance fluorescence.

A Ru complex was used to examine the effect of spectral overlap on the fluorescence enhancement. Comparing to the Cy5-AgNP system, higher enhancement was observed for the Ru-AgNP system. This can be due to the better matched spectra between the Ru

complex and the nanoparticles as well as the lower quantum yield of the dye which is a better candidate for the radiative decay engineering processe as discussed by Lacowicz.[5]

To improve the long-term stability of the AgNP platform, gold coating of the particles was performed. The effects of gold-coated AgNP samples on the fluorescence enhancement were investigated. Decreasing enhancements were observed for the samples with increasing Au/Ag ratios, which was mainly attributed to surface coverage. To obtain the appropriate comparison between the nanoparticle samples, the surface coverage of gold-coated AgNPs should be similar to that of AgNPs by increasing the concentrations of the coated particles. This will be part of the future work.

The large AgNPs were initially used in a model assay for the detection of human IgG and a significant increase in the fluorescence signal was observed. The LOD of the assay was improved by ~ 9-fold when compared with the assay in the absence of nanoparticles. The relative enhancement was found to increase with the analyte concentration. The same MEF assay format was further used to enhance a CRP sandwich immunoassay and the LOD of the assay was improved by 19-fold. Similar to the enhanced IgG assay, the relative enhancement was observed to increase with the CRP concentration. The increases in fluorescence signals and improvements in the LODs for both immunoassays are primarily due to the interactions of the fluorophores with the plasmonic scattering components of the AgNPs. Notably the MEF-based CRP assay compares well with the best reports to date,[38] requiring only a single detection step. In addition, the LOD of the MEF-based CRP assay is much lower than those of the commercial assays as listed in Table 4.1. Though clinically relevant range for CRP assay is high, the MEF-based platform can be used for other cases requiring high sensitivities such as cTnI assay. Additionally, low-cost optics can be used for the read-out of MEF-based assays due to their significantly enhanced signal, which has the advantage of developing diagnostic systems for low resource environments. This work demonstrates the potential of MEF for enhancing the performance of immunoassays, with the AgNP substrates providing a reproducible and sensitive detection platform. In the next chapter, an evaluation is carried out on the results obtained for all the different assay formats performed in this thesis work.

References

1. E. G. Matveeva, Z. Gryczynski and J. R. Lakowicz, Journal of Immunological Methods **302** (1–2), 26-35 (2005).
2. R. Nooney, A. Clifford, X. LeGuevel, O. Stranik, C. McDonagh and B. MacCraith, Anal Bioanal Chem **396** (3), 1127-1134 (2010).
3. A. Barnett, E. G. Matveeva, I. Gryczynski, Z. Gryczynski and E. M. Goldys, Physica B: Condensed Matter **394** (2), 297-300 (2007).
4. H. Szmacinski, Z. Murtaza and J. R. Lakowicz, The Journal of Physical Chemistry C **114** (16), 7236-7241 (2010).
5. J. R. Lakowicz, Analytical Biochemistry **298** (1), 1-24 (2001).
6. J. R. Lakowicz, Analytical Biochemistry **337** (2), 171-194 (2005).
7. Y. Zhang, K. Aslan, M. J. R. Previte and C. D. Geddes, Applied Physics Letters **90** (5), 053107/053101-053107/053103 (2007).
8. R. Bardhan, N. K. Grady, J. R. Cole, A. Joshi and N. J. Halas, ACS Nano **3** (3), 744-752 (2009).
9. K. Aslan, Z. Leonenko, J. Lakowicz and C. Geddes, J Fluoresc **15** (5), 643-654 (2005).
10. Y. Zhang, A. Dragan and C. D. Geddes, The Journal of Physical Chemistry C **113** (28), 12095-12100 (2009).
11. P. P. Pompa, MartiradonnaL, A. D. Torre, F. D. Sala, MannaL, M. De Vittorio, CalabiF, CingolaniR and RinaldiR, Nat Nano **1** (2), 126-130 (2006).
12. R. I. Nooney, O. Stranik, C. McDonagh and B. D. MacCraith, Langmuir **24** (19), 11261-11267 (2008).
13. Y. Tan, Y. Li and D. Zhu, Journal of Colloid and Interface Science **258** (2), 244-251 (2003).
14. P. K. Jain and M. A. El-Sayed, Chemical Physics Letters **487** (4-6), 153-164 (2010).
15. D. E. Charles, D. Aherne, M. Gara, D. M. Ledwith, Y. K. Gun'ko, J. M. Kelly, W. J. Blau and M. E. Brennan-Fournet, ACS Nano **4** (1), 55-64 (2010).
16. D. Charles, M. Gara, D. Aherne, D. Ledwith, J. Kelly, W. Blau and M. Brennan-Fournet, Plasmonics, 1-12 (2011).
17. T. R. Jensen, M. L. Duval, K. L. Kelly, A. A. Lazarides, G. C. Schatz and R. P. Van Duyne, The Journal of Physical Chemistry B **103** (45), 9846-9853 (1999).

18. H. Szmacinski, D. S. Smith, M. A. Hanson, Y. Kostov, J. R. Lakowicz and G. Rao, Biotechnology and Bioengineering **100** (3), 448-457 (2008).
19. Y. Chen, K. Munechika and D. S. Ginger, Nano Letters **7** (3), 690-696 (2007).
20. K. Aslan, J. R. Lakowicz and C. D. Geddes, The Journal of Physical Chemistry B **109** (13), 6247-6251 (2005).
21. K. Munechika, J. M. Smith, Y. Chen and D. S. Ginger, The Journal of Physical Chemistry C **111** (51), 18906-18911 (2007).
22. S. Xu, Y. Cao, J. Zhou, X. Wang, X. Wang and W. Xu, Nanotechnology **22** (27), 275715 (2011).
23. M. Thomas, J. J. Greffet, R. Carminati and J. R. Arias-Gonzalez, Applied Physics Letters **85** (17), 3863-3865 (2004).
24. F. Tam, G. P. Goodrich, B. R. Johnson and N. J. Halas, Nano Letters **7** (2), 496-501 (2007).
25. U. Neugebauer, Y. Pellegrin, M. Devocelle, R. J. Forster, W. Signac, N. Moran and T. E. Keyes, Chemical Communications **0** (42), 5307-5309 (2008).
26. M. Sauer, J. Hofkens and J. Enderlein, *Handbook of Fluorescence Spectroscopy and Imaging: From Ensemble to Single Molecules*. (Wiley, 2010).
27. H.-I. Peng, T. D. Krauss and B. L. Miller, Analytical Chemistry **82** (20), 8664-8670 (2010).
28. J. An, B. Tang, X. Zheng, J. Zhou, F. Dong, S. Xu, Y. Wang, B. Zhao and W. Xu, The Journal of Physical Chemistry C **112** (39), 15176-15182 (2008).
29. X. C. Jiang and A. B. Yu, Langmuir **24** (8), 4300-4309 (2008).
30. D. Aherne, D. E. Charles, M. E. Brennan-Fournet, J. M. Kelly and Y. K. Gun'ko, Langmuir **25** (17), 10165-10173 (2009).
31. S. Link, Z. L. Wang and M. A. El-Sayed, The Journal of Physical Chemistry B **103** (18), 3529-3533 (1999).
32. M. Moskovits, I. Srnova-Sloufova and B. Vlckova, The Journal of Chemical Physics **116** (23), 10435-10446 (2002).
33. S. E. Hunyadi and C. J. Murphy, Journal of Materials Chemistry **16** (40), 3929-3935 (2006).
34. X. Wei, H. Li, Z. Li, M. Vuki, Y. Fan, W. Zhong and D. Xu, Anal Bioanal Chem **402** (3), 1057-1063 (2012).

35. N. Lochner, C. Lobmaier, M. Wirth, A. Leitner, F. Pittner and F. Gabor, European Journal of Pharmaceutics and Biopharmaceutics **56** (3), 469-477 (2003).
36. Y. Chen, V. Kamat, E. R. Dougherty, M. L. Bittner, P. S. Meltzer and J. M. Trent, Bioinformatics **18** (9), 1207-1215 (2002).
37. H. Xu, X. Zhao, J. R. Lu and D. E. Williams, Biomacromolecules **8** (8), 2422-2428 (2007).
38. Y. Luo, B. Zhang, M. Chen, T. Jiang, D. Zhou, J. Huang and W. Fu, Journal of Translational Medicine **10** (1), 24 (2012).
39. A. Agrawal, A. K. Shrive, T. J. Greenhough and J. E. Volanakis, The Journal of Immunology **166** (6), 3998-4004 (2001).
40. H. Xu, X. Zhao, C. Grant, J. R. Lu, D. E. Williams and J. Penfold, Langmuir **22** (14), 6313-6320 (2006).
41. G. Schneider, G. Decher, N. Nerambourg, R. Praho, M. H. V. Werts and M. Blanchard-Desce, Nano Letters **6** (3), 530-536 (2006).

Chapter 7

Conclusions and future work

7.1 Conclusions

The aim of the work was to experimentally investigate the biosensing applications of noble metal nanoparticles in terms of various assays.

Initial work was carried out at NUIG during the first year of my PhD program, which involved homogeneous, refractive index sensitivity-based assays for detecting human CRP and cTnI using triangular nanoplates including TSNPs and AuTSNPs. The synthetic methods of these nanoplates were developed in Prof. John Kelly's group in the chemistry department in TCD. The nanoplates were conjugated with PC molecules and aTnI antibody to form biosensors for the corresponding CRP and cTnI detection. The refractive index sensitivities of the bare nanoplates and biosensors before and after centrifugation were examined using a sucrose method. All samples showed sensitivities near or above the optimum values predicted by the theory of Miller *et al.* regardless of centrifugation, suggesting that the PC and aTnI-conjugated nanoplates can serve as efficient sensors for the corresponding CRP and cTnI detection. Additionally, gold coating of the TSNPs was considered to protect the morphology of the nanoplates and thus maintain their sensitivities. In the case of the CRP assays, PC-AuTSNPs showed a higher sensitivity and greater LSPR response than PC-TSNPs. The lowest concentrations of analyte that were detected by PC-TSNPs and PC-AuTSNPs were 0.017 mg/L and 3.3×10^{-3} mg/L of CRP, respectively. When the analyte increased to 3.34 mg/L, both sensors approached saturation. In the case of cTnI assays, both aTnI-TSNPs and aTnI-AuTSNPs started to show a redshift in their LSPR peaks when cTnI was 4.1 µg/L. Similar to the case of the CRP assays, aTnI-AuTSNPs generally presented a greater LSPR response than aTnI-TSNPs. At the highest concentration of cTnI (333 µg/L), no saturation was observed for both sensors. Unfortunately, the work was discontinued due to IP restrictions on the use of the Kelly particles in DCU, and it was infeasible to implement a set of replicates to estimate an LOD and a working range

for each assay. Furthermore, optimization of the sensors and the assays was impossible for the same reason. Nevertheless, the AuTSNPs showed promise as robust and highly sensitive sensors for biosensing applications.

Following the work conducted in the first year, the homogeneous CRP assays were carried on with alternative nanoplates that were synthesized using a different method. In this case the AuTSNPs were conjugated with aCRP monoclonal antibodies C2 and C6. The refractive index sensitivities of the bare nanoplates and biosensors were estimated using the sucrose method. Unlike the Kelly particles, the alternative nanoplates presented sensitivities below the Miller line, indicating that these particles may not be as sensitive as the Kelly particles. C2-AuTSNPs, C6-AuTSNPs and a 1:1 mixture of these two sensors were individually used for the CRP assays, the corresponding LODs for which were 1.53, 1.62 and 1.29 mg/L. However, instability of the sensors was observed after they were prepared for a few days. It was decided to evaluate the potential performance achievable with a commonly developed aggregation-based assay approach using spherical AuNPs. In this case, the AuNPs were conjugated with polyclonal aIgG, forming biosensors for human IgG detection. Upon adding the analyte, the AuNPs aggregated and an increase in the extinction intensity at 600 nm was observed. The LOD for this assay was determined to be 1.59 mg/L, which was lower than a similar assay reported previously.[1]

To explore the potential application of the alternative AuTSNPs for biosensing approaches, the nanoplates were incorporated into an SPR system for detection of human IgG. In this biosensing system AuTSNPs acted as an enhancer to amplify the SPR response to the antigen-antibody binding event, thus improving the sensitivity of the SPR detection. Compared to a control assay, the assay using AuTSNP-conjugated aIgG presented a significantly increased binding response. However, non-specific binding was observed for the assays which can be minimized by optimizing the blocking step. Currently, the mechanism behind nanoparticle-enhanced SPR is not fully understood. Possible mechanisms include (i) increased surface mass, (ii) increased refractive index of the analyte and (iii) the plasmon resonant coupling between the nanoparticles and the gold film.[2] Though more work needs to be carried out to further investigate the assay, this preliminary experiment has shown great potential for enhanced sensitivity of SPR detection incorporating AuTSNPs.

The last section of the work involved the MEF-based assays using noble metal nanoparticles. Initially, the effect of AuTSNPs on the enhancement of fluorescence was evaluated and compared with that of large spherical AgNPs. A distance dependence of the fluorescence enhancement was observed for AgNPs whereas no enhancement was observed for AuTSNPs. This is attributed to the large scattering component of the AgNP extinction. Since large AgNPs showed an enhancement effect on the fluorescence, the following experiments were performed using these particles. The effect of spectral overlap on the MEF was examined using a Ru dye which was compared with Cy5. Due to the better matched spectra between the Ru dye and nanoparticles, a much higher enhancement was obtained for Ru-AgNP system. Additionally, gold coating of the nanoparticles was performed to improve the long term stability of the AgNPs. The enhancement effects of the gold-coated AgNPs on the fluorescence were estimated. Decreasing enhancements were noted for the particles with increasing Au/Ag ratios, which was mainly due to the decreases in the surface coverage. The AgNP-coated substrates were used for enhanced assays for the detection of human IgG and CRP. A remarkable increase in the fluorescence signal was observed for the enhanced assays. The LODs of the IgG and CRP assays were improved by ~ 9-fold and 19-fold, respectively. These effects were primarily attributed to the coupling of the fluorescence to the scattering component of the nanoparticle LSPR extinction. This work signifies that MEF provides a promising approach for improving the assay performance.

A comparison of all the assays carried out in this thesis is shown in Table 7.1. With respect to the assays for the detection of CRP, the lowest LOD (0.24 µg/L) is observed for the MEF-based assay, which is much lower than the values for the commercial hs-CRP assays as listed in Table 4.1. However, as a conventional heterogeneous sandwich assay, washing steps are required and the assay time is very long. Though the refractive index sensitivity-based assay is a more straightforward method, its LOD is much higher than the values of the commercial assays. The solution-phase refractive index sensitivity-based and aggregation-based assays are usually used for colorimetric detection. In general, they are better choices for point-of-care devices and for low resource environments due to their simplicity and low cost. The MEF platform provides an efficient approach for the enhancement of fluorescence-based assay to detect analytes that require a low LOD, such as cTnI. SPR biosensing offers rapid detection

and the study of various biomolecules such as proteins and nucleic acids in real time. Incorporation of nanoparticles into this sensing system can increase measurement sensitivities, particularly with respect to small molecule detection.

Table 7.1 Comparison of the assays performed in this thesis

	Refractive index sensitivity-base assay (Kelly particles)	**Refractive index sensitivity-base assay (alternative AuTSNPs)**	**Aggregation-based assay (AuNPs)**	**AuTSNP-enhanced SPR assay**	**MEF-based assay (AgNPs)**
Assay time	30 min	90 min	90 min	10 min	120 min
Analyte volume	10 µL	10 µL	10 µL	100 µL	100 µL
LOD	N/A	1.29 mg/L of CRP	1.59 mg/L of IgG	N/A	0.52 µg/L of IgG, 0.24 µg/L of CRP
Measurement	LSPR λ_{max}	LSPR λ_{max}	LSPR λ_{600nm}	SPR response	Fluorescence
Instrumentation	UV-vis spectrometer	UV-vis spectrometer	UV-vis spectrometer	Biacore 3000	Fluorescence spectrometer
Washing steps	No	No	No	Yes	Yes
Cost	Low	Low	Low	High	High

7.2 Future work

The next stage of the work will involve a further investigation of the nanoparticle-enhanced SPR detection using nanoparticles of various shapes and sizes. In addition to the AuTSNPs, other nanoparticles such as nanospheres and nanorods can be incorporated into the SPR sensing system. Particularly, an LOD of 1 aM was reported for an SPR detection enhanced by nanorods.[3] Furthermore, the effect of the nanoparticle size on the enhanced SPR detection needs to be evaluated.

With respect to the MEF-based assay, further investigation of MEF using gold-coated AgNPs is needed. To improve the reproducibility of the AgNP-coated substrates, a

method for preparing more homogeneous nanoparticles is required. Additionally, shaped nanoparticles such as nanorods could be used for the evaluation of the MEF.[4, 5]

For the development of assays, a few parameters are required for optimization including the concentration of antibody or antibody-nanoparticle conjugates, pH and ionic strength of the assay buffer, incubation temperature and duration. Sufficient blocking is also needed to prevent non-specific binding. To verify the specificity of the antibody-antigen reaction, negative controls need to be included when carrying out the assays. Multiple replicates need to be carried out within the same day and on different days to estimate the precision of the assay. Statistically, LOD, limit of quantitation (LOQ) and the working range of the assay can be estimated according to a set of assay with multiple replicates.

Currently, the field of biosensing with noble metal nanoparticles is a fast growing area in biomedical sciences. The unique optical properties of the nanoparticles provide numerous exciting prospects for highly sensitive detection of biomolecules. While a lot of achievements have been obtained in this field, more significant progress will be made in the next few years.

References

1. Q. Cao, H. Yuan and R. Cai, J. Wuhan Univ. Technol.-Mat. Sci. Edit. **24** (5), 772-775 (2008).
2. L. He, M. D. Musick, S. R. Nicewarner, F. G. Salinas, S. J. Benkovic, M. J. Natan and C. D. Keating, Journal of the American Chemical Society **122** (38), 9071-9077 (2000).
3. H. R. Sim, A. W. Wark and H. J. Lee, Analyst **135** (10), 2528-2532 (2010).
4. K. Aslan, Z. Leonenko, J. R. Lakowicz and C. D. Geddes, The Journal of Physical Chemistry B **109** (8), 3157-3162 (2005).
5. A. M. Gabudean, M. Focsan and S. Astilean, The Journal of Physical Chemistry C **116** (22), 12240-12249 (2012).

List of publications and presentations

Peer-reviewed publications:

Zhang Y., Keegan G., McDonagh C. and Brennan-Fournet M. (2013). Highly sensitive C-reactive protein (CRP) assay using metal-enhanced fluorescence (MEF). Manuscript submitted.

Oral presentations:

Zhang Y., Voisin M., Ledwith D. and Brennan-Fournet M. (2010). One-step highly sensitive human cardiac troponin I diagnostic method using plasmonic silver nanoplate sensors. Oral presentation delivered at Inspire Bionano Postgraduate research workshop, UCD, Ireland

Poster presentations:

1. Zhang Y., Voisin M., Ledwith D. and Brennan-Fournet M. (2010). Solution phase triangular silver nanoplates for highly sensitive surface plasmon resonance sensing of C-reactive protein. Poster presentation delivered at Inspire Bionano Postgraduate research workshop, UCD, Ireland

2. Zhang Y., Keegan G, McDonagh C and Brennan-Fournet M (2012) Nobel metal nanoparticles for immunoassays. Poster presentation delivered at BOC Gases poster competition, DCU, Ireland

3. Zhang Y., Keegan G., Brennan-Fournet M. and McDonagh C. (2013). Highly sensitive C-reactive protein assay using metal-enhanced fluorescence. Poster presentation delivered at the 4th International Congress Nanotechnology in Medicine and Biology, BioNanoMed 2013, Krems, Austria

Appendix A

Estimation of nanoparticle concentration

1. Triangular nanoplates

The concentration of nanoplates in a typical sol was estimated, by presuming that all of the $AgNO_3$ used in the preparation, was converted to nanoplates of exactly the same size, with an edge length of 30 nm and a thickness of 7 nm. The diameter of a silver atom was taken as 0.288 nm and the edge length of a unit cell as 0.4086 nm. A unit cell consists of 4 silver atoms. According to the following equation,

$$No.of\ particles = \frac{Total\ No.of\ Ag\ atoms\ in\ sol}{No.of\ Ag\ atoms\ in\ a\ particle} \quad (A.1)$$

It was estimated that a typical sol had a concentration of ~ 6×10^{12} particles/L for the Kelly particles and ~ 3×10^{14} particles/L for the alternative nanoplates prepared using the method of Zhang *et al.*.

2. Spherical AuNPs

For the AuNPs used in the IgG assay, the concentration c was estimated according to Beer-Lambert law,

$$c = \frac{A}{\epsilon l} \quad (A.2)$$

where A is the absorbance, ϵ is the molar extinction coefficient, c is the concentration of the absorbing sample and l is the path length through the sample. ϵ was taken as 2.4×10^8 $m^{-1}cm^{-1}$ and l was taken as 1 cm. It was calculated that a typical assay solution contained 4.3×10^{12} particles/mL.

Appendix B

Estimation of antibody concentration in aIgG-AuTSNP sol

It was presumed that there was a monolayer of antibody adsorbed on the surface of the nanoplates. An antibody has an adsorption density of ~ 2.5 mg/m^2 on a particle surface.[1] The concentration of the nanoplates was taken as 3×10^{14} particles/L and the molecular weight of antibody was taken as 150kDa. The edge length and the thickness of the nanoplates were taken as 30 nm and 7 nm, respectively. Therefore, it was estimated that the aIgG-AuTSNP sol contained ~ 1 µg/mL of aIgG.

Reference

1. G. T. Hermanson, *Bioconjugate Techniques*. (Academic Press, 2008).